Aerodynamic Design and Optimization of a Hyperloop Vehicle

F.T.H. Wong

Technische Universiteit Delft

TUDelft

Delft
University of
Technology

Challenge the future

Aerodynamic Design and Optimization of a Hyperloop Vehicle

by

F.T.H. Wong

in partial fulfillment of the requirements for the degree of

Master of Science
in Aerospace Engineering

at the Delft University of Technology,
to be defended publicly on Wednesday May 23, 2018 at 02:00 PM.

Supervisor:	Dr. ir. A. H. van Zuijlen	TU Delft
	M. van der Meijs	HARDT
Thesis committee:	Prof. dr. ir. L. L. M. Veldhuis	TU Delft
	Dr. ir. M. Voskuijl	TU Delft

An electronic version of this thesis is available at http://repository.tudelft.nl/.

TUDelft
Delft
University of
Technology

Preface

My academic career at the faculty of Aerospace Engineering at the Delft University of Technology has further nurtured my passion for the design and analysis of aerospace vehicles. I feel blessed that I have had the opportunity to enjoy an utmost challenging and engaging study program.

I am grateful that I can finish my Master program with a research on an interesting and present-day engineering topic: the aerodynamic design and optimization of a Hyperloop vehicle.

I would first of all like to express my gratitude towards my academic supervisor Alexander van Zuijlen for his willingness to supervise and guide me during this research project. His valuable feedback, keen observations and invested time have all enabled me to acquire the desired outcomes and results for this project.

I would furthermore like to thank my supervisor from HARDT Hyperloop, Marinus van der Meijs, whom has given me great insights and knowledge on the research topic. His feedback and support have been very valuable to me and I could not have obtained the final results without these. The dedication for his work is truly inspiring. Together with Marinus, I would like to thank Tim Houter, Mars Geuze and Sascha Lamme for giving me the opportunity to perform my thesis work at HARDT Hyperloop.

I also wish to thank professors Leo Veldhuis and Mark Voskuijl for partaking in the thesis committee and for their efforts to assess the work that I have conducted. My gratitude also goes out to my colleagues and fellow thesis interns at HARDT for their inspirational attitudes and the enjoyable time. It has been a pleasure to work with a motivational and engaging group of engineers.

I would lastly like to thank my mother for her relentless support and encouragement. Without her, I would not have had the opportunities which have led to this accomplishment.

F.T.H. Wong
Delft, May 2018

Summary

Increasing environmental concerns paired with the rising demand of high-speed transportation motivate the study and development of alternative, unconventional transportation methods. One such example is the Hyperloop, a newly proposed mode of passenger and freight transportation.

Hyperloop comprises pods that are propelled through a partially evacuated tube at velocities of $300m/s$. These pods are accelerated by means of a magnetic linear accelerator, while being levitated by electromagnets. Passengers can enter and exit the pods at stations located either at the ends of the tube, or branches along the tube. The Hyperloop is meant to have several key benefits over conventional (public) transportation systems, with the most important ones of it being significantly more energy efficient, faster and cheaper for travel distances of up to approximately $2000km$. Air travel would remain the most efficient means of transport for 'long-haul distances', cost-wise, since the infrastructural costs of the Hyperloop would rise tremendously if a tube system were to be constructed for those stretches.

Within the tube, the low pressure environment consequently leads to a low air density, which in turn results in a significant reduced amount of drag compared to vehicles travelling at the same speeds. Although the pods are intended to travel at pressures of approximately 0.1% of the atmospheric pressure, the remaining air within the tube still necessitates a careful aerodynamic design and analysis of the pod. The movement of the pod through a (confined) low pressure environment combined with transonic speeds compose a unique flow regime that is rarely encountered, and as such also poses its own unique fluid dynamic challenges. Coping with the Kantrowitz limit which is associated to choked flow is one such example.

The objective of this research is to develop an aerodynamic shape optimization procedure for a Hyperloop pod, which is realized by developing a low-fidelity aerodynamic solver coupled to an optimization scheme. The solver is first of all capable of analyzing axisymmetric pod geometries, where distributions of flow parameters are predicted as well as the total aerodynamic drag as a main figure of merit. Secondly, the solver is implemented in an optimization routine which is capable of producing a pod shape that minimizes the aerodynamic drag compared to a baseline geometry. This baseline pod is based off a combination from literature findings regarding aerodynamic pod shapes and functional top level requirements set by HARDT Hyperloop. The solver is validated by means of results obtained with Computational Fluid Dynamics simulations based on Reynolds-Averaged Navier-Stokes equations, where a two-equation turbulence model is employed.

The solver is based on the assumption that the flow through the tube and along the pod can be modeled as if it were flowing through a nozzle. It is furthermore assumed that the flow field properties are uniform across each specific longitudinal cross-section within the tube. As such, the flow is modeled and classified as a quasi-one-dimensional nozzle flow. To allow for a computationally efficient means of analyzing a high number of pod shapes, the geometry is parameterized by means of the class-shape-function transformation method, allowing the entire geometry to be described by 24 design variables. These variables are altered by the optimizer, where use is made of a gradient-based sequential quadratic programming algorithm.

The solver solutions agree well with the numerical results when comparing flow distributions close to the tube wall. This accuracy is less pronounced when the results are compared to the distributions directly over the pod surface. The implications of the quasi-one-dimensional flow assumption are apparent. Nonetheless, the overall trend of aerodynamic parameters is well captured, as well as the prediction of the total aerodynamic drag of the pod.

The optimization resulted in a drag reduction of 11.2%, from $4.08kN$ to $3.63kN$. The pod length was shortened from $49m$ to $47.6m$, mainly due to a reduction in nose length. Since the top level requirements yield an operating condition in which the Kantrowitz limit is violated, the presence of choked flow is imminent. A nose that is as short as possible is therefore beneficial since the presence of a high pressure peak in front of the pod is inevitable. In contrast, the tail has been elongated with the introduction of a concavity, allowing for a more gradual flow expansion and a relieved choking effect.

Contents

List of Figures

List of Tables

List of Abbreviations

1D	One-dimensional
2D	Two-dimensional
3D	Three-dimensional
CFD	Computational Fluid Dynamics
CST	Class Function Shape Function Transformation
DNS	Direct Numerical Simulation
EVM	Eddy Viscosity Model
FGC	Fictitious Gas Concept
GA	Genetic Algorithm
HTT	Hyperloop Transportation Technologies
LES	Large Eddy Simulation
Maglev	Magnetic Levitation
NASA	National Aeronautics and Space Administration
PDE	Partial Differential Equation
RAND	Research and Development
RANS	Reynolds-averaged Navier-Stokes equations
RSM	Reynolds Stress equation Model
SIMPLE	Semi-Implicit Method for Pressure-Linked Equations
SOU	Second Order Upwind
SST	Shear Stress Transport
SQP	Sequential Quadratic Programming

List of Symbols

Roman Symbols

a	Acceleration	m/s^2
A	Area	m^2
C_D	Drag coefficient	-
C_f	Friction coefficient	-
C_p	Pressure coefficient	-
C_v	Specific heat at constant volume	J/kg·K
D	Drag	N
e	Specific energy	J/kg
E	Energy	J
g	Gravitational constant	m/s^2
g_i	Inquality constraint	-
h_i	Equality constraint	-
k	Turbulence kinetic energy	J/kg
k_{eff}	Effective thermal conductivity	W/(m·K)
J	Optimization objective function	-
K_b	Boltzmann constant	J/K
K_n	Knudsen number	-
M	Mach number	-
$\dot{m}$	Mass flow rate	kg/s
p	Pressure	Pa
q	Dynamic pressure	Pa
R	Gas constant	J/(kg·K)
Re	Reynolds number	-
S	Shear rate	1/s
T	Temperature	K
u	Flow velocity	m/s
V	Velocity	m/s
y^+	Non-dimensional wall distance	-

Greek Symbols

β	Blockage ratio	-
γ	Ratio of specific heats	-
δ	Kronecker delta	-
Δ	Difference operator	-
ϵ	Turbulence dissipation	m^2/s^3
ζ	Parametrized curve	-
θ	Angle	°
λ	Molecular mean free path	m
μ	Dynamic viscosity	Pa· s
ν	Kinematic viscosity	m^2/s
ν_T	Eddy viscosity	Pa·s
ρ	Density	kg/m^3
σ	Prandtl number	-
τ	Shear stress	N/m^2
ϕ	Velocity potential	m$^2/s$
Ψ	Volumetric flux	m^3/(s· m^2)
ω	Specific turbulence dissipation rate	1/s

Subscripts

0	Initial conditions
∞	Free-stream conditions
i	i^{th} vector element
n	n^{th} vector element
T	Total conditions

Superscripts

$*$	Sonic throat conditions
^	Unit vector
$\rightarrow$	Vector notation
L	Lower
U	Upper

Miscellaneous

$\neq$	Not equal to
$\ll$	Much smaller than
$\leq$	Less than or equal to
∂	Partial derivative
$^-$	Vector notation
∇	Vector differential operator

1

Introduction

1.1. Rationale

It is evident that many sectors focus on becoming more environmentally friendly. This is due to the depletion of natural resources, but this focus also offers many benefits in terms of marketing, public relations and costs. One of these sectors which is inspiring and striving to become greener is the transport sector.

The detrimental effects on the environment due to transportation is raising concerns, mainly because of the ever growing travel networks and developments within this sector, triggered by the continuously rising demand of interconnected, high-speed travel. It is forecasted that by 2050, 41% of the world traffic market share (and 71% in North America) is projected by high-speed transport [1]. Along with the exploitation of non-renewable energy sources, regulative authorities are necessitated to set rules and regulations that become more stringent by the decade with a focus on reducing noise and greenhouse gas emissions. In light of this and the aforementioned rising demand of high-speed transportation, a new means of transport which adheres to these demands and regulations is necessary.

Hyperloop is a new transportation method that can comply to these regulations while showing significant benefits over conventional transportation methods. The system comprises passenger pods that are propelled through a tube where the pressure is reduced to 0.1-1% of the atmospheric pressure [2]. The reduced pressure consequently means that the density is also decreased for the same temperature, since these are then linearly proportional to each other. This low density results in a significantly lower amount of aerodynamic drag experienced by the pods. The pods are levitated by electromagnets while being propelled by a magnetic linear accelerator to an intended operating velocity of $300m/s$.

Though the Hyperloop is intended to have a direct 'A-to-B' connection, the transportation mode highly resembles transportation by means of train. At the same time, it tackles the goal of having a high operational speed ($M_{operational} \approx 0.88$) while maintaining a high energy efficiency, thereby resembling a typical aerospace design problem. It can thus be regarded as a combination of train and air transportation, merging ground transport and aerospace technologies to attain a fundamental new capability. The result is a high-capacity mode of transportation that is optimized for emission reductions while travelling at airliner speeds. The Hyperloop also addresses NASA's research goals for growth in demand, sustainability, and technology convergence for high-speed transport [3].

The aerodynamic characteristics play a significant role in the overall performance of a vehicle. Evidently, this is also the case for the Hyperloop, where finding an adequate aerodynamic design of the pod is necessary in order to reach the earlier mentioned airliner speeds while simultaneously fulfilling the low energy requirements. However, the design of the pod is not an external aerodynamic problem as is with the aerodynamic design of aircraft, trains or automobiles for instance.

Since the pod is confined by the low pressure tube, it has become an internal aerodynamic problem and as such, unveils new fluid dynamics challenges which need to be carefully addressed during the design process. The physical challenge that is the most critical is governed by the Kantrowitz limit, and is typical for internal transonic aerodynamics [4]. Violation of this limit will result in a significant amount of drag increase, which could nullify all promised potential benefits of the Hyperloop.

It is therefore of paramount importance to carefully investigate these aerodynamic related challenges in order to realize the intended performance benefits of the Hyperloop. This thesis project comprises an investigation on these problems in order to develop an aerodynamic design and optimization procedure for the Hyperloop pod.

1.2. Research Objective

The main goal of this research project is to find a shape for the Hyperloop pod which minimizes the aerodynamic drag compared to a baseline pod geometry and to analyze the flow behaviour around the pod in general, thereby contributing to the further development of the Hyperloop.

This project furthermore aims to introduce and contribute to the knowledge on the aerodynamic performance of vehicles in rarefied, internal environments. From the research proposal, it became clear that performing optimization routines focusing on aerodynamic phenomena that are critical for the Hyperloop is the next step to be undertaken after preliminary sizing processes have already been conducted. From previous investigations, it also became clear that the main Hyperloop concept is feasible but refinements and further investigations are a necessity [5]. Therefore this project is intended to delve into a more detailed analysis of the Hyperloop pod, focusing on the aerodynamic aspects.

The goal and objectives of this project are to be realized by developing and utilizing a simplified aerodynamic solver. The outputs will be compared against results of Computational Fluid Dynamics (CFD) simulations in order to validate the aerodynamic solver. Additionally, the solver can be utilized to investigate the effect of external parameters, such as the tube radius or internal tube pressure, on the aerodynamic drag. As such, the solver allows for the further exploration of the aerodynamic characteristics for a relative wide and unexplored design problem that still has a relative wide and unexplored design space.

This research project is carried out at HARDT Hyperloop, a company that is realizing and commercializing the Hyperloop concept. Its vision is to have on-demand, high-speed transportation for everyone and to create a world where distances do not matter; a world where the freedom exists to live and work wherever one wants.

HARDT Hyperloop aims at providing a high-speed tube transportation system that is, in comparison to current modes of transportation, safer, faster, cheaper, more efficient, more convenient, more resistant to weather and less disruptive to those along the route. It is an origin-to-destination system where vehicles do not have stops in between. It is supported by the concept that all vehicles share the main tube during high-speed travel and can get on and off from their departure or arrival station through 'exit ramps', where the tube splits off in branches. The system should be ideal for travelling between the distance of $50km$ to $2000km$ in 5 to 120 minutes [6]. The system of HARDT comprises four main elements: tube and track, vehicle, station and related services.

1.3. Research Questions

Following from the rationale and the main objective of this research project, the main research question is evident: *What is the optimal shape of a Hyperloop vehicle?* In order to answer this question, sub-questions are formulated that guide the process in solving the main question:

- What are the key parameters for the aerodynamic design of the pod and how are they related to the generation of aerodynamic drag?

- What are the key physical phenomena that contribute to the drag generation of the pod?

- What are the main (valid) assumptions for a simplified aerodynamic solver applicable to this fluid dynamic problem, and what are their implications on the governing fluid dynamic equations and the real physical problem?

- What are the consequences/changes of the optimized shape compared to the baseline?

1.4. Outline

This report starts-off with a literature review regarding the aerodynamic aspects of the Hyperloop, as well as fluid dynamic analyses and optimization techniques for vehicle aerodynamic shape optimization.

The methodology that was developed and carried out in order to arrive at an aerodynamic solver for the shape optimization is presented and discussed in Chapter 3. Thereafter, the solver is validated by means of CFD analyses, which will be discussed in Chapter 4. The model is then used to perform an optimization and to assess the influence of different parameters on the aerodynamic drag, which is done in Chapter 5. Finally, the report is concluded and recommendations are given for possible future work based on this research project in Chapter 6.

2
Literature review

It is evident that there is little to no literature available on the Hyperloop specifically focusing on its aerodynamic aspects, since the concept is relatively new and in its first developing stages. Furthermore, the related technology itself is still at a proof of concept stage. Nonetheless, the aerodynamic considerations for the Hyperloop can be related to several systems and flow models that already have been developed or at least analyzed for a relative longer period, for instance the analysis of magnetic levitation (Maglev) trains placed in a confined low pressure environment. Therefore, this literature review will be based on these considerations when gaining background knowledge regarding the state-of-the-art. This chapter will start-off with an introduction to the flow field that a Hyperloop pod is exposed to, and the various methods of solving the main flow parameters in such an environment. Since CFD analyses are to be conducted within the scope of this research project, a section is dedicated to the theory of CFD which is applicable for the analysis of a Hyperloop pod, introduced and discussed in Section 2.5. Thereafter, in Section 2.6, different aerodynamic shape optimization methods that are the most common are introduced and touched upon. Finally, the chapter is concluded with a brief discussion and conclusion on the main literature findings in Section 2.7.

2.1. Flow Regime

The Hyperloop pod travels in an unconventional flow regime: high-subsonic Mach numbers with relatively low Reynolds numbers. The low Reynolds number is a consequence of the low density environment, which in turn results from the low internal tube pressure. The Reynolds number for this flow is in the order of 10^5, implying that the flow will transition from a laminar to turbulent flow somewhere over the pod surface [7], or, a transition point exists over the pod surface.

Both laminar and turbulent flows will yield different performance characteristics and it is therefore important to carefully capture the transition point. Furthermore, at these low Reynolds numbers the boundary layer is prone to separation as the boundary layer is relatively thick [8]. Boundary layers separate rather easily when a relatively large adverse pressure gradient is present and the boundary layer has thickened considerably. These phenomena all lead to a significant amount of increased drag. A proper aerodynamic design is needed to reduce or avoid separation as much as possible in order to keep the associated pressure drag to a minimum.

Finally, the near vacuum environment paired with a transonic flow in a confined area all contribute to unique flow conditions affecting the design of the pod. The most notable effects will be described in subsequent sections.

2.1.1. Kantrowitz Limit

Since the pod is confined by the tube, the design problem is defined as an internal aerodynamic problem and as such poses its own challenges and phenomena that need to be addressed. The most significant aerodynamic design criterion for vehicles encountering transonic flows in a confined space is the Kantrowitz limit [9], which constraints the operability of the system. Violating this limit can possibly lead to a three-fold increase in the drag coefficient of the pod [7].

The Kantrowitz limit is a theoretical concept that refers to the physical phenomenon of choked flow, which forms a limiting factor for the Hyperloop performance when it occurs. This happens when the local air flow reaches a Mach number of 1, imposing sonic conditions. While the pod is travelling at high-subsonic speeds, these sonic conditions can be easily reached as the flow is accelerated in the bypass region between the pod and the tube. When the pod speeds up further, a large pressure increase in front of the pod builds up because the mass flow that can go around the pod is limited.

Choked flow is associated with the Venturi effect and is a limiting condition where the mass flow cannot increase further downstream, even when the downstream pressure is further decreased. The air cannot bypass the pod and is accumulated in front of the pod. The pod then acts as a syringe, pushing the column of air ahead of it through the tube. This phenomenon occurs at the minimum section (throat) between the pod and the tube [10] and it directly imposes a relationship between the pod size and tube size. These two dimensions are not independently variable and have to be coupled when designing the Hyperloop pod.

In general, avoiding the exceedance of the Kantrowitz limit can be done in two main ways. The first option is to decrease the ratio of cross-sectional areas between the pod and tube - also known as the blockage ratio ($\beta = A_{pod}/A_{tube}$) which allows more air to bypass the pod at a lower velocity. The second option is to make use of a compressor embedded in the pod that compresses air entering through the front of the pod. This compressed air is then fed through a duct in the pod which finally leaves the pod through a nozzle at the rear. This second option is the one that was proposed in the original introduction of the Hyperloop [2].

2.1.2. Aerodynamic Disturbances

In conventional ground transportation systems, the presence of shockwaves and their related implications are rarely considered due to the relatively low operating speed. Shockwaves occur when the local flow velocity exceeds the speed of sound, and are characterized by an abrupt change in pressure, temperature and density of the flow. The occurrence of shockwaves is prevalent for the Hyperloop system as the pods are intended to travel in a domain of mixed subsonic and supersonic flow, also termed as a transonic flow regime. The shock can for instance be a recompression shock, which terminates a preceding supersonic region.

For example, it was found that at a blockage ratio of 0.5 and an operating speed of M = 0.57, (weak) shockwaves are already observed at the rear of a so-called vacuum train as seen in Figure 2.1 [11]. Furthermore, normal shockwaves coexist with oblique shockwaves that are generated by the interaction and continuous reflection between the tube and vehicle walls. However, for the same speed but at lower blockage ratio ($\beta = 0.25$), no shocks were observed. Depending on blockage ratio and operating speeds, the flow can locally reach speeds of approximately Mach 2.5.
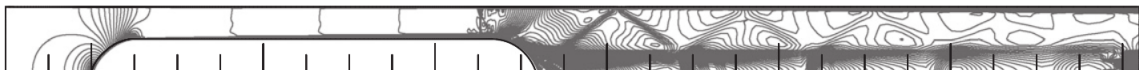
Figure 2.1: Presence of shockwaves at M = 0.57

While shocks can be present in design conditions for wings, on non-lifting bodies such as a Hyperloop pod, the presence of shocks are undesired and should be avoided [10]. This is because shockwaves produce drag due to the total pressure loss that is associated to shockwaves [12]. Therefore, next to the general pressure drag and friction drag, a third type of drag (which in essence can be regarded as an additional pressure drag term) is introduced with shockwaves: wave drag.

Next to the additional drag, shockwaves can cause the boundary layer to separate at the foot of the shock, and separation is to be avoided as it significantly increases the pressure drag. When boundary layer separation occurs, a wake is created between the body and the continuous streamlines. Consequently, a large deficiency in momentum is present in the wake which can give rise to a significant amount of drag. In addition to the drag rise due to flow separation, the pressure distribution over a body is also altered significantly [13]. However, since the internal tube pressure is very low and the shock effect decreases in proportion to the ambient pressure level, the presence of shocks are not as critical as would be in a standard open environment at sea-level. It is for these considerations that both the internal tube pressure and the blockage ratio should remain as low as possible in order to enhance the energy efficiency. It should be noted that these considerations are purely based on the

aerodynamic efficiency. Regarding the entire Hyperloop system, it is evident that the operating costs for instance would be negatively affected by a decreasing blockage ratio, which generally implies that the tube diameter has to increase.

Nevertheless, shockwaves directly affect the drag of a tube train in a detrimental manner which consequently results in an overall efficiency losses. It again shows how the operating speed is one of the limiting factors in the aerodynamic design of a Hyperloop pod. For future work, the design optimization of the vehicle shape is also needed for the control of the shockwaves [7, 14].

Hence, for a given operating speed and fixed propulsion system, a possible aerodynamic design strategy is one in which the aerodynamic drag due to shockwaves is reduced. Minimizing supervelocities on these components to prevent the onset of supersonic flow and associated shockwaves can be a design approach in finding an optimal aerodynamic shape for the Hyperloop pod.

2.2. Governing Design Parameters

Bodies in transonic flows generally experience drag to two main mechanisms: through wake forming due to the separation of the flow as previously described and through the generation of shockwaves. The skin friction drag in turn is a function of the shear stress and is mostly due to the viscous effects of a fluid. Every component of a body that is wetted by the flow will give rise to a friction drag component.

In general, the aerodynamic drag is quadratically proportional to the operating velocity of a vehicle, and is composed of the pressure drag and viscous drag that are dependent on the vehicle shape and length. For relatively short vehicles, the total drag is mostly composed by the pressure drag, while on an elongated vehicle such as a train, the total drag is dominated by the viscous drag to a large extent [15]. However, for a tube train this is the other way round. The main reason for this is that the internal tube pressure is very low compared to the atmospheric pressure at sea level. Furthermore, the pod can be regarded as a piston in a cylinder. The pressure drag is therefore the dominating component in the total aerodynamic drag. Besides the square of the train operating speed, the drag of a tube train system is linearly proportional to the internal tube pressure unlike a ground system. As an ideal gas is dealt with, a pressure change leads to a linearly proportional change in air density for a constant temperature, which yields the linear change in drag.

In a tube train system, the ratio between the pressure drag and viscous drag is approximately 10:1 when the blockage ratio is 0.25, but increases to 20:1 when the blockage ratio is 0.75 [11]. It shows how much the pressure drag is dominating, but more importantly shows that the ratio between these drags is highly dependent on blockage ratio.

It is found that the maximum operating speed (before choking occurs) is inversely proportional to both the blockage ratio and internal tube pressure. Again, it is evident that both internal pressure and blockage ratio should be minimized in order to enhance the aerodynamic efficiency. The blockage ratio can of course not be continuously minimized as it is limited by the maximum tube size, or equivalently the minimum vehicle size. An optimal value for this parameter therefore has to be found. A reasonable value for this ratio should lie within 0.25-0.7 regarding aerodynamic considerations [16].

From these findings it can be deduced that the three most important initial aerodynamic design parameters of the Hyperloop are: blockage ratio, internal tube pressure and pod operating speed. These parameters are coupled and have a large impact on one another. It is also found that the operating speed of the pod does not have a significant effect on the relationship between the blockage ratio and the internal tube pressure, which is to be expected since these are mainly external parameters. The total drag of a tube train with a fixed operating speed is linearly proportional to the internal tube pressure and is significantly affected by this [14, 17].

2.3. Preliminary Vehicle Shape Analysis

While the parameters described in the previous section are important to the overall drag of the system, the vehicle shape in itself of course also significantly impacts the aerodynamic performance. Intensive studies about the aerodynamic analysis and energy efficiency of a tube train system already date back to 1970, where a project was undertaken by the Transportation Bureau of the United Sates [18]. According to this study, the drag coefficient, C_D, of a tube train ranges from 0.015 to 0.11 when the vehicle nose and rear both have a semicircular shape. These coefficients were found for a Reynolds number in the order of 10^5 and a blockage ratio ranging from 0.125 to 0.5, comparable to the Hyperloop pod design conditions.

More extensive research has been conducted on different head and tail shapes of a Maglev train in an evacuated tube by Ma et al. [19]. In this study, a focus was laid on the pressure difference between the nose and tail of the vehicle, in essence the main driver of pressure drag. The different shapes that were investigated can be seen in Figure 2.2.
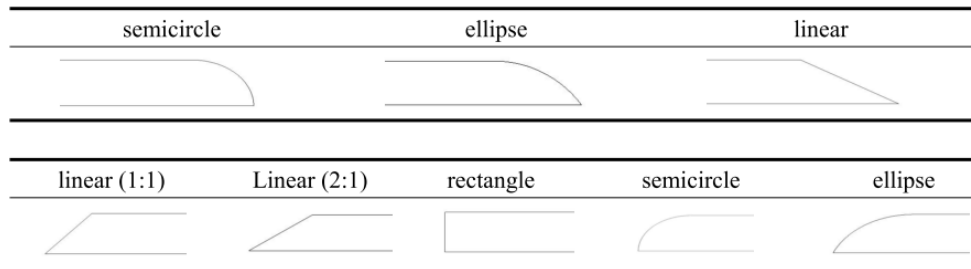

Figure 2.2: Investigated shapes for the head and tail of an evacuated tube train

It was observed that different head shapes of the tube trains do not cause a significant difference in aerodynamic drag effects. There was however a shape which can be regarded as the desired direction in searching for an optimal shape, which is the linear head design. The linear head yields the lowest drag amongst different investigated shapes. It was furthermore observed that the pressure difference increases with blockage ratio regardless of nose shape, and that the pressure at the head is directly affected by the tail type.

Regarding tail shapes, a blunt-shaped (rectangular) tail yields the lowest pressure difference for a blockage ratio of 0.25. However, under the blockage ratio of 0.36, the pressure difference of the train with this tail is greater than compared with a semicircle tail. It again shows that the blockage ratio is an important factor that has an influence on the 'optimal' shape, thereby affecting the pressure difference and ultimately the total drag of the vehicle. Finally, it was found that with increasing internal tube pressure, the effect of drag reduction by vehicle shape manipulation increases very slowly when the pressure is less than $1kPa$, but rapidly when the pressure is above $10kPa$ [20].

In another, more recent study (2017) on tube train shapes, it was observed that the pressure difference was lowest for a train with an elliptical head shape and a similar but more blunt tail when the air pressure was 100 Pa [14]. This combination dramatically reduced the amount of aerodynamic drag compared to other shape combinations. The simulated results showed that the shape of the pod significantly affects the aerodynamic drag. Furthermore, the energy usage is found to be relatively insensitive to pod length. Therefore, the system would scale favorably to much higher passenger capacities than originally proposed [21], mostly due to the relative low friction drag that comes as a cost for lengthening the vehicle. A general agreement can be observed regarding the different studies in which the tail of the train should be more blunt-shaped compared to the head. An optimal ratio between the nose length and vehicle diameter lies within the range of 1.5-2.5, according to a study which focused on nose and tail lengths of Maglev trains in an evacuated tube [22].

As mentioned before, the low Reynolds number environment can lead to boundary layer separation at relative ease. A study on a Hyperloop pod which is scaled down in size showed that for a head shape with an inflection point that is too pronounced, the boundary layer that is still laminar at that point already separates at relatively low adverse pressure gradients [7]. While the skin friction drag is low due to the laminar flow over the pod surface, the total drag is still high due to the relatively high pressure drag that results from the large wake starting from this inflection point. This laminar separation has to be prevented in order to reduce the amount of pressure drag.

Based on these findings, another possible design strategy could therefore be to transition the boundary layer to a turbulent one close to the front of the pod, such that higher adverse pressure gradients can be tolerated before separation occurs. It is known that turbulent boundary layers can tolerate higher adverse pressure gradients, with an increased friction drag as detrimental side effect. It however weighs up against the much higher pressure drag increase when the boundary layer separates. A key part to this aerodynamic design strategy is therefore to ensure that the transition point is moved in front of the so-called natural transition point close the nose area of the pod, or simply said to trip the

boundary layer. It must however be noted that the findings in this study were based on flow conditions that differ from the full-scale system, where Reynolds and Mach numbers of $6 \cdot 10^4$ and 0.3 respectively are considered (as opposed to $Re \approx 10^5$ and $M \approx 0.9$ for the full-scale system), implying that the flow behaviour regarding the separation past the inflection point do not necessarily have to hold for the full-scale pod.

2.4. Simplified Aerodynamic Model

Optimization problems require an analysis model to quantify the objective function and constraints. These analysis models are coupled to an optimization algorithm, which manipulates the design variables at every iteration. In most cases, the accuracy of the optimized solution is dependent on the analysis model.

A simplified aerodynamic model that is of relatively low computational cost is useful for rapid design iterations. While CFD analyses are more accurate in the prediction of flow fields and aerodynamic quantities, performing these for every design iteration are computational expensive and therefore inherently time inefficient. A simplified model will therefore be developed which will be coupled to an optimizer. A suitable aerodynamic shape optimization scheme will be followed, which will be introduced in Section 2.6.

2.4.1. Assumptions

A first step in developing a low-fidelity flow model is to make assumptions in order to simplify the governing equations and conditions. A possible methodology in developing such model is to base it on a quasi-1D flow assumption. This implies that different flow parameters are uniform along each section and vary primarily along one direction x for instance (i.e.: $A = A(x)$, $p = p(x)$, $\rho = \rho(x)$ etc.). Furthermore, the flow is assumed to be steady, inviscid and adiabatic. The gas is assumed to be an ideal gas. For accelerating flows (favorable pressure gradients), the idealization of isentropic flow is generally a realistic model of the actual flow behavior [23]. The flow is therefore assumed to be isentropic.

2.4.2. Continuum versus Free Molecule Flow

As mentioned before, the Hyperloop pods travel in an unconventional flow regime, where the low amount of air inside the tube is of particular interest. It is therefore required to verify whether the fluid can be modeled as a continuum, where each fluid element represents a large number of molecules. The mean free path, λ, is the average distance traveled by a particle (e.g. a molecule) between successive collisions with neighbouring molecules. If the scale of a certain body of influence denoted by d is orders of magnitude higher than λ, the flow will appear to this body as a continuous substance. The amount of collisions between the molecules and the body surface are at a sufficiently high frequency such that this body is 'not able' to distinguish the individual molecular collisions [24]. Such flow is accordingly termed as continuum flow.

On the contrary, if λ is in comparable order as the body scale, these collisions between molecules and body surface occur infrequently up to the extent where each individual impact can be felt by the body. Such flow is then termed as free molecular flow. If this is the case, statistical mechanics will have to be utilized to predict the flow behaviour.

One quantifiable way of determining whether a flow can be modeled as a continuum is through the Knudsen number [25]. This number is in essence the ratio between the mean free path of a molecule and a macroscopic length scale of interest. This number can be determined as follows:

$$K_n = \frac{K_b T}{\sqrt{2}\pi d^2 p L} \tag{2.1}$$

When $K_n \ll 1$, the fluid can be modeled as a continuum. Otherwise, molecular mechanics will have to be utilized for the analysis. For the flow regime that the Hyperloop pod encounters, the Knudsen number is in the order of 10^{-5} [4] which is well below the continuum threshold. Therefore, continuum mechanics are applicable for this aerodynamic problem.

2.4.3. Aerodynamic Forces and Moments

The aerodynamic forces and moments on every arbitrarily shaped body exposed to a fluid, no matter how complex they may be, is due to only two sources: the pressure and shear stress distributions over the body surface. For any arbitrary surface, the pressure is acting in a normal direction onto the surface whereas the shear stress acts tangentially to the surface.

The integration of the pressure and shear stress distributions over an entire body surface then leads to a resultant force and moment that both act on this body. This resultant force can subsequently be split into two components: lift and drag. Obtaining the shear stress and pressure distributions is therefore key in determining the overall aerodynamic performance. The main aerodynamic quantity of interest will be the drag for the case of a Hyperloop vehicle in the scope of this project.

2.4.4. Pressure Distribution over Non-Lifting Bodies

The Mach number and geometry of a vehicle directly affect the supervelocities over a non-lifting body. In high-subsonic conditions, the local velocity can exceed the speed of sound thereby creating shock-waves or expansion waves. The generation of these waves has a detrimental effect on the drag contribution as was already discussed before, which is why it is of paramount importance to understand the relation between geometries and associated supervelocities. The local velocity is directly tied to the pressure coefficient C_p. For an incompressible flow, a well-known expression that relates the two parameters is given by:

$$C_p = 1 - (\frac{V}{V_\infty})^2 \tag{2.2}$$

Alternatively, the pressure coefficient can be expressed as a function of Mach number:

$$C_p = \frac{2}{\gamma M_\infty^2}(\frac{p}{p_\infty} - 1) \tag{2.3}$$

This relation directly stems from Bernoulli's equation, which states that the square root of the local pressure is inversely proportional to the local velocity. Under the assumption that the difference between the local velocity and free-stream velocity is negligibly small (i.e. $V = V_\infty + \Delta V$ and $\Delta V / V_\infty \ll 1$), equation 2.2 can be reduced to:

$$C_p = -2\frac{\Delta V}{V_\infty} \tag{2.4}$$

This equation provides a relatively simple relation between the pressure coefficient and the super velocity, ΔV, over a body. This relation was applicable to a fluid particle along a streamline. A similar relation can be found when the perpendicular direction is considered along a curved streamline. Assuming inviscid, irrotational flow and that the dimensions of a fluid particle can be described by its length Δl and width Δw, the second law of Newton applied on this particle can be defined as [26]:

$$\frac{mV^2}{r} = (p + \Delta p - p)\Delta l \tag{2.5}$$

Furthermore, the pressure difference for a particle can be expressed as $\Delta p = (dp/dw)\Delta w$ with its mass $m = \rho\Delta w\Delta l$. Combining and substituting these expressions into equation 2.5 yields:

$$\frac{\rho V^2}{r} = \frac{dp}{dr} \tag{2.6}$$

From equation 2.6, it can be deduced that the pressure is increasing outward from the center of curvature. Additionally, a free body diagram of a fluid particle on a curved (convex) streamline is shown in Figure 2.3 [27].
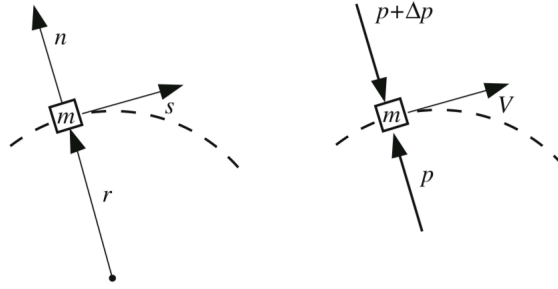
Figure 2.3: Geometrical definitions and pressure acting on a fluid particle on a curved streamline

Since the curve is convex, the normal vector n is in the same direction as r, consequently yielding a positive pressure gradient dp/dn. Since the pressure at a location far away from the wall should be equal to the free-stream pressure, it can be concluded that p at the wall is to be lower than this free-stream pressure. Therefore, it can be deduced that a convex shape leads to a pressure reduction, or consequently a negative pressure coefficient. The opposite is true for a concave shape, since the pressure gradient is negative by definition.

These findings can be combined with the earlier relation between local pressure and super velocity (equation 2.4). It can now be stated that a convex geometry leads to a positive value of ΔV, since C_p decreases. Convex geometries therefore lead to higher local velocities when compared to the freestream velocity. Similarly, concave shapes therefore lead to lower local velocity when compared to the free-stream velocity. Finally, it can also be stated that the larger the local curvature, the larger the amplification of the local supervelocities. These findings provide a fundamental (qualitative) analysis regarding the pressure distribution over the Hyperloop pod, which can possibly be a combination of convex and concave shapes.

2.4.5. Compressibility Effects

The qualitative relation between local curvature and supervelocity was based on an incompressible flow. As a Hyperloop pod is travelling in a transonic flow regime, compressibility effects need to be taken into account. While the derived relations still hold, the pressure coefficients are mostly affected in their numerical values due to compressibility effects. The compressible pressure coefficient can be related to the incompressible one through the well-known Prandtl-Glauert compressibility factor:

$$C_p = \frac{C_{p_{incompressible}}}{\sqrt{1-M_\infty^2}} \tag{2.7}$$

This factor not only gives a more accurate value of the pressure coefficient by means of a correction, it more importantly shows that the pressure coefficient, and thus local supervelocities, are related to the compressibility of air for a body in high-subsonic conditions.

Although the Prandtl-Glauert rule is simple to apply, it has been observed that this rule generally underpredicts experimental data [10]. This is why several improvements have been made regarding this correction of which one is the Karman-Tsien rule [28] given by:

$$C_p = \frac{C_{p,0}}{\sqrt{1-M_\infty^2} + \frac{M_\infty^2}{(1+\sqrt{1-M_\infty^2})} \frac{C_{p,0}}{2}} \tag{2.8}$$

This compressibility correction is more accurate due to the fact that non-linear aspects of the flow are accounted for, while the Prandlt-Glauert rule is purely based on linear theory. Comparable to the Karman-Tsien rule is Laitone's rule [29] given by:

$$C_p = \frac{C_{p,0}}{\sqrt{1-M_\infty^2} + \left[\frac{M_\infty^2(1+\frac{\gamma-1}{2}M_\infty^2)}{2}\sqrt{1-M_\infty^2}\right]C_{p,0}} \tag{2.9}$$

Laitone's rule is more recent than both aforementioned compressibility corrections and is also more accurate than the Prandtl-Glauert rule, but not necessarily than the Karman-Tsien rule.

Figure 2.4 shows the three presented compressibility corrections, where in the same figure experimental data is shown for the variation in pressure coefficient with free stream Mach number for a NACA 4412 airfoil [10].
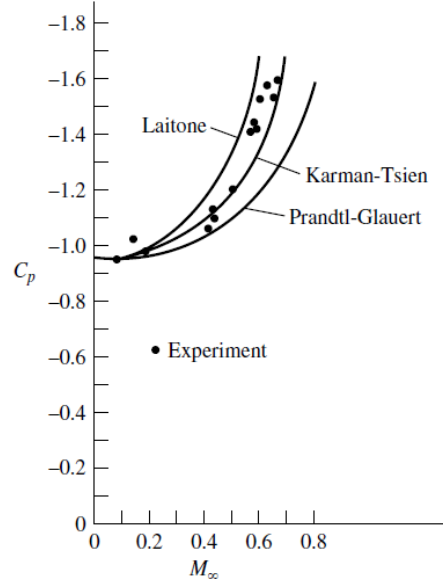
Figure 2.4: Three compressibility corrections compared with experimental results for a NACA 4412 airfoil

It can be observed that the Prandtl-Glauert rule underpredicts the experimental data as was stated, whereas the other two rules are more accurate. For the aerodynamic solver, the use of Laitone's rule or the Karman-Tsien rule is therefore desired.

2.4.6. Transonic Channel Flow

The flow behaviour around the pod can be modeled as a flow through a channel, with pod surface and tube wall posing as the channel walls. As such, the flow domain can be regarded as a supersonic (convergent-divergent) nozzle assuming that there will be a minimum section somewhere between the pod and wall surfaces. The velocity distribution around the pod can then be based on the area contraction between the inlet area and the (minimum) space between the tube wall and pod surface.

The area-velocity relation, directly following from the mass conservation principle, can serve as a starting point to solve the flow field. This relation gives a relative easy qualitative relation of whether a flow is accelerating or decelerating through a specific passage, similar to the discussion regarding concavities and convexities in the previous subsection. It can directly be concluded that a decrease in cross-sectional area leads to an increase in velocity and a static pressure drop for subsonic flow. This is the other way round for supersonic flow:

$$\frac{dA}{A} = -\frac{dV}{V}(1 - M^2) \tag{2.10}$$

As the flow is assumed to be isentropic, stagnation conditions are constant throughout the flow domain. The isentropic relations can then be used as a reference in order to obtain local properties, which for the pressure, temperature and density are given as such respectively:

$$\frac{p_t}{p} = (1 + \frac{\gamma - 1}{2}M^2)^{\frac{\gamma}{\gamma - 1}} \tag{2.11}$$

$$\frac{T_t}{T} = 1 + \frac{\gamma - 1}{2}M^2 \tag{2.12}$$

$$\frac{\rho_t}{\rho} = [1 + \frac{\gamma - 1}{2}M^2]^{\frac{1}{\gamma - 1}} \tag{2.13}$$

Finally, from the continuity equation given, a relation between the local area and throat area can be derived from which the local Mach number can be estimated:

$$\frac{A}{A^*} = \frac{1}{M}\left[\frac{1 + \frac{\gamma-1}{2}M^2}{\frac{\gamma+1}{2}}\right]^{\frac{\gamma+1}{2(\gamma-1)}} \tag{2.14}$$

Equations 2.11 to 2.14 form the set of equations that are fundamental to the analysis of one-dimensional (1D) isentropic flow through a nozzle. Combining the expression for the pressure coefficient given earlier by equation 2.3 with the isentropic relation given by equation 2.11, a relation can be established between the free-stream Mach number, local Mach number and pressure coefficient [27]:

$$M^2 = \frac{2}{\gamma - 1}\left[\frac{1 + \frac{\gamma-1}{2}M_\infty^2}{(1 + \frac{1}{2}\gamma M_\infty^2 C_p)^{\frac{\gamma-1}{\gamma}}} - 1\right] \tag{2.15}$$

These sets of equations derived from the conservation principles can be used in order to predict the pressure distribution.

2.4.7. Panel Method

Aside from the transonic channel approach, a panel method can also be developed in order to predict the aerodynamic properties of the Hyperloop pod. In such a method, the surface is divided into straight lines between surface contour points, which are termed - as its name suggests - panels. This method relies on the superposition of singularities on each of these panels. A piecewise variation of the vorticity on discrete segments of the vehicle surface is sought for. An example of such discretization with a vorticity distribution applied on an airfoil is shown in figure 2.5 [30].
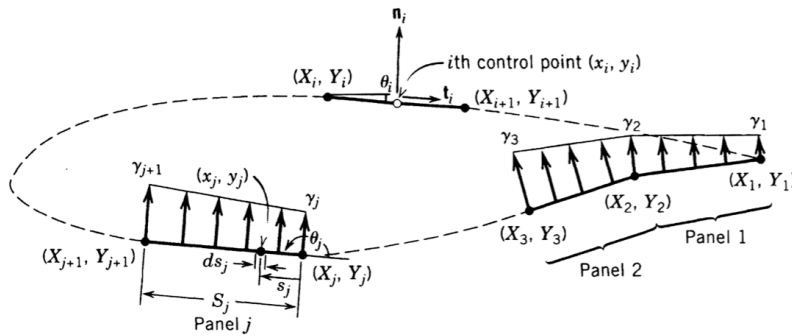
Figure 2.5: Replacement of an airfoil by vortex panels of linearly varying strength

Panel methods are not restricted to the use of a vortex singularity to represent a certain surface. Source and doublet singularities may also be used. This method requires large sets of algebraic equations to be solved simultaneously, generated by the tangency-boundary condition. There are different types of panel methods, but they all follow the same general steps [31]:

1. The first step is choosing the number and type of singularities, where each singularity has an unknown strength. For example, if N number of singularities are present, there are N unknown strengths. Therefore, N equations are needed.

2. Discretizing the aerodynamics surface into N panels or segments. The panels do not necessarily need to have the same size, but it can reduce computational time if they are. The panels should be concentrated in regions where the variables are expected to undergo rapid changes. This most often happens in regions of rapid geometry change. For example, at the head and tail of the Hyperloop pod, relative large curvature changes are expected and as such, more panels should be clustered in those regions.

3. Placing the control points. In solving a differential equation, the general solution must be generated where boundary conditions are applied for the specific case. The panel-solution method

is based on satisfying the surface-tangency boundary condition as mentioned. Since there are N unknowns, this boundary condition then has to be satisfied at N points on the surface. These N points are the so-called control points, and placement follows logically similar to the placement of the singularities.

4. Writing one equation for each control point. Here, the influence of all of the singularities and the free-stream at a fixed control point is summed. Then, it is required that the net local velocity is tangent to the surface at that control point or, equivalently, that the normal component of velocity at the control point is zero. To accomplish this, the relative position of the control point relative to the location of all of the singularities is required, as well as the geometrical slope of the surface. In addition, it must be decided how the singularities are to be distributed on their respective panels. So-called higher-order vortex panel methods may use a curved panel. These methods also represent the vorticity as a linear or nonlinear variation along each panel. In general, higher-order panel methods achieve greater accuracy than using combined singularities on flat panels but at the expense of a more complicated formulation and generally with additional computation time required.

5. Imposing the Kutta condition (if necessary). To produce a realistic solution, lifting airfoils with a sharp edge require the Kutta condition; other geometries, such as ellipses and cylinders, do not. The Kutta condition is a principle that holds for steady-flows. Briefly said, the condition is used to ensure that the flow at the trailing edge is smooth, implying that the vorticity at the trailing edge is to be zero. By imposing this condition, one of the equations discussed in the previous step can be omitted, thereby reducing the required number of control points by one. It is very well possible that this condition should be imposed as well in the analysis of a Hyperloop pod, as it is possible that the pod geometry ends in a sharp tail.

6. Finally the system of equations generated by Steps 4 and 5 can be solved. Solving for N unknown singularity strengths requires the solution of a full N by N matrix. Evidently, the more panels that are used (i.e., the larger the value of N), the more accurately the method represents the continuous vorticity distribution along a continuous surface. This can lead to more accurate results, however with an increased computational time as cost.

The solution to this method will initially be inviscid (potential) flow predictions, leading only to a prediction of lift. In order to make this method relevant for the Hyperloop pod analysis, the viscous component is to be added, which leads to the prediction of drag. This can simply be achieved by introducing a boundary layer theory.

2.5. Theory of Computational Fluid Dynamics

In the scope of this thesis project, CFD simulations are performed in order to verify the simplified aerodynamic solver. CFD is extensively used for analysis and design of engineering applications, and is a branch of fluid mechanics that numerically solves and analyzes problems involving fluid flows [32]. Some of these numerical methods are finite element, finite difference, and finite volume methods that are using spatial and time discretizations. The goal of any CFD simulation is to study details of a particular fluid dynamics phenomena in a controlled environment. In this section, the governing equations of fluid dynamics are presented. Afterwards, turbulence modelling is discussed with respect to applications on the Hyperloop. Next, boundary conditions and mesh generation are discussed and an overview of CFD on tube train applications will be presented.

2.5.1. Mathematical Model of Fluid Dynamics

The starting point of any numerical method is a mathematical model, i.e. the set of the governing equations of fluid dynamics along with the boundary conditions [33]. These fundamental governing equations form the cornerstones of every CFD model. These equations are the continuity, momentum and energy equations, which are mathematical representations of the following three physical principles respectively:

1. conservation of mass

2. Newton's second law (F = ma)

3. conservation of energy

The governing equations that follow from these laws will be be briefly described and will be given in their conservation form: the form where the control volume is fixed in space with the fluid moving through it. This results in the equations being in their partial differential equation form.

From the first physical principle, the continuity equation follows directly and is given by:

$$\frac{\partial \rho}{\partial t} + \nabla \cdot \rho \underline{u} = 0 \tag{2.16}$$

Following from Newton's second law, the momentum equations can be derived which states that the temporal change of the linear momentum of a (material) fluid element equals the sum of the forces that act on it. For a fluid element, the forces acting on it can be divided into two sources: body forces (e.g. gravity, electromagnetic forces) and surface forces due to the pressure and shear stress distributions as was mentioned earlier. The momentum equation can then be defined as:

$$\frac{\partial(\rho u_j)}{\partial t} + \frac{\partial(\rho u_i u_j)}{\partial x_i} = -\frac{\partial p}{\partial x_j} + \frac{\partial \tau_{ij}}{\partial x_i} + \rho f_j \tag{2.17}$$

where τ_{ij} represents the shear stress, which for a Newtonian fluid is given by:

$$\tau_{ij} = \mu \left(\frac{\partial u_i}{\partial x_j} + \frac{\partial u_j}{\partial x_i} \right) - \frac{2}{3} \mu \frac{\partial u_k}{\partial x_k} \delta_{ij} \tag{2.18}$$

A Newtonian fluid is one in which the viscous stresses that arise from the flow are linearly proportional to the local strain rate (i.e. $\tau \propto \frac{\partial V}{\partial t}$) at every point within the fluid domain [34]. For the vast majority of all aerodynamic problems, the fluid can be assumed to be Newtonian [32].

The final conservation law is that of energy. The physical law states that the total energy of a closed system is conserved. Energy can neither be created nor destroyed, but rather can be transformed from one form to another. Applying this law to a finite control volume, the following equation is established:

$$\frac{\partial}{\partial t}(\rho E) + \frac{\partial}{\partial x_j}(\rho u_j E + u_j p + q_j - u_i \tau_{ij}) = \rho g_j u_j \tag{2.19}$$

As mentioned, the above equations form the cornerstone for each CFD model. However, additional equations are required in order to obtain all the flow-field variables, as there are a total of 5 equations and 6 unknowns.

In general, it is reasonable to assume the gas behaves like a perfect gas. For such gases, the equation of state holds and is given by:

$$p = \rho R T \tag{2.20}$$

However, by introducing a sixth equation, a new unknown T is introduced which is the temperature. A final, seventh equation can be provided in order to close the entire system. This final equation is valid for a calorically perfect gas:

$$e = c_v T \tag{2.21}$$

Historically, the momentum equations in the three spatial directions for a viscous flow were identified as the Navier-Stokes equations. However, in modern CFD nomenclature, the Navier-Stokes equations have been expanded into the entire set of equations that was presented in this section. Therefore, equations 2.16 to 2.21 are the so-called Navier-Stokes equations and form the mathematical model behind the CFD model.

2.5.2. Turbulence Modelling

The Reynolds numbers that are encountered in the Hyperloop flow regime are still too high for Direct Numerical Simulation (DNS) to be a viable option, given the state of the current computational power and for the coming few decades [35]. DNS attempts to obtain a numerical solution to the unsteady Navier-Stokes equations, and is (currently) only applicable to relatively low Reynolds number flows.

The main limitation is the spatial grid and time scale requirements in order to capture all important motions in a turbulent flow.

Turbulence is a fluid flow phenomenon which can mainly be characterized by unsteadiness, irregular fluid motions on a wide physical scale range and rapid mixing. For the anticipated future, real-life fluid dynamic problems still require turbulence models in order to solve these. Reynolds-Averaged Navier–Stokes (RANS) equations combined with turbulence modelling provide an adequate model of turbulent flow effects. Modelling the flow behaviour in such fashion mainly provides additional momentum transfer by means of Reynolds stresses, although heat and mass transfer are also enhanced by the presence of turbulence. In CFD simulations for the tube trains and Hyperloop pods, RANS-based CFD is the main method in modelling the aerodynamic characteristics (as opposed to DNS and LES). These equations are based on Reynolds decomposition, which implies that a quantity is decomposed in a time-averaged and a fluctuating quantity:

$$u(x,y,z,t) = \bar{u}(x,y,z) + u'(x,y,z,t) \tag{2.22}$$

In this equation, the overbar represents the time-averaged quantity, whereas the prime represents the fluctuating quantity. The RANS equation can then be given as:

$$\frac{\partial \langle \underline{u} \rangle}{\partial t} + \nabla \cdot (\langle \underline{u} \rangle \langle \underline{u} \rangle) + \frac{1}{\rho} \nabla \langle p \rangle - \frac{1}{Re} \nabla \cdot \nabla \langle \underline{u} \rangle = -\nabla \cdot \langle \underline{u}' \rangle \langle \underline{u}' \rangle \tag{2.23}$$

In the RANS equation, the term $-\langle \underline{u}' \rangle \langle \underline{u}' \rangle$ is equal to τ_{ij} which is also known as the Reynolds stress tensor. This term is non-linear and is responsible for the fact that there are more unknowns than equations available [32]. This lack of equations is also known as the closure problem. Therefore, the Reynolds stress term needs to be solved with empirical approximations, which has led to the creation of numerous so-called turbulence models. These models serve the purpose of exactly what the name implies: using a model to predict the effects of turbulence. The turbulence models can generally be divided into two categories: Eddy Viscosity Models (EVM) and Reynolds Stress Models (RSM).

The main observation made in EVMs is the fact that turbulence leads to momentum exchange between fluid elements. The Reynolds stress is assumed to be proportional to a parameter called the eddy viscosity v_T:

$$-\langle \underline{u}' \underline{u}' \rangle = 2 v_T S_{ij} - \frac{2}{3} \delta_{ij} k \tag{2.24}$$

As such, the six independent components stemming from the Reynolds stress are now reduced to one scalar field v_T. This parameter can be expressed as a function of the mean velocity field in different ways, which thus leads to different models [36]. The eddy viscosity is a field quantity and is not to be confused with the kinematic viscosity which is a material property.

RSMs in turn, attempt to directly solve the model transport equations for all components of the unknown Reynolds stress tensor [37]. The model transport equations involve approximations of higher-order correlations and the dissipation rate tensor. As such, RSMs are able to account for complex interactions in turbulent flow fields and are by design superior to EVMs for flows with strong streamline curvature and for secondary flow structures induced by turbulence. The main reason is due to the elimination of the assumption that the turbulent stress is related to the mean shear stress. At the same time however, the six additional partial differential equations result in a too high computational cost for engineering applications. RANS equations yield sufficient accurate results in most general engineering cases.

There is a large number of turbulence models that each have their own pros and cons. Understanding their strengths and weaknesses is of paramount importance in order to achieve accurate results from CFD simulations. For brevity, only relevant models which have been applied to (Maglev) trains in an enclosed environment will be discussed. For these applications, the most common models found in literature are the $k - \epsilon$, $k - \omega$ SST and the Spalart-Allmaras model, which are all EVMs. These models will be briefly touched upon.

$k - \epsilon$ Model

The $k - \epsilon$ model is an EVM and is a so called two-equation model. It is one of the most widely used turbulence model in general, first proposed by Jones and Launder [38]. In this model, an equilibrium

is assumed between turbulence production and dissipation. This results in two partial differential equations (PDE) for the turbulence kinetic energy k and the dissipation rate ϵ.

Also in literature, where CFD simulations on the Hyperloop pod were performed, the $k - \epsilon$ model was the most common model amongst the three that are discussed. The model gives good results for both external aerodynamic problems as well as wall-bounded flows, which therefore makes it suitable for the Hyperloop pod simulations. A drawback of this model is its inaccuracy for cases where relative large adverse pressure gradients exist [35].

$k - \omega$ Model

The $k-\omega$ model was first proposed by David C. Wilcox [39], and is also a widely implemented turbulence model. Similar to the $k - \epsilon$ model, this is a two-equation model and attempts to predict turbulence by solving PDEs for the kinetic energy k and the specific turbulence dissipation rate ω. It is highly similar to the $k - \epsilon$ model but the small differences lead to a large effect on the difference between turbulence prediction.

Compared to the $k - \epsilon$ model, this model gives superior results for boundary layer flows and for flows with higher pressure gradients and where separation occurs. It is also possible to blend the two models, which leads to the SST model as proposed by Florian Menter [40]. This model is used for the design of the Massachusetts Institute of Technology Hyperloop pod competition for instance [7], as separation in their design is expected, and the $k - \omega$ model is known for handling separated flows well where large adverse pressure gradients exist.

Spalart-Allmaras Model

The final model which is commonly used for CFD analyses is the Spalart-Allmaras Model, and is based on a postulated transport equation for a viscosity-like variable which is also known as the Spalart-Allmaras variable [41].

This model is very robust compared to the previous two, and is computationally more efficient as it only requires one transport equation. It also generally leads to superior results for attached flows and for the prediction of the separation location, but is less suitable for the prediction of the reattachment location [42].

2.5.3. Numerical Model

The Hyperloop pod is set to run at a speed of $300 m/s$ or equivalently at a Mach number of 0.88 when the ambient temperature is assumed to be $288.15K$. Assuming that an ideal gas is dealt with, the equation of state holds and yields a scaling of the air density with the air pressure. The ambient pressure is assumed to be equal to the internal tube pressure, which for this design will be at $100Pa$.

As the Reynolds number of the flow field is in the order of 10^5, the presence of turbulence is expected, and a suitable turbulence model will have to be chosen in order to account for the turbulence production. As mentioned before, the k-ϵ model was the one that was chosen (approximately 90% of all cases) the most in literature.

A steady, viscous flow field was assumed in most cases. There are however also arguments that simulations involving the Kantrowitz limit has to be unsteady [7]. The presence of choked flow and the resulting pressure build-up is said to be an inherently unsteady phenomenon, which thus has a chance of preventing solution convergence if steady simulations are performed. A careful setup of the inlet and outlet boundary conditions is therefore necessary in order to take these phenomena into account.

The mass and momentum is defined through the total pressure at the inlet of the domain, which will be based off the Mach number and the static ambient pressure. This is also the case for the total temperature, which in general will also be prescribed for the inlet condition.

All solid surfaces require a wall boundary condition. When a fluid is in contact with a solid body, the fluid will not have any velocity relative to the body at the contact surface. This is also known as the no-slip condition for viscous flows and is a Dirichlet boundary condition [43]. This is applicable to the vehicle 'walls' for instance.

For the simulation of a vehicle travelling through confined spaces, it is common practice to assume that the object is stationary while the walls are moving at the speed of which the vehicle is intended to travel. Therefore, a tangential velocity of $300 m/s$ at the wall is to be prescribed.

2.6. Aerodynamic Shape Optimization

The main goal of all aerodynamic design methods, whether analytical, computational or experimental is to find an improved shape of an object in terms of an aerodynamic figure of merit compared to a previous shape while adhering to specified constraints. In the case for this thesis project, the main figure of merit is the aerodynamic drag or drag coefficient, which is to be minimized by means of an appropriate optimization scheme. Aerodynamic Shape Optimization methods can roughly be categorized into three basic categories:

1. Inverse surface methods

2. Inverse field methods

3. Numerical optimization methods (gradient based)

These methods have their own pros and cons and will be further touched upon in this section.

2.6.1. Inverse Surface Method

An inverse design method is one in which a geometry is modified until it produces a prescribed target distribution of a certain quantity. In most cases, the target distribution is a pressure or velocity distribution. For compressible flows, this method can be further sub-categorized into a transonic potential flow method and the Euler and Navier-Stokes method.

Transonic Potential Flow

One of the transonic potential flow methods is to replace the Neumann surface boundary condition, $\partial \phi / \partial n$, with a Dirichlet boundary condition ϕ within a CFD analysis code, first done by Tranen [44]. The velocity potential ϕ is obtained by integrating a desired target velocity distribution. The shape of the vehicle is then modified in an iterative fashion with the computed normal velocity through the surface.

Another common method is the extended Lighthill's method by McFadden and Garabedian [45]. This method builds forth on Lighthill's method [46], which comprised the design of a 2D profile in order to attain a desired pressure distribution. In the extended method, the flow equation is first solved for a certain given mapping h_o. The mapping is then updated by setting the surface speed to a desired target: $q = q_d$. The flow equation is subsequently solved for this new mapping h_1, and this process is repeated. Compared to the aforementioned method, it has an advantage due to the fact that it does not require modifications to the boundary conditions. All solutions will therefore remain valid throughout the optimization process.

Euler and Navier-Stokes

Another type of inverse surface method is the Euler and Navier-Stokes method, most commonly known through the work of Campbell [47]. A difference between the actual and a target pressure distribution is translated into adjustments of surfaces through the relationship of surface curvature and pressure for subsonic flows. For supersonic flows, the surface slope is taken instead of the curvature. These curvatures and slopes are calculated plane by plane:

$$\Delta n + \beta_1 \frac{\partial}{\partial x} \Delta n + \beta_2 \frac{\partial}{\partial y} \Delta n + \beta_3 \frac{\partial^2}{\partial x^2} \Delta n + \beta_4 \frac{\partial^2}{\partial y^2} \Delta n = \beta_5 \Delta c_p \tag{2.25}$$

In equation 2.25, Δn is the local normal surface displacement and β_i is the user specified quantities.

2.6.2. Inverse Field Method

With an inverse field method, the vehicle design is based on objectives or constraints that are imposed on the configuration surface but everywhere in the flow field. As its name suggests, it is also a method where the design is modified until a certain target is met.

One of these methods is proposed by Garabedian and Korn [48], which is based on a hodograph transformation. A hodograph transformation is one in which nonlinear partial differential equations are transformed into their linear counterparts [49]. It is achieved by interchanging the dependent and independent variables in the equation to achieve this linearity.

This method is useful for optimization procedures with a focus on shock control, as it can guarantee a shock-free flow field. It has been proven successful in the development of shock-free transonic airfoils, which could thus be a desired method as one of the mentioned design strategies for the Hyperloop pod was to prevent the generation of shockwaves. A disadvantage of this method is the fact that the method is not applicable to three dimensional flows.

Another popular inverse field method is the Fictitious Gas Concept (FGC) first introduced by Sobieczky [50]. The FGC is originally designed for potential flow, and its main goal is to design airfoil and wing shapes as well as turbomachinery components which exhibit this shock-free nature at design conditions [51].

The fundamental concept behind this method is that the governing equations for the fluid dynamic problem in consideration are modified locally. The flow is solved with an altered perfect gas-dynamic law within the supersonic region of the flow. This results in a preliminary elliptic behaviour within this supersonic domain, consequently leading to a so-called fictitious part of the flow [52]; hence the name of this method.

For both inverse surface and inverse field methods, a shared main disadvantage is that the objective of a target pressure distribution is built directly into the design process and thus cannot be changed to any arbitrary objective function.

2.6.3. Numerical Optimization Method

The final common aerodynamic shape optimization is the numerical optimization method. A gradient based optimization method is most common within this category.

It is common to first parametrize the geometry that is to be altered, in order to allow for the evaluation of a high number of different geometries against a relatively low computational cost. There exists numerous parametrization techniques, but they can more or less be generalized through the following method: the geometry which is to be modified is parametrized and defined by weights, a_i, combined with a certain shape functions b_i. The geometry can then be represented by:

$$f(x) = \sum_{i=1}^{n} a_i b_i(x) \tag{2.26}$$

Subsequently, a cost function I or objective function is defined which contains the parameter that is to be maximized or minimized. The function in itself should be a function of the weights a_i. It can then be related to the gradient $\partial I / \partial a_i$ through:

$$\delta I = \sum_{i=1}^{n} \frac{\partial I}{\partial a_i} \delta a_i \tag{2.27}$$

The gradient of the function is used to determine a direction within the feasible design space for improvement, which can be a reduction in drag for instance. The figure of merit is typically described by a function termed as the objective function.

2.7. Discussion and Conclusion

A study regarding the aerodynamic considerations of the Hyperloop was performed, where literature on Hyperloop relatable systems is assessed, as well as literature on (shape) optimization methods and CFD simulations. The Hyperloop is a newly proposed transportation mode that can give answers to the rising demand of high-speed, sustainable travel. A sustained global economy growth requires faster, cheaper, safer and more efficient transportation modes. In a Hyperloop system, pods are propelled through a reduced pressure tube while being magnetically levitated. The airliner speeds at which the pods travel combined with its means of propulsion result in a significant time and energy reduction compared to conventional transport systems for similar medium distances (up to approximately $2000km$). The Hyperloop can provide a direct, on-demand, low-emission and energy efficient means of transportation.

A careful design is necessary in order to achieve the (performance) benefits and in particular the aerodynamic design. A Hyperloop pod travels in an unconventional flow regime: very low Reynolds numbers (order 10^5) with high Mach numbers (Mach 2.5 locally). This brings with it its own unique challenges that have to be dealt with. The (aerodynamic) design of the Hyperloop is comparable to a

typical aerospace problem, that tackles the same strategic goals of having low-carbon propulsion and highly efficient vehicles.

Literature has shown that there already has been research conducted on the aerodynamics, but still on a conceptual and preliminary level. The main aerodynamic challenge will be coping with the Kantrowitz limit which is associated to choked flow. Violating this limit could lead to a three-fold increase in drag coefficient compared to operations in non-choked conditions. The most important parameters concerning the aerodynamic design are the blockage ratio, vehicle speed and operating tube pressure. For the blockage ratio, a feasible range lies within 0.25 - 0.7.

Furthermore, the speed regime in which the pods is operative means that shockwaves will be present, which is detrimental to the aerodynamic performance of the pod. Again, a careful and adequate design needs to be developed in order to cope with these aerodynamic phenomena in order to achieve the aforementioned benefits of this transportation system.

While the operating pressure within the tube is at a mere $100Pa$, the shape of the vehicle still significantly affects the overall aerodynamic performance. Investigations on basic shapes have shown that a vehicle with an elliptical head and semicircular tail yield the lowest pressure difference between the front and back of the vehicle for low blockage ratios. However, different combinations of head and tail shapes were found to be more efficient at higher blockage ratios. Once again, the importance of this parameter is noted.

A suitable range for the ratio of nose length to pod diameter should lie within 1.5 - 2.5. A longer nose and tail is beneficial for the aerodynamic drag reduction, but the effects are less pronounced with increasing length. The relative thick boundary layer due to the low Reynolds number means that separation can occur at relative ease, and a design that promotes turbulent flow is therefore a possible design strategy.

For the prediction of general aerodynamic quantities through a simplified aerodynamic flow model, the channel flow approach or panel method are considered to be suitable methods. Through the fact that the pod and tube walls form a channel, the typical nozzle flow calculation scheme can be followed in order to compute the flow field around the pod if the channel approach is taken.

Within the CFD analyses that were conducted to obtain the above mentioned aerodynamic findings, it was observed that RANS-based simulations with a $k - \epsilon$ turbulence model is the most widely used model for the aerodynamic analysis of these tube trains. The main reason for this model to be chosen over others is mainly due to the fact that it performs well for wall-bounded flows in particular, thus similar to flow within a tube as is the case for the Hyperloop pod.

These findings from literature regarding aerodynamic design considerations of the Hyperloop pod serve as a good starting point for the development of an aerodynamic design and optimization procedure. This literature study serves as a foundation of the research project.

3

Aerodynamic Shape Optimization Methodology

In this research project, an aerodynamic solver is developed which is capable of aerodynamically analyzing a Hyperloop pod and determine the drag of the pod. In this case, CFD analyses are performed in order to validate the solver method. Furthermore, the solver is utilized to perform a shape optimization, in which the aim is to reduce the aerodynamic drag of the pod.

This chapter will cover the procedure that was taken in order to arrive at the aerodynamic model that is capable of analyzing the flow behaviour around the Hyperloop pod. The main goal of this model is to predict the aerodynamic drag of the pod. Afterwards, the model is coupled to a gradient-based optimization scheme, in which a shape is sought for that has the lowest aerodynamic drag. In Section 3.1, the main assumptions made and their implications on the governing fluid dynamic equations are discussed. Section 3.2 will cover the main procedure that was developed in order to derive main flow parameters (e.g. p, T) with which the aerodynamic drag can be determined. Thereafter, in Section 3.3, the baseline pod will be presented which is based off requirements as set by HARDT combined with main findings from literature. This baseline pod will act as a reference in determining potential aerodynamic performance improvements. Finally, Section 3.4 will be covering the parametrization method of the geometry which is required in order to allow for the solver to analyze a large number of geometries in a short amount of time.

3.1. Main Assumptions and Governing Equations

In order to arrive at a simplified aerodynamic model, assumptions and simplifications are made in order to reduce the complexity of the model, thereby reducing computational efforts. It is evident however, that the physical problem still needs to be correctly represented, which means that care must be taken in making these simplifications. Validation of the model with CFD is therefore important, in order to assess the ability of the model to simulate the physical problem and to investigate which of the neglected effects are causes for any possible but acceptable discrepancies.

First of all, the flow around the pod is modeled as a flow through a channel with a varying area, where the pod surface and tube wall pose as channel walls. As such, the flow domain can be regarded as a compressible (convergent-divergent) nozzle, assuming that there will be a minimum section somewhere over the pod surface, equivalent to the location of the throat. It is furthermore assumed that the variation in area is gradual, which means that the flow is modeled as a quasi-1D flow. This type of flow is one in which all relevant flow parameters vary primarily in one direction, which is the flow direction x in this case. The most important implications that come with this assumption are listed below:

- Flow parameters uniform along each section: $A = A(x)$, $p = p(x)$ etc.

- $V_x \neq 0$

- $\frac{V_y}{V_x} \ll 0$

- $\frac{V_z}{V_x} \ll 0$

The flow is furthermore assumed to be isentropic. For accelerating flows (favorable pressure gradients), the idealization of isentropic flow is generally a realistic model of the actual flow behavior [23]. This supports the isentropic flow assumption, as the flow around the pod is in an accelerating state for the largest part in the region of interest. The isentropic flow assumption mainly implies that certain quantities, the total temperature for instance, are assumed to be constant throughout the flow domain.

Finally, the flow is assumed to be steady and inviscid, with the air assumed to behave as an ideal gas. The main implications of this assumption is that the heat capacity ratio γ is equal to 1.4 for air and that the ideal gas law is valid for calculations.

The quasi-1D flow assumption evidently has its implications on the governing fluid dynamic equations. How these equations relate specifically to the flow field under consideration will be briefly discussed in the following subsections.

3.1.1. Conservation of Mass

The first discussed governing equation is based on the physical principle that mass can neither be created nor destroyed. The mass conservation in its integral form is given by [53]:

$$\frac{\partial}{\partial t} \iiint_V \rho d\mathcal{V} + \oiint_S (\rho \vec{V} \cdot dS) = 0 \tag{3.1}$$

This equation is also known as the continuity equation, which for a steady flow ($\frac{\partial}{\partial t} = 0$) reduces to:

$$\oiint_S \rho \vec{V} \cdot dS = 0 \tag{3.2}$$

When looking at a specific section of the flow passage within the nozzle and regarding it as a control volume that spans across station 1 to station 2, the application of the mass conservation equation 3.2 to this specific section in the main flow direction, the following is noted: as for each specific cross-sectional area, A, the density and velocity are assumed to be constant, these can be taken out of the integral. This then leads to a simplified balance equation:

$$-\rho_1 u_1 \iint_1 dA + \rho_2 u_2 \iint_2 dA = 0 \tag{3.3}$$

and finally further simplifies to:

$$\rho_1 u_1 A_1 = \rho_2 u_2 A_2 \tag{3.4}$$

The analysis for this specific section can essentially be applied to any section along the flow passage, which means that a more general equation can be formulated for the mass flow where the flow parameters are thus only a function of x due to the quasi-1D assumption. This mass flow rate is to stay constant:

$$\dot{m} = \rho(x)u(x)A(x) = C \tag{3.5}$$

3.1.2. Conservation of Momentum

The momentum equation relies on the physical principle that a force is equal to the time rate of change of momentum. The conservation of momentum equation for an inviscid flow, without body forces, is given in its integral form by:

$$\frac{\partial}{\partial t} \iiint_V \rho \vec{V} d\mathcal{V} + \oiint_S (\rho \vec{V} \cdot dS)\vec{V} = -\oiint_S p \cdot dS \tag{3.6}$$

which again for a steady flow reduces to

$$\oiint_S (\rho \vec{V} \cdot dS)\vec{V} = -\oiint_S p \cdot dS \tag{3.7}$$

As for the same implications with the conservation of mass, the density and velocity are constant for a specific cross-sectional area and can thus be taken out of the integral. Together with this assumption and again looking at a specific location within the passage leads to the following relation:

$$p_1 A_1 + \rho_1 u_1^2 A_1 + \int_{A_1}^{A_2} p\, dA = p_2 A_2 + \rho_2 u_2^2 A_2 \tag{3.8}$$

This equation can be rewritten in its differential form:

$$pA + \rho u^2 A + p\, dA = (p + dp)(A + dA) + (\rho + d\rho)(u + du)^2 (A + dA) \tag{3.9}$$

which after rearrangement leads to:

$$A\, dp + Au^2\, d\rho + \rho u^2\, dA + 2\rho u A\, du = 0 \tag{3.10}$$

Finally, from the findings of the conservation of mass, it was noted that the mass flow is given by the product of the density, area and flow velocity and is furthermore to remain constant. Hence, the derivative of this product is equal to zero. This implies that the second and third terms in equation 3.10 can be omitted. This then results in the so-called Euler's equation:

$$dp + \rho u\, du = 0 \tag{3.11}$$

3.1.3. Conservation of Energy

The final fundamental equation that is covered is the energy equation. Since the density is not constant for a compressible flow, this additional relation is required to complete the system. The energy equation is based on the physical principle that energy can neither be created nor destroyed. It can only change in form. Again, for an inviscid, steady and adiabatic flow without body forces, the energy equation is given by:

$$\oiint_S \rho \left(e + \frac{V^2}{2} \right) \vec{V} \cdot \, dS = - \oiint_S p \vec{V} \cdot \, dS \tag{3.12}$$

Applying the above equation again to the aforementioned control volume within the flow passage yields:

$$\rho_1 \left(e_1 + \frac{u_1^2}{2} \right)(-u_1 A_1) + \rho_2 \left(e_2 + \frac{u_2^2}{2} \right)(u_2 A_2) = p_1 u_1 A_1 - p_2 u_2 A_2 \tag{3.13}$$

which after rearrangement leads to the following balance equation:

$$p_1 u_1 A_1 + \rho_1 u_1 A_1 \left(e_1 + \frac{u_1^2}{2} \right) = p_2 u_2 A_2 + \rho_2 u_2 A_2 \left(e_2 + \frac{u_2^2}{2} \right) \tag{3.14}$$

Dividing this equation by the mass balance relation (equation 3.4) yields:

$$\frac{p_1}{\rho_1} + e_1 + \frac{u_1^2}{2} = \frac{p_2}{\rho_2} + e_2 + \frac{u_2^2}{2} \tag{3.15}$$

Finally, noting that the quantity $p/\rho + e$ is equal to the enthalpy h, the energy equation can be expressed as:

$$h_1 + \frac{u_1^2}{2} = h_2 + \frac{u_2^2}{2} \tag{3.16}$$

An important implication of the energy equation is therefore that the quantity $h + u^2/2$, which is equal to the total enthalpy h_t, remains constant throughout the flow.

3.2. Computation of Aerodynamic Quantities

As the flow is modeled as a quasi-1D nozzle flow, the computation of relevant aerodynamic quantities and distributions is to a large extent based on the ratio of the local area between the pod surface and tube wall, and the area of the throat. This will become evident with the implications of the simplifications that were discussed in the previous section. It is important to note that the pod is axisymmetric with a circular cross-section. As such, circular areas are taken when computing area ratios and only one half of the flow path is modeled to save computational time.

3.2.1. Mach Number Distribution

To predict the flow velocity around the pod, an expression is derived which relates the ratio of local area and throat area to the local Mach number. In order to arrive at this expression, the continuity equation that was earlier derived (equation 3.4) is applied to the throat section, where the flow reaches sonic conditions. The throat section is denoted by the superscript $*$:

$$\rho^* u^* A^* = \rho u A \tag{3.17}$$

subsequently, the ratio between the local and throat areas can be expressed as:

$$\frac{A}{A^*} = \frac{\rho^* u^*}{\rho u} = \frac{\rho^* a^*}{\rho u} = \frac{\rho^*}{\rho_T} \frac{\rho_T}{\rho} \frac{a^*}{u} \tag{3.18}$$

Due to the isentropic flow assumption, the stagnation density can be expressed as a fraction of its static value in terms of the Mach number alone as a variable:

$$\frac{\rho_T}{\rho} = (1 + \frac{\gamma - 1}{2} M^2)^{\frac{1}{\gamma - 1}} \tag{3.19}$$

at sonic conditions, this relation becomes:

$$\frac{\rho^*}{\rho_T} = (\frac{2}{\gamma + 1})^{\frac{-1}{\gamma - 1}} \tag{3.20}$$

With expressions for the first and second term on the right hand side of equation 3.18 and noting that last term in this equation is the inverse of the Mach number, a relation can be obtained which relates the Mach number to the ratio of local area to throat area:

$$\left(\frac{A}{A^*}\right)^2 = \frac{1}{M^2} \left[\frac{2}{\gamma + 1} (1 + \frac{\gamma - 1}{2} M^2) \right]^{\frac{\gamma + 1}{\gamma - 1}} \tag{3.21}$$

The Mach number distribution around the pod can then be based on the local area between the tube and pod for a given throat area. At any given area ratio, the resulting Mach number can either be sub- or supersonic due to the quadratic nature of the equation.

Since the inflow is subsonic, the flow cannot become supersonic up to the throat, where it then reaches sonic conditions. The flow behaviour after the throat however, depends on the boundary condition which is the pressure ratio across the nozzle, or in this case, the pressure ratio between the front and back of the pod.

The pressure build-up in front of the pod, due to violation of the Kantrowitz limit, always 'guarantees' a sufficiently high pressure ratio (>1.893) [54] to sustain a supersonic flow throughout the diverging passage. This implies that after the throat, the flow will always expand to local supersonic speeds. From this qualitative analysis, a general flow profile can already be predicted: the flow is subsonic up to the throat where it then expands and accelerates to supersonic velocities.

3.2.2. Pressure Distribution

Not only is the Kantrowitz limit responsible for a supersonic outlet, from literature, it became clear that this limit which is associated to the choking of the flow is the largest contributor to the aerodynamic drag of the pod. This then also has its implications on the determination of the pressure distribution over the pod, and thus also the computation of the pressure drag. By determining the pressure drag based off a pressure distribution that follows directly from the velocity distribution, the build-up of

the pressure in front of the pod due to choking is not taken into account. Since the flow is choked, this 'traditional' approach does not suffice in predicting the pressure distribution over the pod, as it naturally yields an under-predicted pressure drag. Therefore, the pressure is to be determined from the 'required' mass flow rate.

First of all, realizing that sonic conditions are reached at the throat location, the local velocity is thus equal to the local speed of sound:

$$u^* = a = \sqrt{\gamma R T^*} \tag{3.22}$$

This expression can be used to find an expression for the mass flow rate at the throat. Combining this equation with the earlier found relations for the continuity and total density, given by equations 3.17 and 3.20 respectively, the mass flow at the throat can be expressed as follows:

$$\dot{m} = \rho_T \left[\frac{\gamma + 1}{2} \right]^{\frac{-1}{\gamma - 1}} \sqrt{\gamma R T^*} A^* \tag{3.23}$$

Again, since the flow is assumed to be isentropic with air as an ideal gas, the total conditions of the density is given by:

$$\rho_t = \frac{p_t}{R T_t} \tag{3.24}$$

while the static temperature can be related to the total temperature by:

$$\frac{T_t}{T} = 1 + \frac{\gamma - 1}{2} M^2 \tag{3.25}$$

For the conditions at the throat, the static temperature can be expressed in terms of the stagnation temperature according to:

$$\frac{T^*}{T_t} = \left[1 + \frac{\gamma - 1}{2} \right]^{-1} \tag{3.26}$$

Combining equations 3.24 and 3.26 with equation 3.23 yields an expression for the choked mass flow rate:

$$\dot{m}_{choked} = \frac{p_t}{R T_t} \left[\frac{\gamma + 1}{2} \right]^{\frac{-1}{\gamma - 1}} \sqrt{\gamma R \frac{T^*}{T_t} T_t A^*}$$

which after rearrangement yields:

$$\dot{m}_{choked} = \frac{p_t A^*}{\sqrt{T_t}} \sqrt{\frac{\gamma}{R} \left(\frac{2}{\gamma + 1} \right)^{(\gamma+1)/(\gamma-1)}} \tag{3.27}$$

The choked mass flow rate is therefore only dependent on the stagnation properties and the area of the throat, while in the general case, the mass flow rate is given by:

$$\dot{m} = \frac{p_t A}{\sqrt{T_t}} \sqrt{\frac{\gamma}{R}} M \left(1 + \frac{\gamma - 1}{2} M^2 \right)^{-\frac{\gamma+1}{2(\gamma-1)}} \tag{3.28}$$

With the known inflow conditions, the choked mass flow through the tube can be determined. In this case, the static temperature is $288.15 K$, while the velocity is $300 m/s$. With the Mach number distribution and stagnation conditions known, the static temperature can also be computed at every location with the earlier mentioned isentropic equation 3.25. This relies on the assumption that the total temperature remains constant over the domain.

In agreement with the continuity equation, it is evident that the amount of air that bypasses the pod is to be conserved, which follows from the conservation of mass principle. The mass flow rate is therefore to stay constant throughout the flow passage. As discussed in Section 3.1.1, the mass flow equation simplifies to the product of the density, velocity and local area between the tube and pod.

With the local temperature known, the local speed of sound can be obtained and thus also the local velocity with the known local Mach number. The density that follows from the sustained mass flow rate can then be determined by:

$$\rho(x) = \frac{\dot{m}_{required}}{A(x)V(x)} \tag{3.29}$$

with the known (distribution of) static quantities, the static pressure can be determined according to the ideal gas law:

$$p(x) = \rho(x)RT(x) \tag{3.30}$$

Finally, the pressure can be integrated over the surface in order to obtain the total pressure drag. The pressure acts normal onto the pod surface, so it must be noted that only the component that contributes to the pressure drag is to be taken into account, i.e. the component projected along the direction of travel:

$$D_{pressure} = \iint_S p(x)cos(\theta)dA \tag{3.31}$$

In this equation, θ is the angle between the surface normal and the pressure drag direction.

3.2.3. Viscous Effects

The development of the boundary layer is an important aspect for the determination of the viscous drag and heat transfer for instance. However, for this internal aerodynamic problem, it more importantly affects the aerodynamic characteristics through its influence on the effective height of the pod. Since the length of the pod is a few orders of magnitudes higher compared to the height between the pod and the tube, the thickness development of the boundary layer can play a significant role on the velocity distribution. This effect is more pronounced for the specific flow conditions of the pod, where low Reynolds number contribute to a faster growth in boundary layer height.

The boundary layer characteristics are highly dependent on the Reynolds number of the flow, which thus has to be determined first. The dynamic viscosity μ which is needed to compute the Reynolds number is determined according to Sutherland's law [55]:

$$\mu = \mu_0 \frac{T_0 + C}{T + C} \left(\frac{T}{T_0}\right)^{3/2} \tag{3.32}$$

For this case, the boundary layer is modeled to behave according to a Blasius boundary layer, which assumes that the pressure remains constant throughout the height of the boundary layer [56]. Furthermore assuming that the development of the boundary layer can be modeled as that over a flat plate, the thickness δ for a laminar flow is then given by the Blasius solution:

$$\delta_{laminar} = \frac{5.0x}{\sqrt{Re_x}} \tag{3.33}$$

The flow regime is considered as a transitional one, implying that at a certain point downstream of the nose, the laminar boundary layer transitions into a turbulent one which grows at a faster rate. Thus, a so-called transition point exists somewhere over the pod surface. The inclusion and determination of the transition point is not only important for the correct prediction of the friction drag, but more importantly for the determination of the effective pod height.

The value of the length x at which this transition happens is typically termed as the critical length x_{crit}. This critical distance then allows for an associated critical Reynolds number Re_{crit} which, when continuing with the flat plate assumption, is approximately $5 \cdot 10^5$ [57]. As such, the transition point can be determined:

$$x_{crit} = \frac{\mu_\infty Re_{crit}}{\rho_\infty V_\infty} \tag{3.34}$$

After this transition point, the boundary layer then grows according to:

$$\delta_{turbulent} = \frac{0.37x}{Re_x^{1/5}}$$ (3.35)

The boundary layer thickness is typically defined as the distance between the wall to a certain point where the flow velocity has reached 99% of the outer flow velocity. While the concept of a boundary layer thickness is often used to qualitatively analyze flow behaviour, a more 'fluid mechanically correct' measure to characterize the boundary layer is the displacement thickness δ^*, defined as:

$$U\delta^* = \int_{y=0}^{\infty} (U-u)dy$$ (3.36)

U is the velocity on the outer edge of the boundary layer at a certain position x. Since the flow near the wall is retarded, the streamlines are displaced outwards in order to satisfy continuity. This displacement is thus described by δ^*, and is in effect a measure to account for the missing mass flow due to the boundary layer [58]. Again, for a flat plate, this thickness is given by:

$$\delta_{laminar}^* = \frac{1.72x}{\sqrt{Re_x}}$$ (3.37)

Subsequently, the displacement thickness for a turbulent boundary layer is given by:

$$\delta_{turbulent}^* = \frac{0.020x}{Re_x^{1/7}}$$ (3.38)

This displacement thickness is added to the height of the pod, which then results in a so-called effective height. The inviscid flow outside the boundary layer therefore 'sees' a different body than the original geometry. This effective dimension is then used to determine local area ratios for the calculation of the Mach number distribution. A visualization of this effective height is shown in Figure 3.1. The boundary layer thickness visualized by the dashed line is highly exaggerated for clarity purposes and does not represent the actual thickness development.
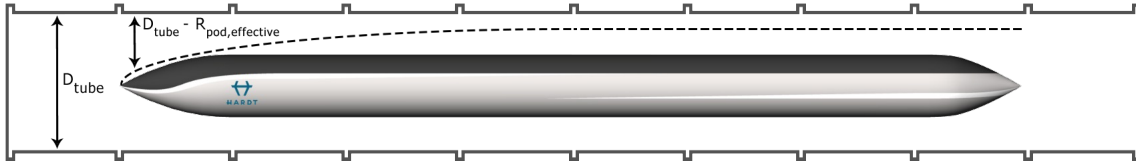

Figure 3.1: Boundary layer growth over the Hyperloop pod

The gradual increase in boundary layer thickness implies that the Mach number is always increasing over the flat surface of the pod, as the effective area between the tube and pod is decreasing with downstream location. The location of the throat will therefore always be around the end of the constant radius section, as the local area will increase again due to the geometry of the tail (i.e. where the pod radius decreases again). The flow will therefore reach sonic conditions close to the tail section, where it then expands afterwards.

Besides the influence on the velocity distribution and thereby on the pressure drag, the viscous effects of course also causes the generation of skin friction drag. However, the skin friction drag is deemed to have a minimal impact on the design and thus optimization of the pod, since it generally accounts for 5-10% of the total drag as was concluded from literature investigations. It is therefore opted to use semi-empirical equations for the skin friction coefficient, instead of obtaining a skin shear stress distribution to predict the skin friction drag. A more accurate skin friction drag would be predicted if the shear stress distribution was determined, but the added complexity and hence longer optimization process does not weigh up against the relative small increase in accuracy for prediction of the friction drag. The Blasius solution yields a friction coefficient relation for a laminar flow as given by [59]:

$$C_{f,laminar} = \frac{0.664}{\sqrt{Re_x}}$$ (3.39)

As is known, the skin friction drag for a turbulent flow is higher, resulting in a higher skin friction coefficient. For the turbulent flow, Prandtl's one-seventh-power law is used [8]:

$$C_{f,turbulent} = \frac{0.027}{Re_x^{1/7}} \tag{3.40}$$

Finally, the skin friction drag can be determined by integrating the coefficient over the surface of the pod:

$$D_{friction} = \iint_{A,laminar} C_{f,laminar} \frac{\rho V^2}{2} dA + \iint_{A,turbulent} C_{f,turbulent} \frac{\rho V^2}{2} dA \tag{3.41}$$

3.3. Baseline Hyperloop Pod

A baseline geometry is defined first in order to have a reference and a basis for the optimization procedure. This baseline design is based off main findings from literature, since no prior model was defined yet.

From literature, it became clear that a combination of an elliptical nose combined with a similar but more blunt tail yields the lowest amount of pressure drag. Furthermore, an advised range for the length of the nose and tail were given that should lie between 1.5 - 2 times the diameter of the vehicle. A geometry based on these findings is therefore taken as baseline design, in order to provide an initial point that can possibly accelerate the optimization procedure.

As per top level requirements (set by HARDT), the geometry of the pod is only fixed in terms of its length and radius of the constant section, which are to be $39m$ and $1.7m$ respectively.

In terms of operational requirements, the internal tube pressure is set at a pressure of $100Pa$, which is then regarded as the free-stream pressure. The geometrical and flow parameters are given in Table 3.1.

Table 3.1: Geometrical and flow parameters of the Hyperloop

Geometrical parameters	Description	Value	Unit
$L_{constant}$	Constant section length	39	m
R_{pod}	Pod radius	1.7	m
R_{tube}	Tube radius	2.15	m
L_{nose}	Nose length	6	m
L_{tail}	Tail length	4	m
β	Blockage ratio	0.625	-
Flow parameters	**Description**	**Value**	**Unit**
p_{tube}	Internal tube air pressure	100	Pa
T_{tube}	Internal tube air temperature	288.15	K
ρ_{tube}	Internal tube air density	0.0012	kg/m^3
V_{pod}	Pod velocity	300	m/s
$\dot{m}_{required}$	Required mass flow rate	5.268	kg/s
Re	Reynolds number	$9.735 \cdot 10^5$	-
Re_{crit}	Reynolds number	$5 \cdot 10^5$	-
x_{crit}	Transition point	26.00	m

Combining the main findings of literature regarding an aerodynamic efficient shape with the top level requirements, a baseline model was formed which is shown in Figure 3.2. The nose and tail have lengths of $6m$ and $4m$ respectively.

Figure 3.2: Geometry of the baseline Hyperloop pod

3.4. Pod Shape Parametrization

To allow efficient geometrical sweeps in order to perform the aerodynamic analysis described in Section 3.2 on a large number of geometries, parametrization of the pod shape is required. Shape parametrization is the process of finding parametric equations in order to describe a certain geometry. Since this is a 2D optimization where only one half of the geometry has to be described, the geometry is essentially defined by a curve. Shape parametrization is necessary in order to translate the system into a mathematical representation suitable for (aerodynamic) analysis, which at the same time should allow for enough freedom in geometrical changes when coupled with an optimization scheme.

More importantly, the parametrization allows for a significantly reduced time in the overall optimization procedure, as the geometry is described by a smaller set of variables when compared to the original representation consisting of Cartesian coordinates.

The class-shape function transformation method (CST) proposed by Boeing [60] is used for the parametrization of the Hyperloop pod. As the name suggests, the parametrization is based on two functions: a class function $C(x)$ and a shape function $S(x)$. A general curve $\zeta(x)$ is then described by:

$$\zeta(x) = C_{N_2}^{N_1}(x) \cdot S(x) \tag{3.42}$$

The properties and purposes of these functions are briefly touched upon in the subsequent sections.

3.4.1. Class Function

The class function can be regarded as a template for a certain shape. It guarantees that characteristic geometrical features of the overall shape are preserved when the shape is altered for an optimization process. In an aerodynamic problem for instance, a streamlined shape is generally desired, which thus can be guaranteed by a specific class function. The mathematical definition of the class function is given by:

$$C_{N_2}^{N_1}(x) = x^{N_1} \cdot (1-x)^{N_2}, 0 \le x \le 1 \tag{3.43}$$

The coefficients N_1 and N_2 are responsible for the characteristic shape of the geometry. In Figure 3.3, examples are given as to how certain values for the coefficients of the class function affect the overall shape for a shape function of unity.
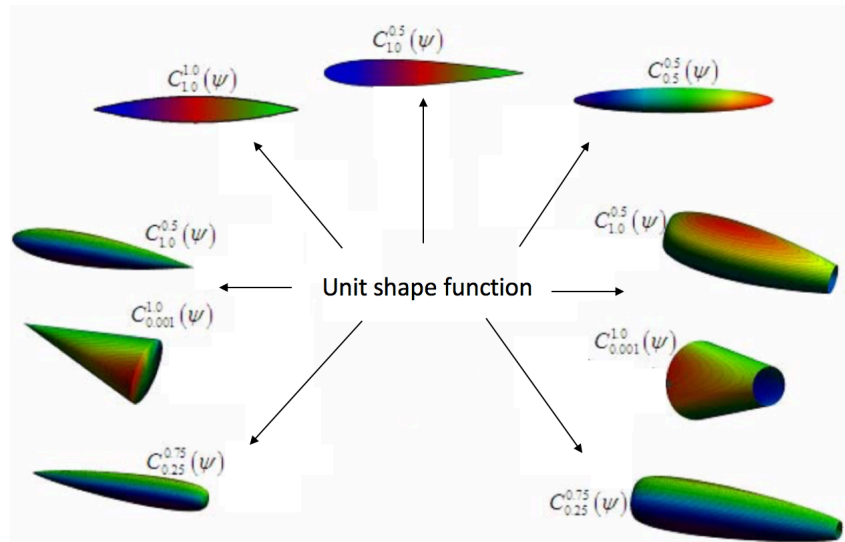
Figure 3.3: Geometries for different class functions based on a unit shape function

3.4.2. Shape Function

The shape function is in essence the sum of Bernstein polynomials multiplied by scaling factors in a vector of same length. The mathematical description of this function is given by:

$$S(x) = \sum_{i=1}^{n} (A)_i \cdot S_i(x) \tag{3.44}$$

In this equation, $(A)_i$ is the vector of scaling factors, while $S_i(x)$ are the Bernstein polynomials. These polynomials are formed through linear combinations of Bernstein basis polynomials and are restricted to the interval [0,1] [61]. The $n + 1$ number of basis polynomials are defined by:

$$S_{i,n}(x) = \binom{n}{i} x^i (1-x)^{(n-i)}; \; i = 0, ..., n \tag{3.45}$$

The coefficient n indicates the order of the polynomial. As an example, these polynomials up to the fourth order are given as defined by equations 3.46 to 3.50. A fourth order polynomial (n = 4) thus implies that five (n+1) basis polynomials are required.

$$b_{0,0} = 1 \tag{3.46}$$

$$b_{0,1}(x) = 1 - x, \quad b_{1,1}(x) = x \tag{3.47}$$

$$b_{0,2}(x) = (1-x)^2, \quad b_{1,2}(x) = 2x(1-x), \quad b_{2,2}(x) = x^2 \tag{3.48}$$

$$b_{0,3}(x) = (1-x)^3, \quad b_{1,3}(x) = 3x(1-x)^2, \quad b_{2,3} = 3x^2(1-x) \quad b_{3,3}(x) = x^3 \tag{3.49}$$

$$b_{0,4}(x) = (1-x)^4, \quad b_{1,4}(x) = 4x(1-x)^3, \quad b_{2,4} = 6x^2(1-x)^2$$

$$b_{3,4}(x) = 4x^3(1-x) \quad b_{4,4}(x) = x^4 \tag{3.50}$$

To have an illustrative example, both third and fourth order polynomials are shown in Figure 3.4. An important property that can be noted is that the sum of these polynomials is always equal to 1 over the defined domain of x as illustrated by the dashed line in the figures.

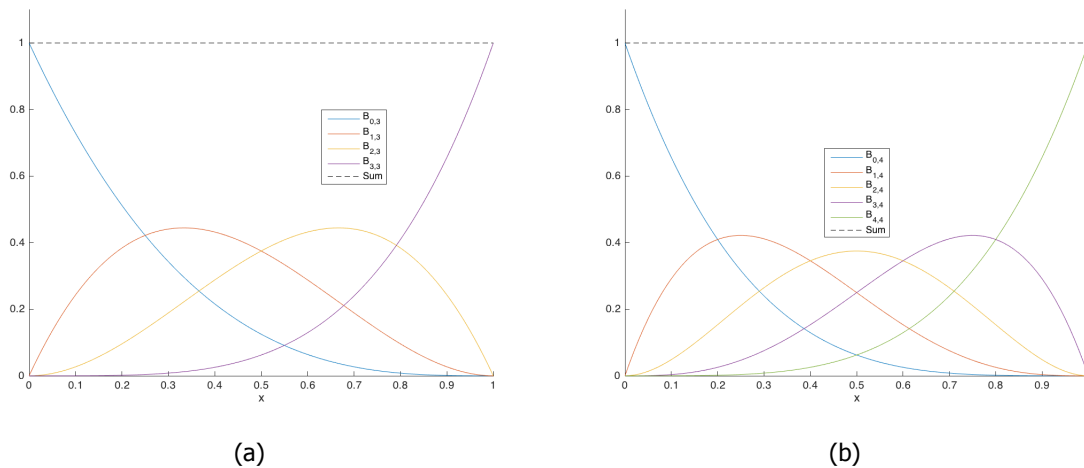(a)   (b)

Figure 3.4: Bernstein polynomials of third (a) and fourth (b) order

As mentioned, these Bernstein polynomials are then multiplied with the scaling factors to finally form the shape factor. As such, the shape of this dashed line formed by the sum can be manipulated. An example of the effect of this scaling is seen in Figure 3.5. In this case, the fourth curve has been scaled by 0.3, yielding a concavity at the aft section of the curve.
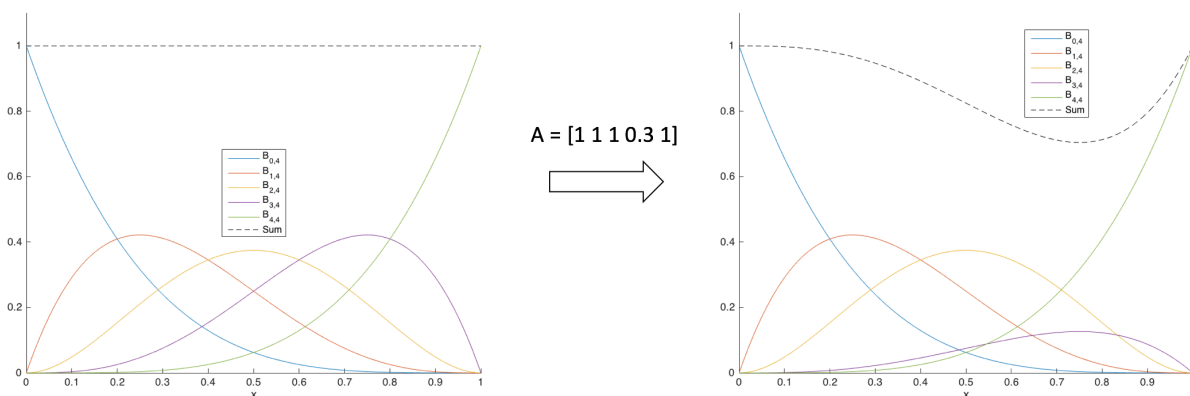

Figure 3.5: Effect of scaling on a unit shape function

Finally, when multiplying this with the earlier discussed class function, the shape of the original curve that was to be parametrized is obtained. Therefore, when altering the shapes in an optimization, the only parameters that need to be varied are the scaling factors of the shape function, also known as the CST coefficients. The length of the CST vector (i.e. amount of CST coefficients required) depends on the degree of the Bernstein polynomials.

3.4.3. Curve Fitting

It is now evident that when using the CST method as curve parametrization technique, the values that are to be sought for in order to represent a certain curve are the scaling factors A_i. The baseline configuration is given as Cartesian coordinates, and a specific set of scaling factors has to be found to represent this curve. In essence, this curve fitting is a small optimization problem in itself, where a set of scaling factors is sought for that yields the lowest difference in original coordinates and the ones obtained from parametrization. Thus, an error function can be defined which is to be minimized, in order to match the coordinates produced by the CST method to that of the original Cartesian coordinates:

$$\epsilon(\bar{x}) = \sum_{i=1}^{N}(y_{CST,i}(\bar{x}) - y_{cartesian,i})^2 \tag{3.51}$$

In the error function, N represents the total number of Cartesian coordinate points. Furthermore, the square of the error is taken in order to ensure convergence towards a positive error value.

3.4.4. Parametrization Values

The first step in parametrizing the nose and tail of the baseline model is to determine the number of CST coefficients that yields the most accurate representation of the original curve. In Section 3.4.2, it was noted that the sum of the basis polynomials is always equal to one. For a horizontal line, it therefore does not matter whether a first or fifth order polynomial is used as the same result is achieved. For a curve of arbitrary shape however, the order of the polynomial does in fact matter and different accuracies are obtained for different orders, where the accuracy is expressed by the error function as was defined by equation 3.51.

Generally, a higher order curve leads to more accurate curve parametrizations. However, it is evident that a higher order curve also results in a longer optimization process as more CST coefficients are to be modified. On the other hand, a certain minimum number of coefficients is required in order to ensure design flexibility and an accurate parametrization. A curve order comparison is therefore performed which shows the error trend for an increasing number of CST coefficients. This comparison is done for the geometry of the nose with CST coefficients varying from 1 to 20. The respective errors are shown in Figure 3.6a. For clarity, the errors from 6 CST coefficients onwards are also shown in Figure 3.6b.

(a)   (b)
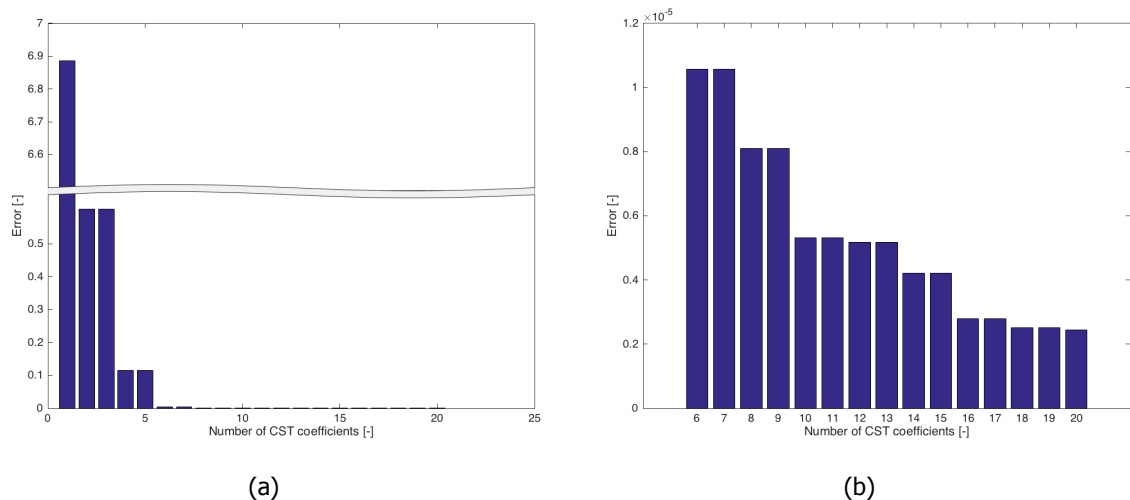
Figure 3.6: Errors for 1 to 20 CST coefficients

For relative low numbers of CST coefficients, it can be noted that the error decreases rapidly when the number of coefficients is increased. After 5 CST coefficients, the error already drops several orders of magnitudes, in the range of 10^{-5}. From 10 coefficients onwards, the reduction in error is negligibly and relatively small. A further increase in number of coefficients yields a relative large increase in computational time compared to the minimal error reduction. Therefore, it is decided to use 10 CST coefficients for the parametrization of the nose and tail geometries, where the difference between the CST coordinates and original Cartesian coordinates is in the range of $0.58 \cdot 10^{-5}$. The values of the initial CST coefficients to create the baseline geometry are listed in Table 3.2.

Table 3.2: Values of CST coefficients for the baseline design

$\mathbf{CST}_{nose}$	Value	$\mathbf{CST}_{tail}$	Value
1	-0.131	11	0.9999
2	0.3518	12	0.9999
3	0.4096	13	0.9999
4	0.6768	14	0.9997
5	0.8394	15	0.9987
6	0.8046	16	0.9124
7	0.9911	17	0.7802
8	0.9993	18	0.9561
9	0.9998	19	0.4332
10	0.9999	20	0.4893

4

Aerodynamic Model Validation

In the scope of this research project, CFD simulations are performed in order to validate the low-fidelity aerodynamic solver. Since no experimental data is available regarding aerodynamic aspects of the Hyperloop, CFD analyses are a relative reliable and efficient way in gaining confidence in the solver results in the scope of this project. One could of course also argue about the validity of the CFD results, which ideally are to be validated as well. Since this is not possible, the verification process of the CFD results are an integral part and need to be carefully addressed. For this research project, ANSYS Fluent is used to perform the CFD simulations, which is based on a finite volume method.

This Chapter will start off with a discussion on the numerical model that is employed for the simulations. In Section 4.2, the meshing of the geometry and computational domain properties are presented. Thereafter, in Section 4.3, the setup of the overall simulation model is touched upon. Section 4.4 will present the results of the simulation, where at the same time comparisons are made with the results obtained from the aerodynamic solver. Finally, a verification process is presented for the CFD procedure and is discussed in Section 4.5, with a general discussion and conclusion of the given in Section 4.6.

4.1. Numerical Model

Numerical methods are based on a discrete representation of solution and operators. This usually requires the projection of the continuous functions onto a discrete mesh of cells. Fluent is based on a finite volume method, which represents the solution as cell averages. Compared to the finite element and finite difference method (two other commonly used methods), the finite volume method is relatively robust and fast. In Fluent, the general scalar transport equation is converted into an algebraic one that is solved numerically.

In a finite volume method, the computational domain is divided into control-volumes that are non-overlapping: the finite volumes. These finite volumes are treated as a control volume on which the conservation laws are then evaluated for each volume individually [62]. The solution then consists of the cell average, and are associated with the cell centers. However, the solution does represent that of the entire cell.

Volume integrals containing a divergence term are transformed into surface integrals by means of Gauss's theorem, while the surface integrals are approximated by numerical quadrature rules. The fluxes Ψ which are a function of a certain conserved quantity ϕ over the finite volume determine the time evolution of the cell average as:

$$\frac{\partial}{\partial t}\phi = -\nabla \cdot \Psi \tag{4.1}$$

These conservation laws are then integrated over the finite volume as given by equation 4.2.

$$\frac{\partial}{\partial t}\int_{\bar{V}}\phi dV = -\int_{\bar{V}}\nabla \cdot \Psi dV \tag{4.2}$$

As mentioned, the volume integral is then rewrote to a surface integral. For a square control volume, this then leads to:

$$\int_{\bar{V}} \nabla \Psi \cdot d\mathcal{V} = \int_{S_V} n \cdot \Psi dS = \int_{S_{right}} n \cdot \Psi dS - \int_{S_{left}} n \cdot \Psi dS + \int_{S_{up}} n \cdot \Psi dS - \int_{S_{down}} n \cdot \Psi dS \qquad (4.3)$$

Since the flux that enters a certain volume is equal to the flux that leaves the volume, this method is termed as a conservative method. Together with the appropriate boundary conditions, an algebraic system of equations is obtained, which is then solved numerically in order to arrive at the solution.

4.1.1. Numerical Solver

For the numerical solver, a pressure-based solver is chosen as opposed to the density-based solver. Initially, the pressure-based solver was meant to be used for incompressible flows, while the density-based solver was meant for compressible flows. However, in later Fluent versions, both methods have been redefined in such way that their suitable operating conditions have been extended to a wide range of flow conditions [63].

Both methods utilize the moment equations to obtain the velocity field. The density-based solver is desired when complex flow interactions occur such as compressible flow with combustion for instance. Since there are no apparent complex flow structures present or expected in the flow field around the pod, the pressure-based solver is used as it requires less memory and is more flexible in the solution procedure, thereby accelerating convergence.

The pressure-based solver obtains the pressure by solving an equation for the absolute pressure or a pressure correction term, which in turn is obtained by the manipulation of the conservation equations. The solver employs an algorithm which belongs to the projection method. This method aims at deriving the pressure equation from the continuity and momentum equations while ensuring that the continuity is satisfied through pressure corrections.

Within the pressure-based approach, a segregated solver is opted for, which in this case is the Semi-Implicit Method for Pressure-Linked Equations (SIMPLE) algorithm [64]. A segregated solver sequentially solves for the pressure correction and momentum as opposed to a coupled solver, which does that simultaneously. The SIMPLE algorithm determines the pressure field by utilizing a relationship between the velocity and pressure corrections, whereby it enforces the mass conservation law. This algorithm is known for its robustness for general transitional and turbulent flow, which is why it is chosen.

4.1.2. Spatial Discretization

For the spatial discretization, a second-order accuracy is desired. A second-order upwind (SOU) scheme is therefore used for the spatial discretization. The SOU scheme offers a higher accuracy when compared to a first-order upwind scheme since an additional data point is introduced for the approximation of the spatial derivative. In Fluent, this is achieved at cell faces through a Taylor series of the solution about the cell centroid [65]. This is done for the pressure, momentum, turbulent kinetic energy and turbulent dissipation rate. The face value ϕ_f is then determined by:

$$\phi_{f,SOU} = \phi + \nabla \phi \cdot \vec{r} \qquad (4.4)$$

It is evident that $\nabla \phi$, which is the gradient of the upstream cell, needs to be determined in order to obtain the face value ϕ_f. To compute this gradient, the least squares cell-based gradient evaluation is used.

The least-squares cell-based method assumes that the solution varies linearly. This method is superior in terms of accuracy compared to a Green-Gauss cell-based gradient method and is comparable to a node-based gradient method, which are the two alternatives for the determination of the gradient within Fluent. While the latter is even more accurate, it is also computationally more expensive. Since there are no complex geometrical features present in this problem, it is expected that the mesh will have a relative simple topology, which is why the least-squares method is deemed to be suitable for this case. For a relatively simple mesh, a least-squares method is sufficient [66]. The change in cell values between a certain reference cell c_0 and an arbitrary neighbouring cell c_1 along a certain vector Δr_i is then given by:

$$(\nabla\phi)c_0 \cdot \Delta r_i = (\phi_{c_i} - \phi_{c0}) \tag{4.5}$$

For each neighbouring cell that surrounds the reference cell, a system of equations can then be defined [67]:

$$[M](\nabla\phi)c_0 = \Delta\phi \tag{4.6}$$

In this equation, M is the coefficient matrix that is only dependent on the geometry. Furthermore, $(\nabla\phi)c_0$ is the cell gradient (given by $\phi_x\hat{i} + \phi_y\hat{j} + \phi_z\hat{k}$) whereas $\Delta\phi$ is the difference vector ($\phi_{c1} - \phi_{c0}$). This (over-determined) linear-system of equations is then solved by the Gram-Schmidt process, which yields a matrix of weights for each cell [68]. There are therefore three components for each of these weights (one for each spatial direction for a 3D problem). The gradient at the cell center can then be computed by multiplying the weight factors by the difference vector [69]:

$$(\phi_x)_{c0} = \sum_{i=1}^{n} W^x i0 \cdot (\phi_{ci} - \phi_{c0}) \tag{4.7}$$

$$(\phi_y)_{c0} = \sum_{i=1}^{n} W^y i0 \cdot (\phi_{ci} - \phi_{c0}) \tag{4.8}$$

$$(\phi_z)_{c0} = \sum_{i=1}^{n} W^z i0 \cdot (\phi_{ci} - \phi_{c0}) \tag{4.9}$$

4.2. Mesh and Geometry Generation

The generation of the grid is an important aspect regarding the accuracy of the CFD simulation. The finite volumes as discussed in Section 4.1 are in essence the cells that are generated. An erroneously generated grid can lead to discretization errors and thus can affect the accuracy of a simulation. Discretezation errors can generally be lowered with a finer mesh, against the cost of a higher computational time. A trade-off therefore has to be made while meeting a certain accuracy threshold. The discretezation error will be further touched upon in Section 4.5.

Since in this problem, an internal flow is dealt with and no complex geometrical features are present as mentioned, the mesh can be relatively simple in terms of its topology and geometry. There is not much 'freedom' for the flow since it is confined by the tube, and the flow passage is relatively small when disturbed by the presence of the pod. Since the mean flow direction is more or less distinct and in one direction, a structured grid is deemed to be most suitable in order to capture the different flow phenomena.

Structured grids have a relative simple topology and simple implementation. It therefore generally leads to faster convergence compared to an unstructured grid. To properly resolve the boundary layer, prism layers are added in order to improve the accuracy at wall boundaries. In order to alleviate computational efforts, a wall function is employed such that a much coarser y^+ resolution can be used. The employed wall function will be discussed in more detail in Section 4.3.

The inlet is positioned at $10m$ in front of the pod, a relative small distance, since there is no noteworthy fluid phenomena to be expected in that region. The outlet however, is positioned approximately twice the vehicle length away measured from the tail of the pod. As mentioned, expansion waves are expected to be present near the tail section, which have the possibility to be reflected by the tube walls. A sufficiently large domain is therefore required in order to analyze this and other fluid phenomena. The mesh for the entire domain and a close-up around the pod are shown in Figures 4.1 and 4.2. The mesh consists of 4217 nodes, with the computational domain thus being $110m$ by $2.15m$.
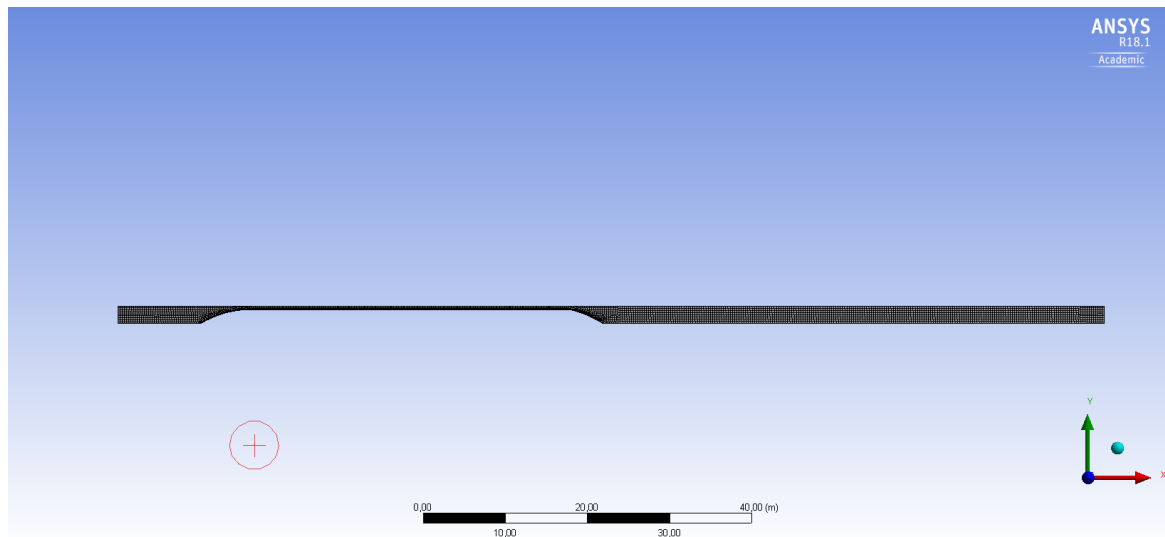
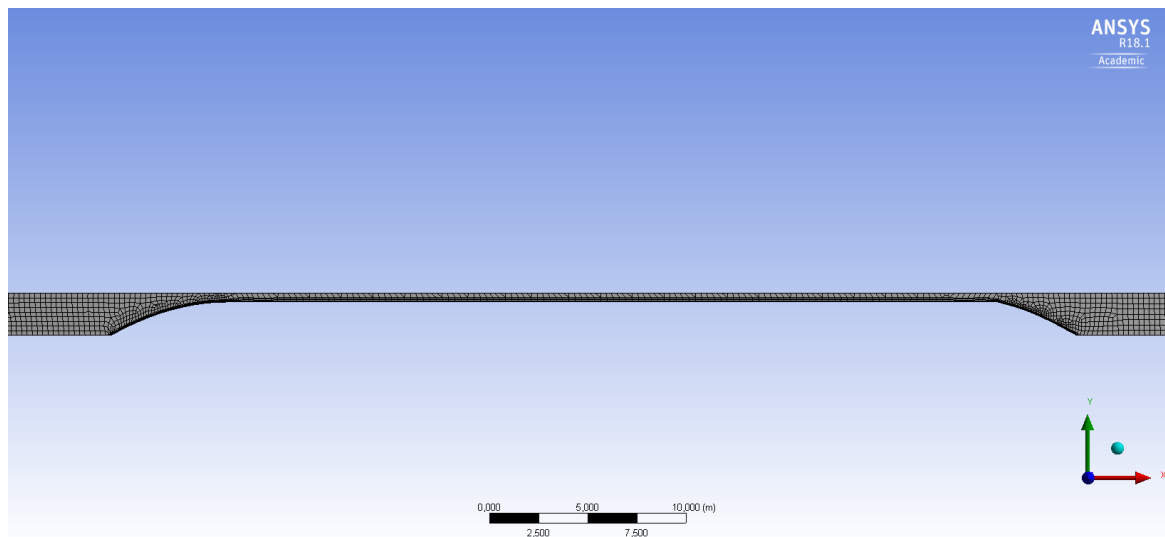Figure 4.1: Mesh of the entire computational domain

Figure 4.2: Close-up of the mesh around the pod

4.3. Model Set-up

With the geometry modeled and a generated grid, the numerical model can now be set-up. This includes the modification of the material (air) and the employment of an appropriate viscous model. Furthermore, an appropriate mathematical model is also designated for the simulation. Finally, the boundary conditions that apply to this problem are also required to be set-up. These different aspects will be covered in this section.

4.3.1. Material Properties

As mentioned before, the air is assumed to behave as an ideal gas, which means that it is also set as an ideal gas within Fluent. This implies that the density will be determined from the ideal gas law, which is an appropriate relationship for compressible flows.

The operating pressure for the air in this case is set to match the internal pressure of the tube, which is $100 Pa$. In Fluent, the operating pressure acts as a reference pressure for calculating the so-called gauge pressure. The absolute pressure is then the sum of the operating pressure and the gauge pressure:

$$p_{abs} = p_{op} + p_{gauge} \tag{4.10}$$

The pressures are split-up in this way in order to avoid numerical round-off errors as much as possible [70]. This is especially significant for regions with a low Mach number in a compressible flow, since in those regions the overall pressure drop is small compared to the absolute static pressure. The pressure changes tend to go to zero as the Mach number goes to zero.

The pressures that are reported and computed by Fluent are the gauge pressures, which means that the operating pressure has to be added to the results in order to arrive at the absolute pressure. The absolute pressure is equivalent to the one that would be encountered in the real environment.

For the definition of the fluid viscosity, Sutherland's law is deployed similar to the law used to determine the dynamic viscosity for the aerodynamic solver, where it is also dependent on the temperature. In this case, a variation of the law is chosen, which is the Sutherland's law with three coefficients:

$$\mu = \mu_0 \left(\frac{T}{T_0} \right)^{3/2} \frac{T_0 + S}{T + S} \tag{4.11}$$

4.3.2. Energy Equation

Since a compressible flow is dealt with, the energy equation has to be deployed as it is now coupled to the continuity and momentum equations. In Fluent, the energy equation is solved in the following form [71]:

$$\frac{\partial}{\partial t}(\rho E) + \nabla \cdot (\vec{v}(\rho E + p)) = \nabla \cdot (k_{eff} \nabla T - \sum_j h_j \vec{J}_j + (\bar{\bar{\tau}} \cdot \vec{v})) + S_h \tag{4.12}$$

The first three terms on the right side of of this equation determine the energy transfer due to conduction, species diffusion and viscous dissipation respectively. Furthermore, the parameter k_{eff} is the effective conductivity which depends on the turbulence model being used. The turbulence model is defined in the viscous model, which will be discussed next.

4.3.3. Viscous Model - Turbulence Modelling

For this fluid dynamic problem, RANS-based CFD analyses are performed. As found from literature, RANS-based simulations are the most widely used simulation methods for general CFD applications. Furthermore, it was also noted that the $k - \epsilon$ model was the most widely employed turbulence model amongst the different RANS turbulence models. The main reason for this can be accounted to the fact that this model performs well for wall-bounded flows.

Therefore, in this research project too, a $k - \epsilon$ model is opted for. However, a slight variation of this model is used: the $k - \epsilon$ realizable model. This variation was first proposed by Shih et. al [72] and is an improvement over the standard model for several reasons.

The standard $k - \epsilon$ model is a semi-empirical one and attempts to describe turbulence by means of two transport equations (PDEs): one for the turbulence kinetic energy k and one for the dissipation rate of the turbulent energy ϵ. While the transport equation for the kinetic energy stems from an exact equation, the one for the dissipation rate is derived from physical reasoning. Consequently, this equation bears little resemblance compared to its mathematical exact counterpart.

The 'realizable' aspect in the improved model implies that certain mathematical constraints are satisfied regarding the Reynolds stresses and as such, are more consistent with turbulent flow physics. A first improvement implemented in the realizable model is therefore a new transport equation for ϵ, which is derived from an exact equation for the transport of the root mean-square vorticity fluctuation [73]. For the realizable model, the transport equation for k is given by:

$$\frac{\partial}{\partial t}(\rho k) + \frac{\partial}{\partial x_j}(\rho k u_j) = \frac{\partial}{\partial x_j}\left[(\mu + \frac{\mu_t}{\sigma_k}) \frac{\partial k}{\partial x_j} \right] + G_k + G_b - \rho \epsilon - Y_M + S_k \tag{4.13}$$

while the equation for ϵ is given by:

$$\frac{\partial}{\partial t}(\rho \epsilon) + \frac{\partial}{\partial x_j}(\rho \epsilon u_j) = \frac{\partial}{\partial x_j}\left[(\mu + \frac{\mu_t}{\sigma_\epsilon}) \frac{\partial \epsilon}{\partial x_j} \right] + \rho C_1 S \epsilon - \rho C_2 \frac{\epsilon^2}{k + \sqrt{\nu \epsilon}} + C_{1\epsilon} \frac{\epsilon}{k} C_{3\epsilon} G_b + S_\epsilon \tag{4.14}$$

Evidently, the transport equation for k has remained unchanged compared to the standard model. In both equations, G_k is the turbulence kinetic energy generated due to velocity gradients, whereas G_b is the turbulence kinetic energy generated due by buoyancy. Furthermore, Y_M in the kinetic energy transport equation which represents the fluctuating dilatation that contributes to the dissipation in a compressible turbulent flow. In compressible flows, the turbulence is affected by dilatation (widening) dissipation, which is more apparent for high Mach number flows. Finally, σ_k and σ_e are turbulent Prandtl numbers, whereas S_k and S_e are source terms for the turbulence.

A new 'feature' in this improved transport equation for ϵ is that the production term (second term on the right hand side in equation 4.14) no longer involves the production of k. This way, the turbulent spectral energy is better represented. Furthermore, the singularity that was present in the standard model has been removed in the improved ϵ equation. As in all $k - \epsilon$ models, the eddy viscosity μ_t is a function of both k and ϵ, given by:

$$\mu_t = \rho C_\mu \frac{k^2}{\epsilon} \tag{4.15}$$

Here lies the second difference between the standard and the realizable $k - \epsilon$ model. In the eddy viscosity equation, C_μ is no longer a model constant which was the case for the standard model. This parameter is now computed by:

$$C_\mu = \frac{1}{A_0 + A_s \frac{kU^*}{\epsilon}} \tag{4.16}$$

The coefficient C_μ is now a function of the mean rotation and strain rates (given by U^*) as well as the turbulence quantities k and ϵ, while A_0 and A_s are model constants. The eddy viscosity is therefore more dependent on the local flow field which means that it is predicted more accurately compared to the standard model [74].

These two main differences from the standard model lead to the fact that the realizable model gives superior results for flows where separation and recirculation occur, as well as boundary layer flows under strong adverse pressure gradients. Furthermore, it also provides improved predictions for the spreading of (axisymmetric) jets and abilities to capture the mean flow of complex structures more accurately. For a wide range of flows (e.g. rotating flows, channel flows, etc.), the realizable model is validated and proven to be substantially better than the standard model [75, 76]. Since the flow in this research problem is assumed to behave as a flow where (a region of) separation is assumed to be presented within a channel, the realizable model is chosen.

Finally, when employing the $k - \epsilon$ model, a near-wall treatment is to be chosen. Turbulent flows are significantly affected by the presence of walls [77], and thus especially in the case for the flow around a Hyperloop pod which is wall-bounded.

An obvious effect of walls on the velocity profile is the no-slip condition, which will be discussed in the next subsection. A less obvious effect however, is also present due to the walls. Very close to the wall, the normal fluctuations are reduced by kinematic blocking, while the tangential fluctuations are reduced due to viscous damping. When the outer part of the near-wall region is considered, the large gradients in mean velocity that exist cause the turbulence to be rapidly augmented by the production of turbulence kinetic energy [78]. Therefore, an adequate near-wall model is required in order to obtain an accurate solution.

As mentioned, it is desirable to have a wall function that allows for coarser y^+ values, in order to reduce the number of nodes and thereby the computational effort. Therefore, a so-called enhanced wall function is employed. This wall function guarantees the correct asymptotic behavior for both small and large values of y^+ and gives a reasonable representation of velocity profiles for cases where y^+ falls within the wall buffer region with an automatic adaption [79]. It is therefore not necessary to have a y^+ value close to 1 to accurately resolve the boundary layer, nor is it required to stay within a specified range of y^+ values as is the case for the standard wall function for instance.

4.3.4. Boundary Conditions

To have a properly defined CFD problem that results in a unique solution, relevant information on (flow) variables are to be specified at the boundaries of the flow domain, better known as the boundary

conditions. Defining the boundary conditions means that the boundaries have to be located first, at which the information is supplied.

The data required at a certain boundary depends on the type of the condition, whereas the boundary conditions themselves mainly depend on the physical models that are employed for the problem. These conditions must be well defined and properly chosen as they have a significant effect on the solution. For this specific problem, there are a total of 5 boundary locations: inlet, outlet, tube wall, pod wall and symmetry plane.

For the inlet, a mass flow boundary condition is used, which is intended for compressible flows. This provides a prescribed mass flow rate at the inlet equation, which is to match the flow condition of $300m/s$ at a tube area of $14.52m^2$. Furthermore, a total temperature has to be prescribed, which is $332K$ based on a Mach number of 0.88.

In physical terms, the specification of a mass flux allows for the variation of total pressure accordingly to the interior solution. This is in contrast to the more general pressure inlet boundary condition, where the total pressure is specified and thus fixed, while the mass flux varies [80]. In the analysis of the flow around the pod, it is more important to match the prescribed mass flow rate than a total pressure, since the choked flow will cause a pressure build-up in front of the pod.

For the outlet, a so called pressure far-field outlet is used. This condition is used to model a free-stream compressible flow at 'infinity', where the static conditions and free-stream Mach number are prescribed.

To bound both fluid and solid regions, wall boundaries are used. In a viscous flow, a no-slip condition is enforced at the walls, which was briefly touched upon in the previous subsection regarding wall effects. One such wall is the surface of the pod. Due to the viscous effects, the fluid that is in direct contact with the wall 'sticks' to the surface, and no slipping is present, hence the name of the condition. Physically, this condition implies that the tangential fluid velocity is equal to the wall velocity, whereas the normal component is equal to zero.

The no-slip condition is also applied to the tube wall. In addition, a moving wall boundary condition for this location is employed, to simulate the movement of the pod through the tube. Therefore, a translational wall motion is invoked moving with an absolute velocity of $300m/s$ in x-direction. A general heat flux is applied for the thermal conditions at the wall.

Finally, the bottom part of the flow domain, coinciding with the x-axis, is modeled as an axis boundary condition. This axis acts as the centerline of the pod which is axisymmetric as discussed. The boundary conditions and their specifications are listed in Table 4.1 below.

Table 4.1: Specification of boundary conditions

Boundary	Type	Specifications	Value	Unit
Inlet	Mass flow inlet	Mass flow rate	5.268	kg/s
		Total temperature	332.78	K
Outlet	Pressure far-field	Static pressure	100	Pa
		Free-stream Mach number	0.882	-
Pod surface	Wall	No-slip condition	-	-
Tube wall	Wall	Translational velocity	300	m/s
		No-slip condition		
x-axis	Axis	Plane of (rotational) symmetry	-	-

4.4. Results and Comparison with Aerodynamic Solver

The flow field around the pod is depicted in Figure 4.3 , where a contour plot of the local Mach number is shown for the entire domain as well as a close-up on the pod which is shown in Figure 4.4. The results of the simulation show that for the baseline model, the aerodynamic drag is approximately $3.98kN$.
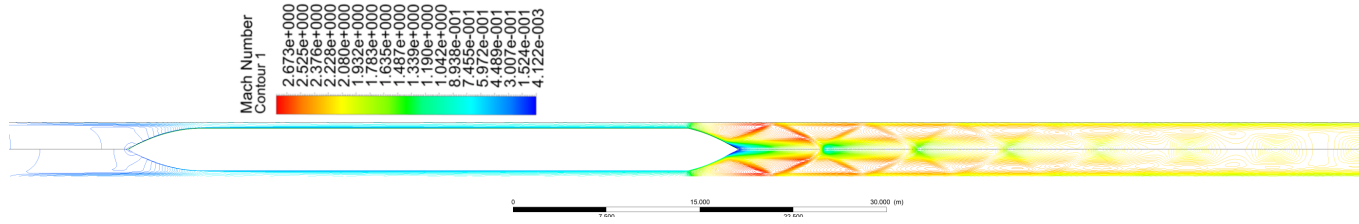
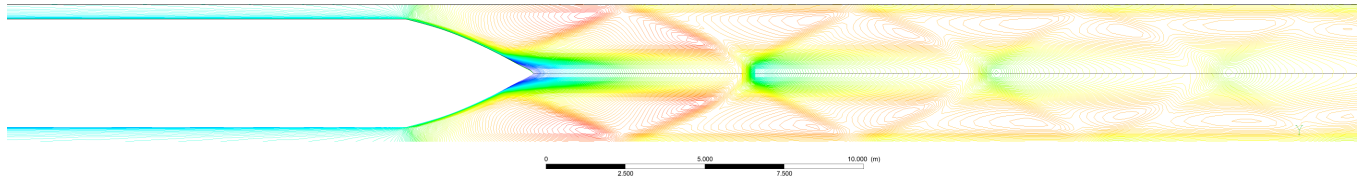Figure 4.3: Mach contours around the baseline pod - full domain

Figure 4.4: Mach contour plot - close-up on the aft region

From the contour plots, it can be seen that the maximum Mach number throughout the domain is 2.67, which occurs at the end section of the tail in front of the (oblique) shock wave that is clearly visible. Recalling the analogy that was made between this flow domain and the flow through a nozzle, the flow behaviour can more accurately be regarded as a flow through an overexpanded nozzle. This implies that the exit pressure is lower than the back pressure, which in this case is the internal tube pressure. The jet therefore has to pass through oblique shocks in order to rise back up to the tube pressure. Additionally, these shocks are reflected due to the presence of the tube walls, where they then slowly fade out and are barely visible after three reflections. A small region of separated flow is also noted approximately $1m$ before the end of the tail. Finally, expansion fans on the upper and lower surface of the pod are observed at the location of the throat, where the flow accelerates and transitions from subsonic to supersonic velocities. The residuals of the velocities, continuity, energy and turbulence model and their convergence histories are shown in Figure 4.5.
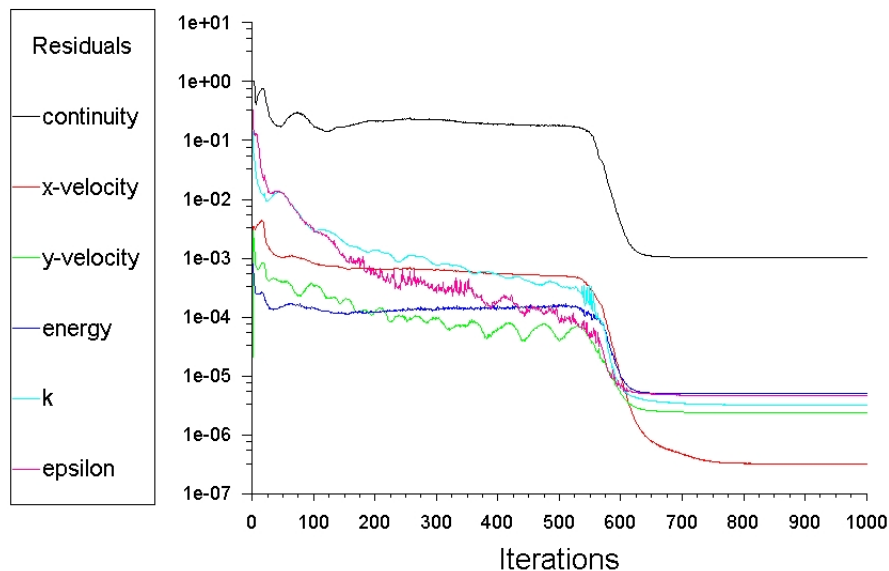

Figure 4.5: Residuals monitor

It can be seen that after approximately 550 iterations, the residuals drop to their converged values, as all residuals drop below 1e-5 except for the continuity, which is at approximately 1e-3. The x-

velocity requires a larger number of iterations to drop to its converged level, since this is the mean flow direction.

The pressure and Mach number distributions throughout the domain are shown in Figures 4.6 and 4.7 respectively. For brevity, the results of the aerodynamic solver are presented as well in the same figure in order to make comparisons. The origin of the domain is placed at the nose of the pod, which is why the graph of the domain starts at $-10m$. Additionally, the distributions along the surface of the pod are shown as well.
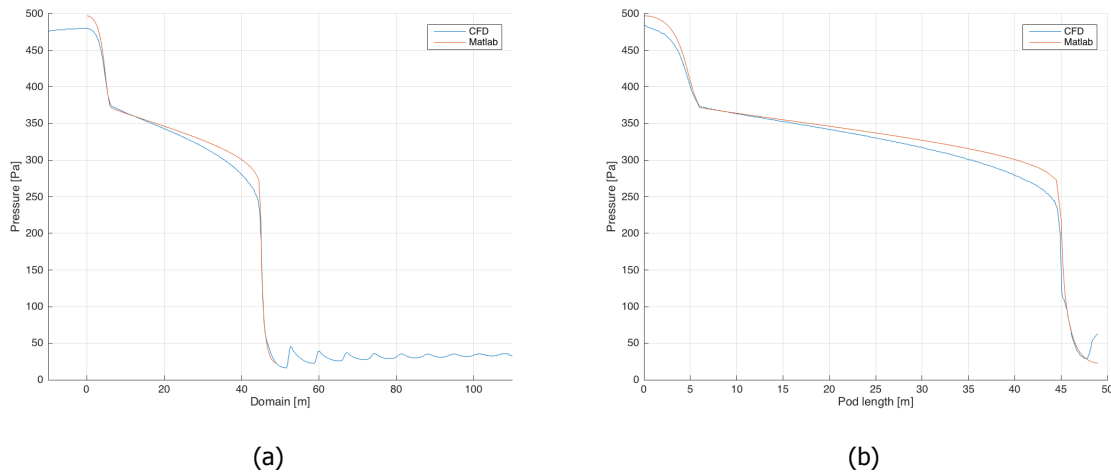

(a) (b)

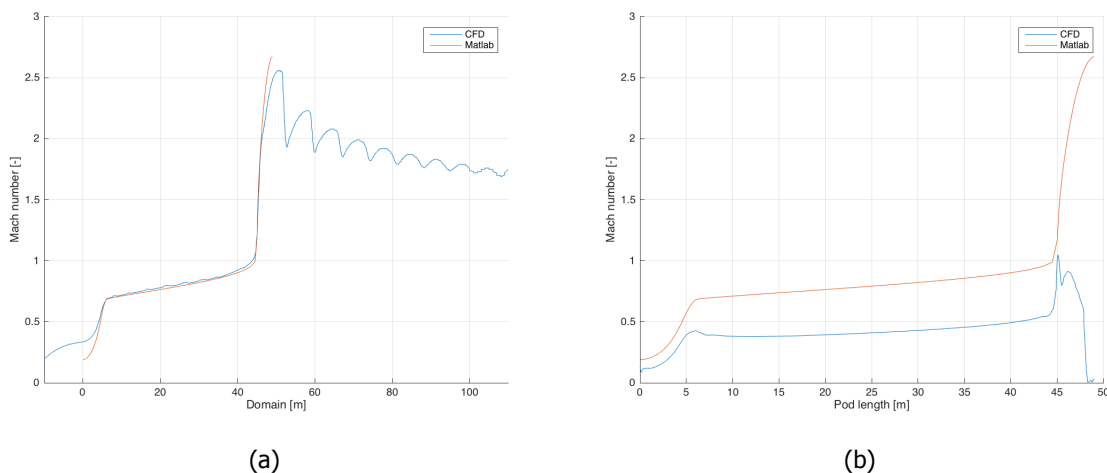Figure 4.6: Pressure distributions of the domain (a) and the pod surface (b)

(a) (b)

Figure 4.7: Mach number distributions of the domain (a) and the pod surface (b)

From the pressure distributions, the high pressure peak that exists at the nose is evident due to violation of the Kantrowitz limit. It can furthermore be noted that the modeled distributions generally agree well with the CFD results, where the main trend is captured as well. This is however to a lesser extent when the distribution directly over the pod surface is compared, due to the 2D effects that were not taken into account with the solver. The same holds for the comparison of Mach number distributions, where the maximum Mach number of 2.7 agrees well with that found in the entire domain, but again do not hold for distributions directly over the pod surface.

These results will be further interpreted and elaborated in Section 4.6, after the CFD results have been verified. Similar distributions of various flow quantities are presented in Appendix 4.4.

4.5. Verification of Numerical Model

As mentioned before, there is no aerodynamic experimental data available (yet) of a Hyperloop pod. Therefore, the CFD simulations cannot be validated. The verification process is therefore the only method towards building confidence in the obtained CFD results. Errors of numerical solutions can typically be classified under three categories:

- Discretization errors, attributed to the difference between the exact solution of the conservation equations and the solution as obtained by the algebraic system of equations due to discretization of these equations

- Convergence errors, defined as the difference between the exact solution and the iterative solution

- Modeling errors, which can be described as the difference between the real physical problem and the solution of the mathematical model

Various procedures can be followed in order to verify the simulation results, and to determine whether the aforementioned errors are present in the solutions.

4.5.1. Grid Convergence

An important verification process is to check for discretization errors. These errors depend on both the grid quality and cell size. A grid convergence check is therefore performed in order to ensure that the final solution is independent of the grid, by running the simulation again for a higher mesh resolution. When the results are comparable, this gives the confidence that the solution is independent on the mesh.

First of all, the general mesh is refined by increasing the number of cells within the entire domain. The total number of cells is increased by a factor of approximately 4 over the entire domain domain, yielding a total of 12,668 cells. Furthermore, additional inflation layers are added to the pod surface, from 3 to 7 layers. A close-up of the refined mesh around the nose area of the pod is shown in Figure 4.8.
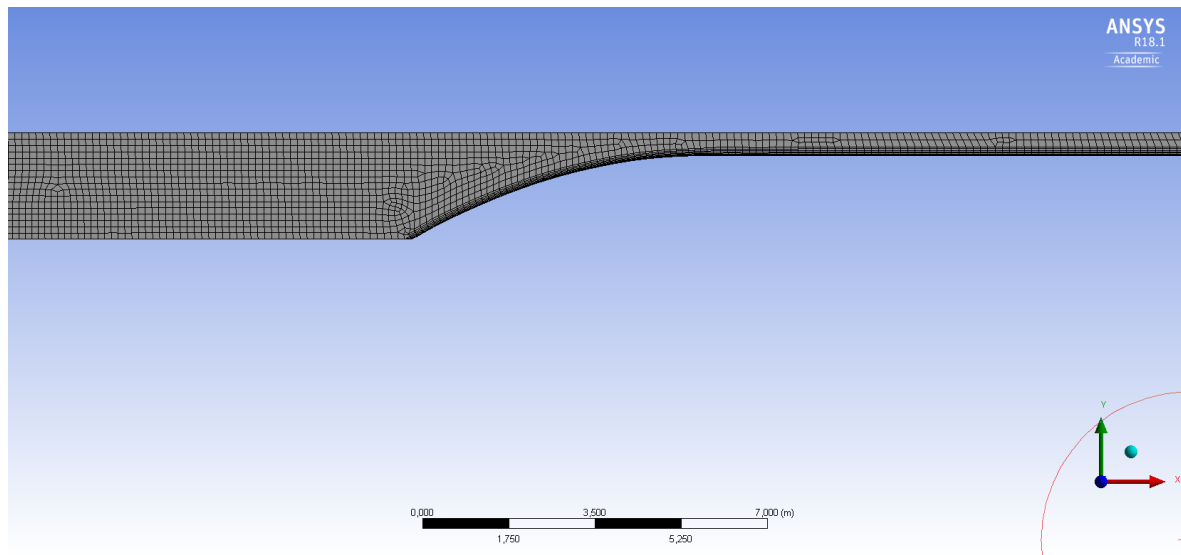
Figure 4.8: Nose area refined mesh - First refinement

Finally, a second level of refinement is employed by means of an adaptive mesh, where refinements are made at the location of the expansion waves, shockwaves and their reflections. This second refined mesh is shown in Figure 4.9. Subsequently, the Mach contours around the tail area of the pod for the coarse and adapted meshes are shown and compared in Figure 4.10, where the upper and lower parts correspond to coarse and adapted mesh solutions respectively.

Figure 4.9: Tail area adapted mesh - Second refinement

Figure 4.10: Tail area Mach contours for the coarse (upper half) and adapted mesh (lower half)

The contour plot of the refined mesh shows a similar flow domain and flow behaviour compared to the coarse mesh solution, with comparable maximum Mach numbers (0.78% difference)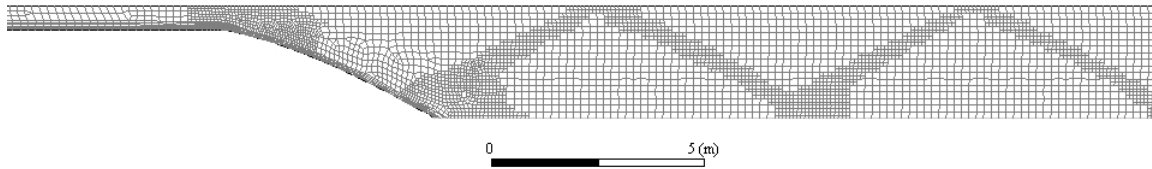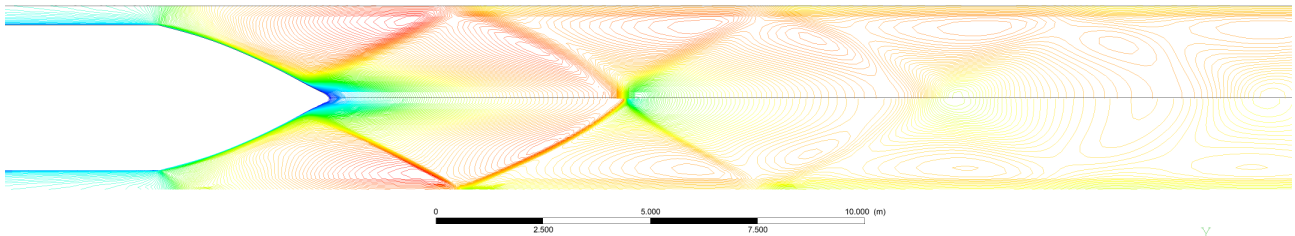 attained throughout the fluid domain. The location of the expansion waves are similar and the (reflected) oblique shock waves are clearly visible again and at the same location as well. A notable difference is that the thicknesses of these waves are reduced in this case. This also confirms that the refined mesh is converging towards a realistic solution, since these locations are better resolved, the exact boundaries of these expansion waves can also be better solved for.

4.5.2. Residual Analysis

Analyzing the residual trends is one of the most fundamental measures in determining whether a solution is converged or not. It directly quantifies the error in the solution of the system of equations. The trends of the baseline simulation were already shown and discussed. For both refined meshes, the convergence history of the residuals is shown in Figure 4.11. As expected, more iterations are required for convergence due to the higher number of cells, with approximately 1150 and 1450 iterations required in order to achieve convergence for the first and second refined meshes respectively.
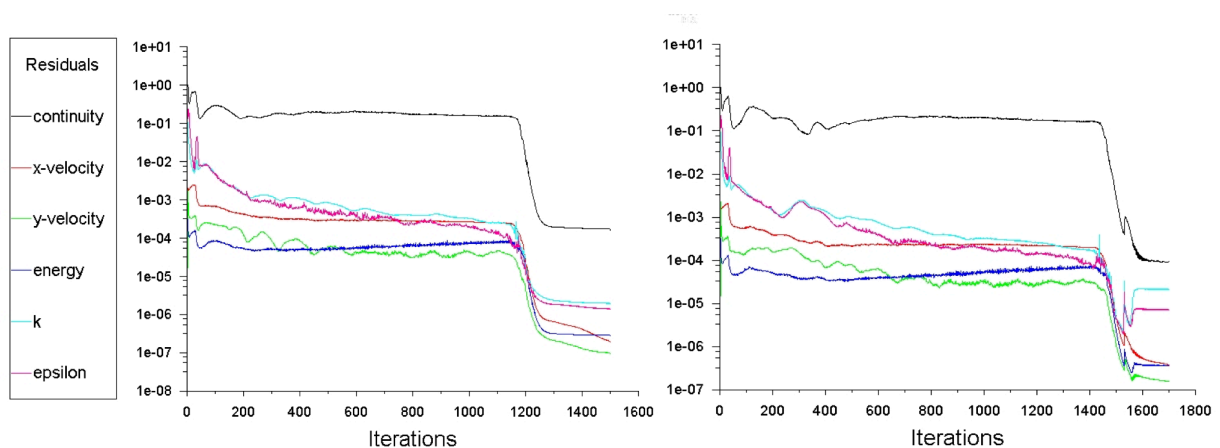

Figure 4.11: Residuals of the first (left) and second (right) refined meshes

The overall convergence trend is similar to the one found for the coarse mesh, where a rather sudden decrease in RMS values is observed for the residuals after a certain amount of iterations.

In addition to the trend of the residuals, an additional monitor is set-up in order to assess the convergence of the drag, which is the main figure of merit in this research project. The trends of the total drag for the three different meshes are shown in Figure 4.12.
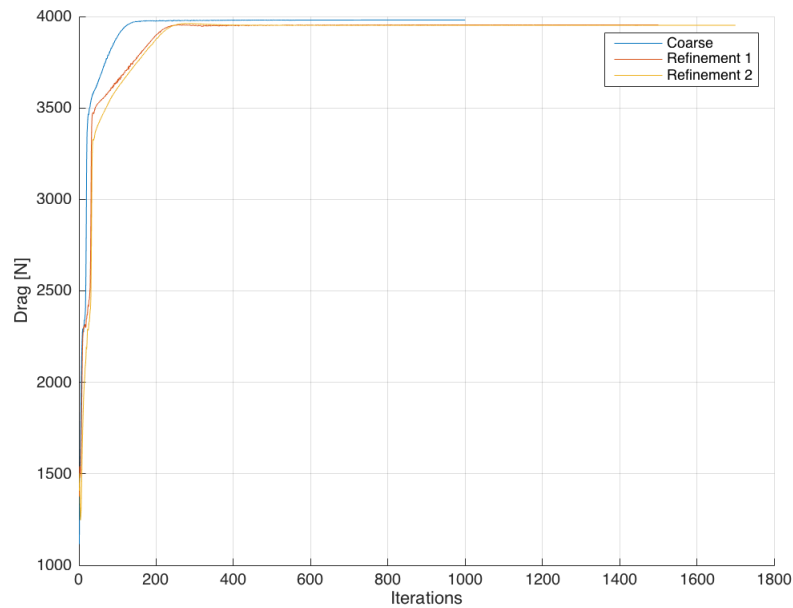

Figure 4.12: Drag convergence monitor for three different meshes

For all three meshes, the trend for the total drag is similar with slightly different final values. After a certain amount of iterations, the drag reaches its final value and remains constant. The final values for the total drag are $3981N$, $3954N$ and $3952N$ for the coarse, refined and second refined meshes respectively, a difference of approximately 0.73% between the coarse and both refined meshes. Again, the denser grids require more iterations towards convergence as expected. It is noted that the drag requires a substantial lower amount of iterations to reach its final value compared to the residuals. These observations are positive contributions towards gaining confidence in the CFD results.

4.5.3. Conservation of Quantities
A third way in verifying the results is to look at the mass conservation throughout the domain, and specifically at the boundaries. If mass conservation is satisfied, the net mass flow rate over the domain should be equal to 0. This can be confirmed by looking at the rate at the inlet and outlet of the domain. The flow rates at the inlet and outlet are $5.268924 kg/s$ and $-5.2689174 kg/s$ respectively, yielding a net flow rate of $6.65 \cdot 10^{-6}$. The negligible net flow rate thus confirms that mass is conserved throughout the domain.

4.6. Discussion and Conclusion
CFD simulations were performed in order to validate the aerodynamic solver which was described in Chapter 3. The CFD simulations yielded reliable solutions as far as verification processes concerned. Grid checks showed that the solution is independent of the grid and general conservation laws are satisfied with a proper convergence of different residuals. The results from the simulations are therefore regarded as a proper benchmark for the aerodynamic solver.

The implications of (exceeding) the Kantrowitz limit are evident from the pressure distributions, where a high pressure is observed at the nose of the pod. This pressure peak is higher than the pressure peak that is to be expected due to a stagnation point at the nose, implying that the pressure peak has build-up significantly due to the flow being choked. As was expected, the flow accelerates through the bypass areas up to sonic conditions at the throat, which is located at the inflection point

where the pod transitions from the constant radius section to the tail section.

Results from CFD simulations and results obtained from the aerodynamic solver show good agreement regarding distributions of aerodynamic quantities of interest. The overall trend is well captured and for the main distribution of interest, that of the pressure, the difference in average values is approximately 9.8%. The differences were most notable at the nose section and tail sections of the pod.

From the comparison of pressure distributions, it became clear that the pressure over the flat surface of the pod is slightly overpredicted by the solver. The prediction of the boundary layer development plays a crucial role in this accuracy. As discussed, the boundary layer thickness adds an effective height towards the original radius of the pod, thereby influencing the acceleration of the flow through the bypass area. The behaviour of the boundary layer modeled through the Blasius solution shows the limitation of assuming a gradual, monotonic growth in boundary layer thickness. Therefore, the difference in pressure increases with downstream position, as the difference in boundary layer thickness increases.

The development also depends on the transition point, which in this case was based on a critical Reynolds number associated to that of a flat plate. It must be noted that the critical Reynolds number is strongly dependent on the degree of perturbation of the outer flow, where higher values of Re_{crit} can be reached for particular smooth flows (up to $3 \cdot 10^6$) [8, 59]. The assumption that the flow is highly perturbed (leading to the current Re_{crit} value of $5 \cdot 10^5$) along with the fact that the flat plate assumption is made, possibly add to the inaccuracy in predicting the boundary layer development.

The inaccuracy of the pressure development over the flat portion of the pod has little influence on the prediction of the pressure drag since there is no pressure component parallel to the flow direction, and the pressure distributions of the nose and tail sections are more critical in that sense. It is however, related to the difference in predicted throat area, which indirectly influences the pressure peak at the nose location. The pressure peak at the nose is overpredicted by the solver by approximately 3.5% due to an underpredicted throat area, suggesting that the displacement thickness at the throat location is overpredicted. It is likely that the boundary layer decreases in thickness close to the throat location due to suction caused by the low pressure area around the tail, which is in this case is not modeled either. This thus leads to an overpredicted pressure drag, with $3.88kN$ and $3.67kN$ determined by the solver and CFD respectively. The opposite is noted for the friction drag, where the solver predicts a lower drag of $217.49N$ compared to $278.2N$ found through CFD. This difference is mainly attributed to the employed turbulence model which assumes a fully turbulent flow, whereas the solver assumes a partially laminar flow region. This combination results in a higher total drag predicted by the solver, with $4.1kN$ compared to the earlier mentioned $3.95kN$ obtained with CFD.

Other limitations of the solver are clear as well. Only the distributions starting from nose to end of the pod can be predicted by the solver. As such, phenomena like the oblique shock waves and its reflections are not modeled and their effects are not taken into account. However, it is assumed that these waves do not have a significant impact on the aerodynamic drag of the pod, since the shocks are relatively weak due to the low pressure environment and do not significantly alter the pressure distributions.

The implications of the quasi-1D flow assumption are clearly visible in the distributions of the flow parameters. When comparing the solver and CFD results, the distributions agree well with each other for a location close to the tube wall, where similar trends and maximum values are reached for instance. However, when comparing the results with the distributions directly over the pod surface, a larger difference is observed. Clearly, the 2D effects are visible here showing that the quantities do not remain constant over the lateral direction for a certain longitudinal section, but are certainly disturbed by the presence of the pod. The results of the solver should therefore be interpreted as mean properties that are averaged over each local cross-sectional area.

Evidently, the velocity of the flow is lower close to the pod due to the viscous effects and the interaction with the boundary layer. Furthermore, the small region of separation at the trailing edge of the tail is not modeled either, leading to an underpredicted pressure by the solver at that specific section. Nonetheless, the important trends and prediction of total drag are considered to be accurate enough and adequate in having a low computational cost model that can predict the flow behaviour and the total aerodynamic drag. The added complexity of predicting and modeling a separated flow which is a highly random process, is deemed to not weigh-out against the little improve in accuracy for the drag prediction and flow field. The solver is thus regarded as a suitable low-fidelity model that can

be utilized to assess the influence of different parameters on the drag of the pod and to be coupled to an optimization routine.

5

Specification and Results of Optimization

In general terms, an optimization problem can be regarded as a problem where the optimal solution is found from all feasible solutions. What is regarded as optimal is then defined by the objective function. This function, together with the constraints, then form the design space in which all feasible solutions lie. A proper specification of the optimization problem is required in order to adequately define and structure the problem, and is thereby an important aspect in any optimization procedure. A mathematical description is often the starting point of an optimization problem, which states what exactly is to be optimized, the constraints its subjected to and the bounds in which the different design variables can lie. The validation of the aerodynamic solver allows it to be used for optimization procedures regarding the drag reduction of the Hyperloop pod. By means of the sequential quadratic programming method, an improved shape of the Hyperloop pod in terms of its aerodynamic drag is sought after.

5.1. Normalization of Parameters

For the optimization routine, the sequential quadratic programming method is used, which is a gradient based, iterative method for constrained optimization procedures. When a gradient-based search algorithm is used, the magnitude of the variables is an important factor to consider. Since the variables can vary by large order of magnitudes (e.g. CST coefficients compared to the drag), all variables are normalized. This is done such that all variables that are involved with the optimization process have the same order of magnitude, in order to reduce the inaccuracy of the optimizer. In this optimization problem therefore, the design variables, constraints, bounds and objective function are all normalized with respect to their initial values.

5.2. Design Vector

For the optimization problem, a design vector is required in which all variables that are allowed to vary are included. Furthermore, the objective function and constraints are all functions of these design variables.

In this case, the size of the design vector $\bar{x}$ is governed by the number of CST coefficients that are required for the geometries of the nose and tail, as it mainly consists of those parameters. The design vector therefore consists of 24 design variables: the 20 CST coefficients and design 4 variables for the definition of the lengths and radii of the nose and tail.

The initial design variables along with their values are listed in Table 5.1, with a total of 24 design variables as mentioned. In addition, the upper and lower bounds of the CST coefficients are set at 1.8 and 0.2 respectively to reduce the design space while still allowing sufficient design flexibility, while the lower bounds of the nose and tail lengths are set in light of minimum pod volume requirements.

Table 5.1: Optimization design variables

$\bar{x}_0$ Entry	Design parameter	Initial value	Unit
1:20	$CST_{1:20}$	CST_0 (Table 3.2)	-
21	R_{nose}	1.7	m
22	R_{tail}	1.7	m
23	L_{nose}	6	m
24	L_{tail}	4	m

5.3. Constraints

As mentioned, this optimization problem is one in which constraints are present. These are set in order to achieve a solution that is not only mathematically feasible, but moreover also physically feasible. Evidently, one such physical constraint is that the radius of the pod cannot exceed that of the tube. It must be noted that it does not suffice to mathematically state that the pod radius is to be smaller than the tube radius. The effective radius of the pod is the limiting factor, which means that the boundary layer height must be included in this constraint. This is thus regarded as a so-called inequality constraint, and is mathematically described by:

$$g_1 = \frac{R_{pod,effective} - R_{tube}}{R_{pod,0}} \leq 0 \tag{5.1}$$

Again, the inequality constraint is normalized by the initial pod radius. Besides this inequality constraint, there are also 2 equality constraints for this problem. One of the limitations of the solver is that it cannot predict flow separation. Therefore, a possibility exists in which geometries are deemed feasible where a relative large gradient in the local curvature is found. In reality, this would impose an area of flow separation which naturally does not lead to an improved aerodynamic performance. Therefore, a constraint is introduced which ensures a continuous and somewhat smooth transition between the nose and constant section. A similar case arises for the tail section, which therefore yields 2 normalized equality constraints. These constraints are also set in light of volume requirements.

The last section of the nose and first section of the tail are constrained to have the same radius as the constant section. This constraint will still allow for changes in the nose and tail radii, and are defined by:

$$h_1 = \frac{y_{nose,end} - R_{pod}}{R_{pod}} = 0 \tag{5.2}$$

$$h_2 = \frac{y_{tail,begin} - R_{pod}}{R_{pod}} = 0 \tag{5.3}$$

5.4. Constants

Some of the parameters that are required for calculations but stay constant throughout the optimization process are part of the constant vector $\bar{c}$. The parameters that are contained within by this vector are listed in Table 5.2.

Table 5.2: Parameters that remain constant during the optimization process

$\bar{C}$ Entry	Parameter	Description	Value	Unit
1	T	Static temperature	288.15	K
2	p	Static pressure	100	Pa
3	V	Pod velocity	300	m/s
4	γ	Ratio of specific heats	1.4	-
5	R	Gas constant	287	J/kg·K
6	M_∞	Free-stream Mach number	0.88	-
7	C_p	Specific heat at constant pressure	1005	J/kg·K
8	Re	Free-stream Reynolds number	$9.735 \cdot 10^5$	-
9	q	Dynamic pressure	54.41	Pa
10	R_{tube}	Tube radius	2.15	m
11	R_{pod}	Pod radius (constant section)	1.7	m
12	μ	Dynamic viscosity	$1.812 \cdot 10^{-5}$	kg/m·s

5.5. Formal Specification

The optimization can finally be mathematically specified. As the objective of this optimization problem is to minimize the aerodynamic drag of the pod, the objective function will consist of the drag, expressed as a function of the design variables. The objective function, constraints and bounds are then formulated as follows:

$$\min_{\bar{x}} J(\bar{x})$$

where

$$J(\bar{x}) = \frac{C_D(\bar{x})\frac{1}{2}\rho V^2 S}{D_{initial}}$$

subjected to the inequality (g_1) and equality ($h_{1,2}$) constraints:

$$g_1(\bar{x}) \leq 0$$

and

$$h_{1,2}(\bar{x}) = 0$$

with bounds

$$x_n^L \leq \bar{x} \leq x_n^U \quad \text{for } n = 1,2,...,24$$

5.6. Implementation in MATLAB

The optimization is performed in MATLAB, where use is made of $fmincon$, a non-linear programming solver. This function finds the minimum of a constrained, non-linear multivariable function. The basic syntax for this function is as follows:

$$x = fmincon\big[@(x)\ HL_{obj}(x, x0, C), x, A, b, Aeq, beq, lb, ub, @x\ HL_{nonlcon}(x, x0, C), options\big]$$

The function starts at the initial design vector x_0 and attempts to find a minimizer x of the function described in HL_{obj}, subject to the linear (in)equalities c(x) and c_{eq}(x) defined in $nonlcon$, which is specified as a function handle. In this case, x_0 is the initial design vector as specified in Section 5.2.

Additionally, the optimization can be further specified in $options$. The most important options in this case are the different tolerances. These tolerances determine the stopping criteria of the optimization, thus also affecting the number of iterations. A total of 3 tolerances are present for this problem: function tolerance, step tolerance and constraint tolerance.

The function tolerance, $TolFun$, is a lower bound regarding the change of the objective function for an iteration. In this case, $TolFun$ is set at 1e-4, as an improvement of the objective function in the order of 1e-5 is deemed to not weigh out against the added computational time.

The step tolerance, $TolX$, is similar to this with the difference that it is related to the stepsize of each iteration. This tolerance is set at 1e-8. Both tolerances are lower bounds, meaning that the iteration process will end when the last performed step is smaller than either $TolFun$ or $TolX$. Both tolerances are illustrated in Figure 5.1 [81].
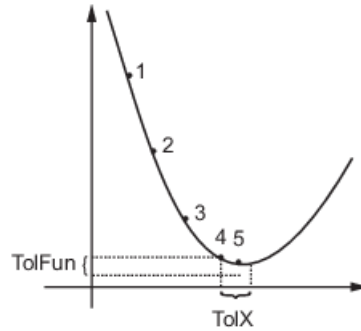

Figure 5.1: Implications of the function and step size tolerances

The constraint tolerance $TolCon$ ensures that the constraints are satisfied with a certain margin. In this case, the tolerance acts as an upper bound as opposed to the previous two tolerances. The optimizer will therefore not be halted when this tolerance is satisfied, but serves as a confirmation of the solution to be feasible.

Finally, within $fmincon$, a sequential quadratic programming (SQP) algorithm is opted for due to its robustness, higher accuracy and numerical efficiency compared to other available algorithms [82]. The SQP method solves a quadratic programming subproblem at each iteration, which consists of a quadratic approximation of the Lagrangian function [83, 84]. The Hessian of this Lagrangian function is approximated, for which the solution of this subproblem is then used to form the basis for the next iteration step. The Lagrangian based on the optimization problem as stated in the previous section is given by:

$$\mathcal{L}(\bar{x}, \lambda, \sigma) = J(\bar{x}) - \lambda^T g(\bar{x}) - \sigma^T h(\bar{x}) \tag{5.4}$$

5.7. Results and Comparison With Baseline

The final geometry that resulted from the optimization routine is shown in Figures 5.2 and 5.3 for a comparison with the baseline geometry. The initial and final design parameters that led to the optimized geometry are listed in Table 5.3.

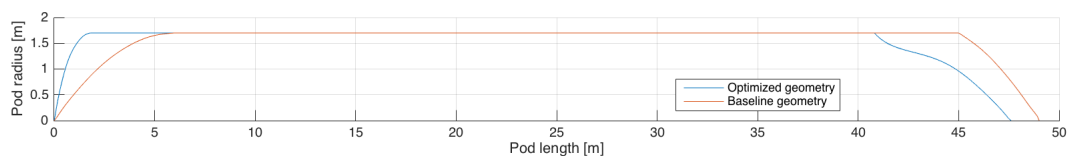Figure 5.2: Optimized pod geometry

Figure 5.3: Comparison of optimized and baseline pod geometry

$\bar{x}$ Entry	Parameter	Initial value	Final value	Normalized optimal value
1	CST_1	-0.0131	-0.0118	0.9008
2	CST_2	0.3518	0.3869	1.0997
3	CST_3	0.4096	0.4505	1.0998
4	CST_4	0.6768	0.7030	1.0387
5	CST_5	0.8394	0.8291	0.9877
6	CST_6	0.8046	0.7401	0.9198
7	CST_7	0.9911	0.8919	0.8999
8	CST_8	0.9993	0.9938	0.9944
9	CST_9	0.9998	0.8991	0.8992
10	CST_{10}	0.9999	0.8999	0.8999
11	CST_{11}	0.9999	1.0999	1.1001
12	CST_{12}	0.9999	0.8998	0.8998
13	CST_{13}	0.9999	0.8994	0.8995
14	CST_{14}	0.9997	0.8919	0.8921
15	CST_{15}	0.9987	0.8124	0.8135
16	CST_{16}	0.9124	0.8702	0.9537
17	CST_{17}	0.7802	0.6872	0.8808
18	CST_{18}	0.9561	0.4090	0.4278
19	CST_{19}	0.4332	0.3049	0.7038
20	CST_{20}	0.4893	-0.1311	0.2679
21	R_{nose}	1.7	1.8891	1.1111
22	R_{tail}	1.7	1.5456	0.8439
23	L_{nose}	6	1.8	0.3000
24	L_{tail}	4	6.8	1.7000

Table 5.3: Initial and final design variables

From both Figure 5.3 and the final values of $\bar{x}_{23}$ and $\bar{x}_{24}$, it can firstly be noted that the nose of the optimized pod has shortened substantially, which is now equal to $1.8m$. The opposite is true for the tail, which length has increased from $4m$ to $6.8m$. As such, the overall length of the pod has decreased from $49m$ to $47.6m$. Furthermore, a concavity in the shape is noted at the tail section which then transitions into a convex shape. The distributions of the Mach number and pressure of the baseline and optimized geometries are also compared and shown in Figure 5.4.
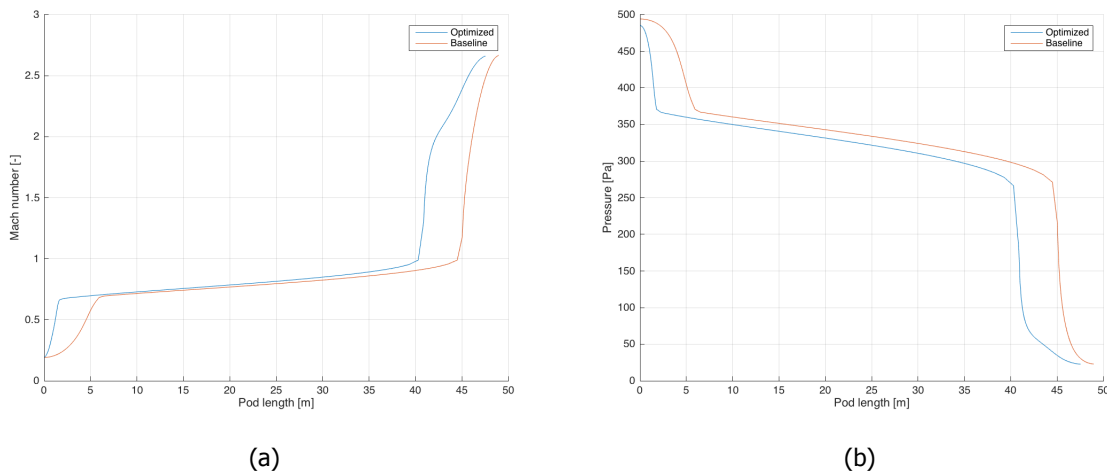

(a)

(b)

Figure 5.4: Comparisons of the Mach number (a) and pressure (b) distributions of the baseline and optimized geometry

The distributions show a similar trend in both quantities for both geometries. Since the nose has shortened, the flow velocity in front of the optimized shape builds up more quickly, leading to a higher pressure gradient in that region. The flow then reaches sonic conditions again at the throat, which is now located at approximately $41m$ downstream of the nose. The flow expands again after the throat section, where it can be seen that it expands more gradually for the optimized geometry. Furthermore, the pressure peak at the nose is slightly reduced for the optimized geometry.

The optimization converged after 37 iterations, in which the objective function has been evaluated 1724 times. The (normalized) objective function has been reduced to 0.8879, thus equivalent to a drag reduction of 11.2% with a final value for the total drag of $3.63kN$. Additional details regarding the convergence history are presented in Appendix B.1.

5.8. Validation of Optimized Geometry

As was specified in the research objective, the result of the optimization will also be analyzed be means of CFD simulations. The same procedure is followed as was presented and discussed in Chapter 4. The flow field around the optimized shape is shown in Figure 5.5.
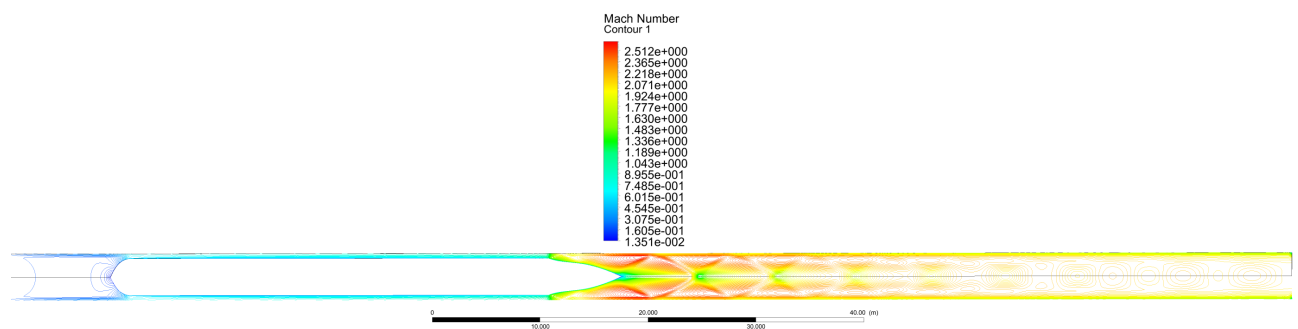

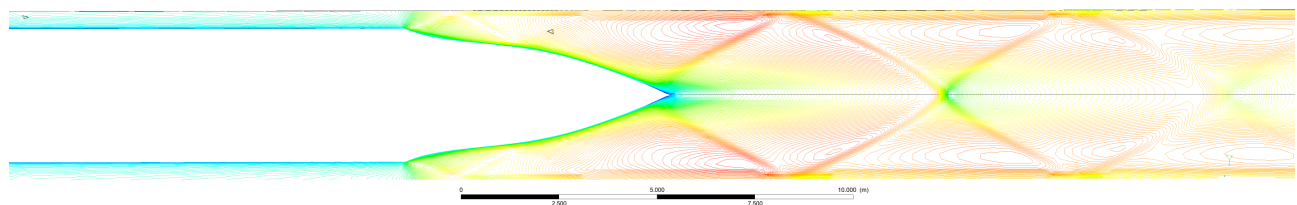Figure 5.5: Mach contours of the optimimized geometry

Figure 5.6: Mach contours tail area - optimized geometry

The contour plots show a similar flow behaviour as for the baseline geometry, where the high pressure region in front of the nose is observed again. The expansion waves are visible again at the tail section. The maximum Mach number throughout the domain has reduced from 2.67 to 2.51, and the region of separated flow has further reduced as well. In agreement with the aerodynamic solver, this geometry has a lower total drag, albeit a lower reduction of 7.2% with a total drag now equal to $3.66kN$. Again, a closeup on the tail region is depicted and is shown in Figure 5.6. Similar convergence trends of the residuals and the drag convergence are observed as was earlier discussed for the baseline simulations. These monitors are shown in Appendix B.2.

5.9. Discussion and Conclusion

The aerodynamic solver that was set-up and described in Chapter 3 has been coupled to an optimization scheme, with the goal of finding a pod shape that has the lowest aerodynamic drag while adhering to certain geometrical and functional requirements. An SQP algorithm is utilized, which is a gradient based, iterative method for constrained nonlinear optimization. The optimization led to a total drag reduction of approximately 11.2 %, which took 1724 function evaluations spread over 37 iterations.

From the geometries, it is clear that the nose has shortened substantially for the optimized geometry, while the opposite is true for the tail section, leading to a reduction in total pod length from $49m$ to $47.6m$. This is also seen through the final values of the design variables, where the nose and tail lengths are on their lower and upper bounds respectively.

Since the pod is operating at a combination of blockage ratio and velocity where the Kantrowitz limit is exceeded, the pressure build-up in front of the pod is prevalent and cannot be avoided by shape manipulation alone (assuming that the tube radius stays constant). Therefore, streamlining the nose would have no effect in reducing this high pressure area as would be the case for external aerodynamics. It is therefore most efficient to shorten the nose section in order to minimize the friction drag. The design variable of the nose length is therefore on its lower bound, which was set in order to meet the volume requirements.

The shortening of the nose not only contributes to a lower friction drag, but more importantly contributes to a less developed boundary layer when the throat location is reached. Since the distance from the nose up to the throat is now lower, the thickness of the boundary layer at that location is also smaller, leading to a larger throat area. The larger throat area will have an effect on the entire Mach number distribution, since this distribution is dependent on the ratio of local area to throat area. The choking effect has therefore also reduced due to this larger throat area, which led to a slightly lower pressure peak for the optimized geometry. Recalling the equation of the choked mass flow rate, it is noted that this quantity is proportional to the throat area:

$$\dot{m}_{choked} \propto \frac{p_0 A^*}{\sqrt{T_0}} \tag{5.5}$$

Thus, an increase in throat area leads to a larger choked mass flow rate. Combined with the implication that the general (effective) bypass area has increased as well, overall larger velocities over the pod are observed, analogous to lower pressures. This can also be seen in Figure 5.4, where the Mach numbers are compared.

While the shape of the nose has little influence on the pressure drag, the tail section does to a large extent influence the amount of this drag component. Evidently, the expansion process starts from the tail section onwards, where the expansion fans are also visible. The more streamlined and thus more gradual decrease in radius compared to the baseline geometry allows for a more gradual flow expansion, as can be seen from the pressure comparison figure, where the pressure gradient is lower at the tail section for the optimized geometry. Furthermore, the Mach contour plots also show a smaller area of separation compared to the baseline design.

When looking at the CFD results, the decrease in drag was less, where a reduction of 7.19% was achieved. This was to be expected as the aerodynamic solver is more 'optimistic' in its prediction due to different flow phenomena that are not taken into account, such as the flow separation at the tail section for instance. The aforementioned implications of the assumptions regarding the boundary layer model for the aerodynamic solver also cause the deficit in drag reduction.

6

Conclusion and Recommendations

Increasing environmental concerns and the rising demand of high-speed transportation has motivated the research and development of the Hyperloop. A careful aerodynamic design and analysis of this new transportation mode is necessary in order to realize the promised the benefits. The HARDT Hyperloop encounters an unconventional flow regime: low Reynolds numbers (slightly under a million) with relatively high Mach numbers (M≈2.7 locally) in a confined space. This brings with it its own unique aerodynamic challenges that have to be dealt with, and thus necessitates a thorough and careful investigation on the (relatively unknown and wide) aerodynamic design space of the pod.

The main aim of this research project is to investigate the aerodynamic characteristics of the Hyperloop pod, whereby the objective is to find a pod shape that minimizes the total drag compared to a baseline geometry while adhering to certain (functional) requirements.

This Chapter will discuss the main conclusions drawn from this research project, whereby the main research question and its sub-questions that were initially presented are referred back to and answered. Thereafter, recommendations are made for possible improvements and continuation based off this work.

6.1. Research conclusions

To realize the objective of this research project, an aerodynamic solver was developed and CFD simulations were performed in order to validate this solver. As far as the verification of the numerical model concerned, the results of the CFD simulations were deemed as a proper benchmark and reliable source for the validation of the aerodynamic solver. The results of the aerodynamic solver agreed well with that of the CFD simulations when the baseline pod was analyzed. The main trend was captured regarding the flow behaviour, expressed in distributions of various parameters. The differences between the two results were approximately 11.8% on average for different flow quantities. The largest differences were mainly observed at the nose of the pod. In general, quantities were overpredicted by the solver, which was also the case for the pressure. The predicted aerodynamic drag was therefore also higher for the solver, with a predicted total drag of $4.01kN$ as opposed to the $3.95kN$ found through CFD simulations for the baseline pod.

What are the key parameters for the aerodynamic design of the pod and how are they related to the generation of aerodynamic drag?

The first question can partially be answered from literature findings, which has shown that there already has been research conducted on the aerodynamics of systems relatable to the Hyperloop, but still on a preliminary level and without experiments. The main findings herein is that the most important parameters regarding aerodynamic considerations of the pod are the blockage ratio, vehicle speed and operating pressure. The blockage ratio plays an important role in a fluid dynamic condition associated to the Kantrowitz limit. Furthermore, the blockage ratio also affects the shape of the pod that yields a lowest pressure drag. While these three parameters are fixed as a (functional) requirement, it is nonetheless fundamental to understand how a variation in these parameters affect the total drag.

These insights can for instance be used when an optimization is done regarding a velocity profile of the pod. The effects of these external parameters are discussed in more detail in Appendix A.2.

From literature investigations on basic nose and tail shapes (e.g. circular, triangular, etc.) for Maglev trains in a partially evacuated tube, it was concluded that an elliptical nose paired with a similar but more blunt tail yielded the lowest amount of pressure drag for a blockage ratio comparable to the one that is dealt with in this research project. Furthermore, an advised range for the length of the nose was given which should lie between 1.5-2 times the diameter of the vehicle. A longer tail would lead to a negligible drag reduction. In light of these findings, a baseline geometry was designed which also fulfilled the functional requirements as set by HARDT, in order to make quantifiable comparisons. This resulted in a pod with a total length of $49m$ and a diameter of $3.4m$, with nose and tail lengths of $6m$ and $4m$ respectively. This design was presented in Figure 3.2.

What are the key physical phenomena that contribute to the drag generation of the pod?
The development of the boundary layer is key in this internal flow problem. The boundary layer is relatively thick due to the low Reynolds numbers, thereby decreasing the effective bypass area. This boundary layer along with the transition into a turbulent one over the mid-section of the pod consequently lead to a relative small throat area, resulting in a low choked mass flow rate.

The implications of exceeding the Kantrowitz limit, associated to choked flow, are evident through the large pressure peak observed at the front of the pod, which is higher than the stagnation pressure as would be the case in the 'standard scenario' if the flow were not to be choked. Expectedly, the flow accelerates through the bypass areas up to sonic conditions at the throat, which is located at the inflection point where the pod transitions from the constant section towards the tail section.

What are the main assumptions for a simplified aerodynamic solver applicable to this fluid dynamic problem, and what are their implications on the governing fluid dynamic equations and the real physical problem?
The driving assumption for the development of the solver was modelling the flow as an isentropic, quasi-1D flow through a nozzle. The implications of several assumptions made for the development of the solver were clearly visible in the distributions of different quantities. When comparing the results of the solver with that of CFD, the distributions well agree with each other for the general domain, where similar trends and maximum values are reached for instance. However, when comparing the results with the distributions over the pod surface, a larger difference is observed. Clearly, the 2D effects are visible here showing that the quantities do not remain constant over the lateral direction for a certain longitudinal section, but are certainly disturbed by the presence of the pod.

The flow velocity is lower close to the pod due to the viscous effects and the interaction with the boundary layer. Nonetheless, the important trends and prediction of total drag are considered to be adequate in having a low computational cost model that can predict the flow behaviour and the total drag. The added complexity of predicting and modeling a separated flow which is a highly random process, is deemed to not weigh out against the little improve in accuracy for the drag prediction and flow field model. The solver is thus regarded as a suitable low-fidelity model that can be utilized to assess the influence of different parameters on the drag of the pod and to be used as an optimization tool.

The development of the boundary layer plays a crucial role in the accuracy of the solver. As discussed, the boundary layer adds an effective height to the pod through the so-called displacement thickness, thereby influencing the acceleration of the flow. The behaviour of the boundary layer modeled through the Blasius solution shows the limitation of assuming a gradual, steady growth in boundary layer thickness, as well as assuming the transition behaviour to be based off a flow over a flat plate. Therefore, the difference in pressure increases with increasing upstream position. The presence of shock waves and flow separation are not taken into account, though the effects of the shockwaves on the total drag are relatively small in this case due to the low internal tube pressure.

What are the consequences of the optimized pod shape compared to the baseline?
The solver was subsequently coupled to an optimization scheme with an SQP algorithm, which is a gradient based optimization method. The 24 design variables were altered in order to find the geometry with a lower drag compared to the baseline model. The optimization led to a drag reduction of 11.2%, which took 1724 function evaluations spread over 37 iterations.

The optimized geometry was reduced in total length by $1.4m$, whereby its nose has shortened in contrast to the elongation of the tail section. This is also seen through the final values of the design variables. Streamlining the nose would have little effect on the pressure drag (due to exceeding the Kantrowitz limit), which ultimately led to the shortening of the nose, thereby minimizing friction drag.

Besides the reduction in friction drag, the reduction in nose length more importantly contributes to a less critical choking effect as the throat area has increased, consequently leading to a lower pressure peak for the optimized geometry.

While the shape of the nose has little influence on the pressure drag, the tail section does to a large extent influence the amount of this drag component. Evidently, the expansion process starts from the tail section onwards, where the expansion fans were also visible. The more streamlined and thus more gradual decrease in radius compared to the baseline geometry allows for a more gradual flow expansion, where the pressure gradient is lower at the tail section for the optimized geometry. The choking effect is further alleviated by the concavity present at the tail section. Furthermore, the Mach contour plots also showed a smaller area of separation compared to the baseline design.

When looking at the numerical results, the drag reduction was less, where a reduction of 7.19% was achieved. Similar flow characteristics are observed compared to the baseline geometry, where expansion fans are visible followed by oblique shock waves that are reflected by the tube walls. In addition, the region of separated flow has been reduced.

The overpredicted drag reduction was to be expected as the aerodynamic solver is more 'optimistic' in its prediction due to different flow phenomena that are not taken into account, such as the flow separation at the tail section for instance. The mentioned limitations of the solver also play a role in the discrepancy of the predicted drag reduction, as are the observed differences between the numerical method and the aerodynamic solver. In particular, the boundary layer development can be easily manipulated by adjusting the length of the vehicle which resulted in an adjustment of throat area of relative ease. In reality, the manipulation of the boundary layer is a more complex process involving more factors, such as the viscosity that is not constant for compressible flows.

What is the optimal shape of a Hyperloop vehicle?

To arrive back at the main question of this research project, a combination of the answers to the above presented questions gives rise to an answer and can thus be brief.

In very generic terms, if the blockage ratio is fixed as well as the shape and constant section length of the pod, an optimal shape is one in which the nose is blunt and the tail is streamlined and where the choking effect is alleviated as much as possible. In this case specifically, the functional requirements lead to a short, bluntly shaped nose. The tail section was more streamlined, and together with the concavity present, the choking effect was alleviated. The optimal shape was presented in Section 5.7 and shown in Figure 5.2.

6.2. Recommendations for Future Work

Based on the results and drawn conclusions of this research project, additional research questions and opportunities for the enhancement of the current work can be invoked.

- First of all, the aerodynamic solver can be further extended in order to improve its accuracy regarding the prediction of aerodynamic quantities. Since the development of the boundary layer is rather crucial for the velocity distribution and hence the distribution of flow parameters of interest, more focus on this development can significantly improve the accuracy of the solver. Investigations on a more accurate transition location (or the Re_{crit} applicable to these conditions and geometries in that sense) could already lead to notable solver improvements. While the solver at its current state already provides valuable insights in terms of distributional trends, the improvement in accuracy can be beneficial regarding the optimization process in particular, where more confidence in the optimized results and direction of optimization can then be gained if the overall solver accuracy is increased. It must however be noted that these additions to the solver should not come against a demanding increase in computational effort, as this would nullify the benefits and purpose of having a low-fidelity aerodynamic model capable of analyzing a large number of pod geometries in a relatively small amount of time. Whether this is the case or not should be assessed in future work.

- The solver evidently omits structural, economic, infrastructural and performance considerations. Undoubtedly, these are aspects that are of equal importance regarding the entire design of the Hyperloop. For future work, these are thus to be considered and incorporated in order to arrive at a final (detailed) pod design, where the feasible design space can be more accurately defined by (physical) bounds and constraints. In view of this remark, the aerodynamic solver can be embodied into a broader multi-disciplinary design optimization framework. A first step herein could be to extend the optimization procedure to an aero-structural pod optimization, where the drag is to be minimized while the pod weight is within certain thresholds.

- Recommendations can also be made regarding the analysis of (baseline) pod geometries. In this research project, only axisymmetric pods were considered. While this might be beneficial regarding manufacturing processes for instance, it does not necessarily have to be so regarding aerodynamic aspects. Investigations on different (non-symmetric) geometries might result in shapes that have a lower total drag. As such, it allows for trade-offs to be made at later design stages between lower manufacturing costs and possibly lower vehicle drag for instance. Furthermore, the constant section that is present in the current pod design could possibly be altered to a non-flat section or a typical droplet shape that is monotonically decreasing in radius, thereby matching the increase in boundary layer growth to a certain extent. This can then result in an effective pod height that to a certain degree remains constant, which could possibly be beneficial in terms of the aerodynamic drag. Besides the constant effective pod height, a non-axisymmetric shape could also lead to a shape that generates a certain amount of lift. While an induced drag term will most likely be introduced, the generated lift could be utilized in order to alleviate the required power for the pod levitation system, which could improve the efficiency considering the entire system.

- Recommendations can finally be made regarding the optimization procedure. Different optimization algorithms can be opted for which might alleviate the computational effort. It is known for some cases that gradient based algorithms are relatively slow when the current point is close to the optimal point. This was also the case for the current optimization, where 10 of the 37 iterations were required to move to the optimum from a relatively close point (as can be seen in the convergence details given in Appendix B.1). While on one hand, the rate of convergence can be manipulated with the adjustment of certain tolerances, it is on the other hand more desirable to achieve faster convergence in a 'natural' manner. For further interest, investigations on alternative optimization algorithms can be done in which this issue can be avoided. Additionally, the optimization problem can be further extended to a population based algorithm such as a genetic algorithm, where multiple candidate solutions are maintained and improved in order to arrive at a global minimum [85].

Bibliography

[1] Schafer, A. and Victor, D.G., *The future mobility of the world population,* Transportation Research Part A: Policy and Practice **34**, 171 (2000).

[2] E. Musk, *Hyperloop Alpha,* URL: "http://www.spacex.com/sites/spacex/files/hyperloop_alpha-20130812.pdf", [cited 3 May 2017],.

[3] K. Davies, C. Jones, P. Norman, and S. Galloway, *A Review of Turboelectric Distributed Propulsion Technologies for N+3 Aircraft Electrical Systems ,* American Institute of Aeronautics and Astronautics (2013).

[4] J. Braun, J. Susa, and C. Pekardan, *Aerodynamic Design and Analysis of the Hyperloop,* American Institute of Aeronautics and Astronautics , 1 (2016).

[5] J. Chin, J. Gray, S. Jones, and J. Berton, *Open-source conceptual sizing models for the hyperloop passenger pod,* American Institute of Aeronautics and Astronautics , 1 (2015).

[6] H. G. Mobility, *Technical Feasibility Report,* Technical Report (Hardt Global Mobility BV, 2017).

[7] M. Opgenoord and P. Caplan, *On the Aerodynamic Design of the Hyperloop Concept,* American Institute of Aeronautics and Astronautics , 1 (2016).

[8] Schlichting, H. and Gersten, K., *Boundary Layer Theory*, 9th ed. (Springer-Verlag, 1221 Avenue of the Americas, New York, NY 10020, 2017).

[9] A. Kantrowitz and C. Donaldson, *Preliminary Investigation of Supersonic Diffusers,* National Advisory Committee on Aeronautics (1945).

[10] J. Anderson, *Fundamentals of Aerodynamics*, 5th ed. (McGraw-Hill, 1221 Avenue of the Americas, New York, NY 10020, 2011).

[11] T. Kim, K. Kim, and H. Kwon, *Aerodynamic characteristics of a tube train,* Journal of Wind Engineering and Industrial Aerodynamics **99**, 1187 (2011).

[12] A. Hodaib and S. Fattah, *Conceptual Design of a Hyperloop Capsule with Linear Induction Propulsion System,* International Journal of Mechanical, Aerospace, Industrial, Mechatronic and Manufacturing Engineering **10**, 835 (2016).

[13] Manisankar, C. and Verma, S.B. and Raju, C., *Shock-Wave Boundary-Layer Interaction Control on a Compression Corner Using Mechanical Vortex Generators,* 28th International Symposium on Shock Waves , 409 (2012).

[14] H. Wang, D. Coleman, and M. Benedic, *Aerodynamic Simulation of High-Speed Capsule in the Hyperloop System,* American Institute of Aeronautics and Astronautics (2017).

[15] M. Yang, J. Du, and Z. Li, *Moving Model Test of High-Speed Train Aerodynamic Drag Based on Stagnation Pressure Measurements,* Plos One **12** (2017).

[16] Y. Zhang, *Numerical simulation and analysis of aerodynamic drag on a subsonic train in evacuated tube transportation,* Journal of Modern Transportation **20**, 44 (2012).

[17] Mi, B. and Zhan, H. and Zhu, J., *Simulation of aerodynamic drag of high-speed train in evacuated tube transportation,* Journal of Vacuum Science and Technology , 877 (2013).

[18] W. Trzaskoma, *Tube vehicle system (TVS); technology review* (McLean, Va., Mitre Corp., 1970).

[19] J. Ma, X. Chen, and L. Zhao, *Aerodynamic simulation of evacuated tube maglev trains with different streamlined designs,* Journal of Modern Transportation , 115 (2012).

[20] J. Ma, D. Zhou, and L. Zhao, *The approach to calculate the aerodynamic drag of maglev train in evacuated tube,* Journal of Modern Transportation , 200 (2013).

[21] K. Decker, J. Chin, and A. Peng, *Conceptual Feasibility Study of the Hyperloop Vehicle for Next-Generation Transport,* American Institute of Aeronautics and Astronautics , 1 (2017).

[22] Zhang, Y. and Zhu, J. and Mi, B., *Reasonable figure of subsonic train front and rear in evacuated tube transportation based on aerodynamic considerations,* Proceedings of the 2nd International Conference on Electronic and Mechanical Engineering and Information Technology , 734 (2012).

[23] R. Fox, A. McDonald, and P. Pritchard, *Introduction to Fluid Mechanics*, 8th ed., 10, Vol. 4 (John Wiley & Sons, Inc., 2011).

[24] S. Pai, *Modern Fluid Mechanics* (Science Press, Beijing, China, 1981).

[25] M. Knudsen, *The Kinetic Theory of Gases: Some Modern Aspects*, 2nd ed. (Methuen & Co. ltd, 1934).

[26] E. Obert, *Aerodynamic Design of Transport Aircraft* (IOS Press, 2009).

[27] Vos, R. and Farokhi, S., *Introduction to Transonic Aerodynamics*, 1st ed. (Springer Netherlands, 2015).

[28] T. Cebeci, *An Engineering Approach to the Calculation of Aerodynamic Flows* (Horizons Publishing, Long Beach, California, 1999).

[29] E. Laitone, *New Compressibility Correction for Two-Dimensional Subsonic Flow,* Journal of Aeronautical Sciences **18**, 350 (1909).

[30] Kuethe, A.M. and Chow, C., *Bases of Aerodynamic Design*, 5th ed. (John Wiley & Sons, 1998).

[31] Flandro, G.A. and McMahon, H. and Roach, R.L., *Basic Aerodynamics - Incompressible Flow*, 1st ed. (Cambridge University Press, 2012).

[32] Anderson Jr., J.D., *Computational Fluid Dynamics - The Basics With Applications*, 1st ed. (McGraw-Hill Series in Mechanical Engineering, 1995).

[33] Ferziger, J.H. and Peric, M., *Computational Methods for Fluid Dynamics,* 3rd ed. (Springer, 2002).

[34] Panton, R.L., *Incompressible Flow*, 4th ed. (Wiley, 2013).

[35] Wilcox, D.C., *Turbulence Modeling for CFD* (DCW Industries, Inc., La Canada, CA, 1993).

[36] H. Versteeg and W. Malalasekera, *An introduction to Computational Fluid Dynamics*, 5th ed. (John Wiley & Sons, 605 Third Avenue, New York, NY 10158, 1995).

[37] Hanjalic, K. and Launder, B., *Modelling Turbulence in Engineering and the Environment: Second-Moment Routes to Closure* (Cambridge Uniersity Press, 2011).

[38] W. Jones and B. Launder, *The prediction of laminarization with a two-equation model of turbulence,* International Journal of Heat and Mass Transfer **15**, 301 (1972).

[39] Wilcox, D. C., *Formulation of the k-omega Turbulence Model Revisited,* American Institute of Aeronautics and Astronautics **11**, 2823 (2008).

[40] F. Menter, *Zonal Two Equations $k-\omega$ Turbulence Models for Aerodynamic Flows,* American Institute of Aeronautics and Astronautics , 93 (1993).

[41] Spalart, P.R. and Allmaras, S.R., *A One-Equation Turbulence Model for Aerodynamic Flows,* American Institute of Aeronautics and Astronautics , 5 (1992).

[42] Dussauge, J.P., *Computation and Comparison of Efficient Turbulence Models for Aeronautics*, 1st ed. (Springer, 1998).

[43] Cheng, A. and Cheng, T., *Heritage and early history of the boundary element method,* Engineering Analysis with Boundary Elements , 268 (2005).

[44] T. Tranen, *A Rapid Computer Aided Transonic Airfoil Design Method,* American Institute of Aeronautics and Astronautics , 74 (1974).

[45] P. R. Garabedian and G. Mcfadden, *Design of Supercritical Swept Wings,* American Institute of Aeronautics and Astronautics **3**, 289 (1982).

[46] M. Lighthill, *A new method of two dimensional aerodynamic design* (Rep. Memor. Aero. Res. Coun. Lond., 1945) pp. 143–236.

[47] Campbell, R.L., *An approach to constrained aerodynamic design with application to airfoils*, Scientific and Technical Information Program 3260 (National Aeronautics and Space Administration, Langley Research Center, 1992).

[48] P. R. Garabedian and D. G. Korn, *Analysis of transonic airfoils,* Communications on Pure and Applied Mathematics **24** (1971).

[49] Courant, R. and Friedrichs, K.O., *Supersonic Flow and Shock Waves*, 5th ed. (Springer, 1976) pp. 248–252.

[50] P. Li and H. Sobieczky, *Computation of fictitious gas flow with Euler equations,* Acta Mechanica **4**, 251 (1994).

[51] Yu, N. J. and Rubbert, P. E., *Transonic Wing Redesign Using a Generalized Fictitious Gas Method*, Tech. Rep. AD-A070 013 (The Boeing Company, Seattle, WA 98124, 1979).

[52] H. Sobieczky and A.R.Seebass, *Supercritical Airfoil and Wing Design,* Annual Review of Fluid Mechanics **16**, 337 (1984).

[53] Buresti, G., *Elements of Fluid Dynamics*, Vol. 3 (Imperial College Press, 2013).

[54] Schobeiri, M., *Turbomachinery Flow Physics and Dynamic Performance*, Vol. 1 (Springer, 2012).

[55] Sutherland, W., *The viscosity of gases and molecular force,* Philosophical Magazine , 507 (1893).

[56] Blasius, H., *The Boundary Layer in Fluids with Little Friction,* National Advisory Committee for Aeronautics **5** (1950).

[57] DeWitt, D. and Bergman, T., *Fundamentals of Heat and Mass Transfer*, 7th ed. (Wiley, 2011).

[58] Y. Cengel and J. M. Cimbala, *Fluid Mechanics - Fundamentals and Applications* (McGraw-Hill Education, Nevada, Reno, 2017).

[59] White, F., *Fluid Mechanics*, 7th ed. (McGraw-Hill, 2012).

[60] Kulfan, B.M., *"CST" Universal Parametric Geometry Representation Method With Applications to Supersonic Aircraft,* Fourth International Conference on Flow Dynamics (2007).

[61] M. Hazewinkel, *Encyclopedia of mathematisc,* URL:"https://www.encyclopediaofmath.org/index.php/Bernstein_polynomials", [cited 16 December 2017] (1994).

[62] F. Moukalled, L. Mangani, and M. Darwish, *The Finite Volume Method in Computational Fluid Dynamics*, 1st ed., Vol. 113 (Springer, 2015).

[63] Choring, A. J., *Numerical Solution of the Navier-Stokes Equations,* Mathematics of Computation **22**, 745 (1968).

[64] S. V. Suhas, *Numerical Heat Transfer and Fluid Flow* (Taylor and Francis, 1980).

[65] Barth, T. and Jespersen, D. C., *The Design and Application of Upwind Schemes on Unstructured Meshes*, 27th Aerospace Sciences Meeting AIAA-89-0366 (NASA, Ames Research Center, Reno, Nevada, 1989).

[66] Diskin, B. and Thomas, J. L. and Nielsen, E. J. and Nishikawa, H., *Comparison of node-centered and cell-centered unstructured finite-volume discretizations. Part I: viscous fluxes,* American Institute of Aeronautics and Astronautics **48**, 1326 (2010).

[67] Anderson, W. and Bonhus, D. L., *An Implicit Upwind Algorithm for Computing Turbulent Flows on Unstructured Grids,* Computers & Fluids **23**, 1 (1994).

[68] C. Ward and D. Kincaid, *Linear Algebra: Theory and Applications* (Jones and Bartlett, Sudbury, Massachusetts, 1910).

[69] Correa, C. D. and Hero, R. and Ma, K. L., *A Comparison of Gradient Estimation Methods for Volume Rendering on Unstructured Meshes,* IEEE Transactions on Visualization and Computer Graphics **17**, 305 (2011).

[70] F. Inc., *8.14.3. - Setting the Operating Pressure,* URL:"https://www.sharcnet.ca/Software/Fluent6/html/ug/node374.htm", [cited 22 February 2018] (2006).

[71] F. Incorporation, *23.3.5 Energy Equation,* URL:"https://www.sharcnet.ca/Software/Fluent6/html/ug/node885.htm", [cited 23 February 2018] (2006).

[72] T.H. Shih, W. W. Liou, A. Shabbir, Z. Yang, and J. Zhu, *A New k-ϵ Eddy-Viscosity Model for High Reynolds Number Turbulent Flows - Model Development and Validation,* Computers & Fluids **24**, 227 (1995).

[73] Launder, B. E. and Spalding, D. B., *Mathematical Models of Turbulence*, 2nd ed. (Academic Press inc, 1972).

[74] W. C. Reynolds, *Fundamentals of Turbulence for Turbulence Modeling and Simulation*, Technical Report (Department of Mechanical Engineering, Stanford University, 1987).

[75] M. D. Salas, J. N. Hefnes, and L. Sakell, *Modeling Complex Turbulent Flows*, 1st ed., Vol. 7 (Springer, 1999).

[76] Bulat, M. P. and Bulat, P. V., *Comparison of Turbulence Models in the Calculation of Supersonic Separated Flows,* World Applied Sciences Journal **10**, 1263 (2013).

[77] S. B. Pope, *Turbulent Flows*, 1st ed. (Cambridge University Press, 2000).

[78] Salim, S. M. and Cheach, S. C., *Wall y^+ Strategy for Dealing with Wall-bounded Turbulent Flows,* Proceedings of the International MultiConference of Engineers and Computer Scientists **2** (2009).

[79] Gharbi, N. and Absi, R. and Benzaoui, A. and Amara, E. H., *Effect of near-wall treatments on airflow simulations,* Proceedings of 2009 International Conference on Computational Methods for Energy Engineering and Environment: ICCM3E , 185 (2009).

[80] F. Incorporation, *6.3.5. Mass Flow Inlet Boundary Conditions,* URL:"https://www.sharcnet.ca/Software/Ansys/16.2.3/en-us/help/flu_ug/flu_ug_sec_bc_mfinlet.html", [cited 23 February 2018] (2006).

[81] I. The MathWorks, *Fmincon Documentation,* URL:"https://nl.mathworks.com/help/optim/ug/fmincon.html", [cited 2 March 2018] (2018).

[82] Schittkowski, K., *NLQPL: A FORTRAN-Subroutine Solving Constrained Nonlinear Programming Problems,* Annals of Operations Research **5**, 485 (1985).

[83] R. Fletcher, *Practical Methods of Optimization* (John Wiley and Sons, 1987).

[84] P. E. Gill, M. A. Murray, and M. H. Wright, *Practical Optimization* (Academic Press, London, 1981).

[85] Blum, C. and Roli, A, *Metaheuristics in combinatorial optimization: Overview and conceptual comparison,* ACM Computing Surveys **2**, 268 (2003).

A

Pod aerodynamic characteristics

A.1. Comparison of flow parameters

In addition to the comparisons of the pressure and Mach number distributions presented in Section 4.4, the distributions of the temperature and density are given in figures A.1 and A.2 respectively.
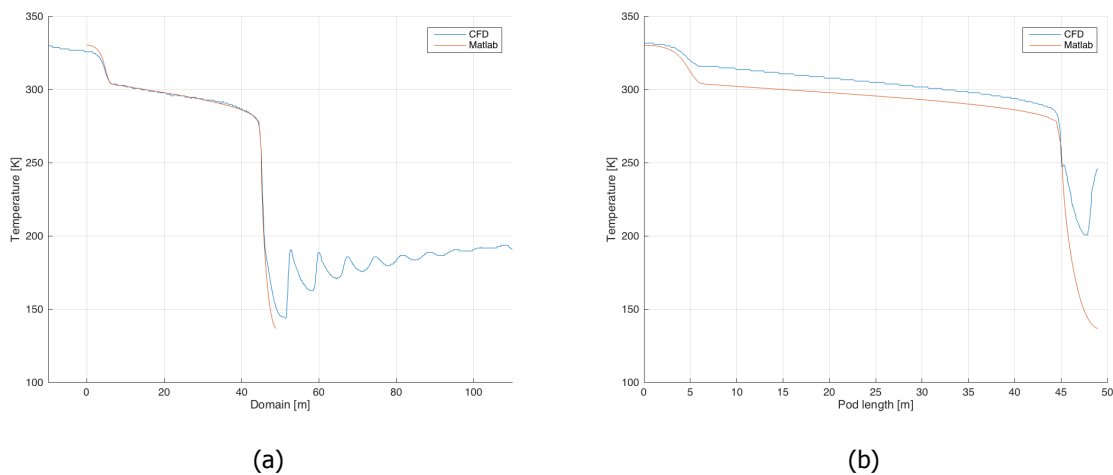

(a)

(b)

Figure A.1: Temperature distributions of the domain (a) and the pod surface (b)

(a)   (b)
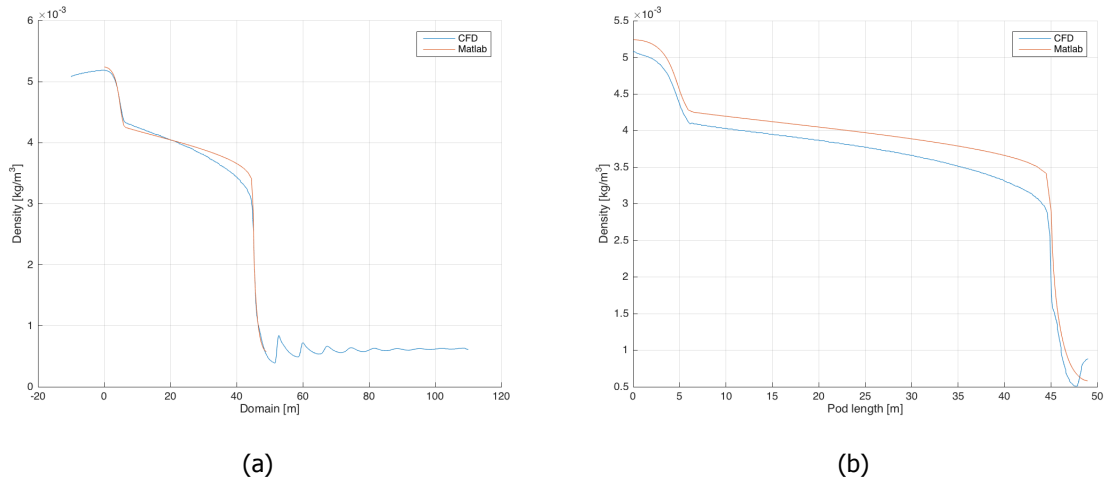
Figure A.2: Density distributions of the domain (a) and the pod surface (b)

Similar conclusions can be drawn regarding the differences between the results of the solver and CFD, where the solver result generally well agrees with the numerical results, but to a lesser extent when compared to the distributions directly over the pod surface.

In addition, the distributions for the pressure coefficients as well as the total temperature variation within the domain obtained by CFD are shown in Figure A.3.

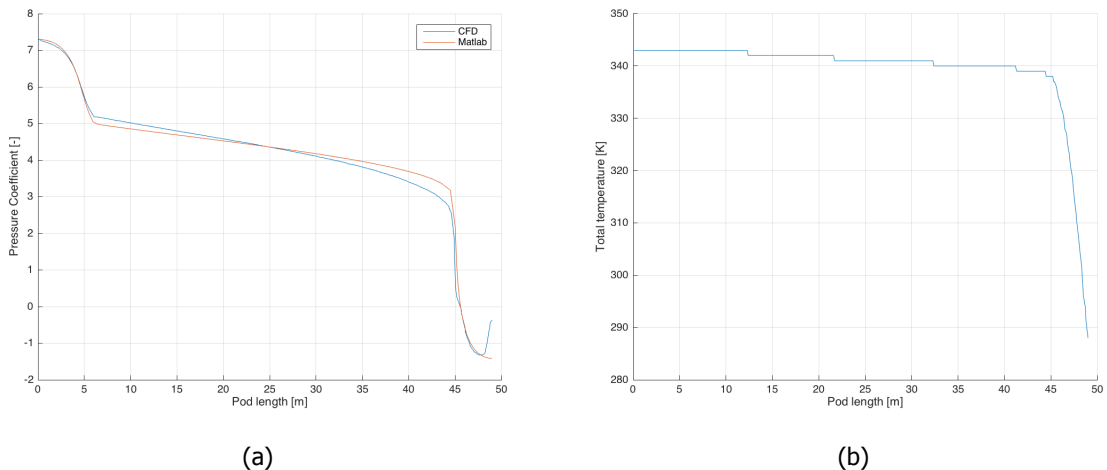(a)   (b)

Figure A.3: Pressure coefficient (a) and total temperature (b) distributions

As mentioned, an isentropic flow was assumed in the solver implying that the total temperature remains constant over the entire flow domain. To assess the validity of this assumption, the distribution of the total temperature obtained from CFD is shown in Figure A.3b. It can be seen that the total temperature is certainly not constant. The value drops gradually but with an insignificant amount for the largest part, with a decrease of 1.46% from the nose up to approximately $45.2m$. Over the final $3.8m$, the value drops drastically due to the irreversibilities associated to flow separation to the final value of $288k$, equal to the static value. The isentropic flow assumption therefore generally holds for the majority of the flow, except for the last part of the tail section, adding to the inaccuracy of the solver.

A.2. Effect of external parameters on total drag

From literature, it was concluded that the most important external parameters that affect the total aerodynamic drag are the blockage ratio, internal tube pressure and operating velocity. Though these

three parameters are fixed as a requirement in this thesis project, it is nonetheless fundamental in gaining more understanding of how the drag varies with a different set of these parameters. This might provide valuable insights when considering the operational aspects of the Hyperloop system and possible future optimization procedures regarding those aspects. The change in drag with operational speed might for instance be useful when a certain velocity profile is to be defined.

First of all, the blockage ratio is varied from 0.1 to 0.85. In this case, the radius of the pod is kept constant, where the tube radius is varied. The change in drag can be seen in Figure A.4, where the current blockage ratio (0.625) is depicted as well. As expected, the drag rises rapidly with increasing blockage ratio since the bypass area is decreased, leading to a stronger choking effect. It can furthermore be noted that a quadratic relation exists between the drag and blockage ratio.
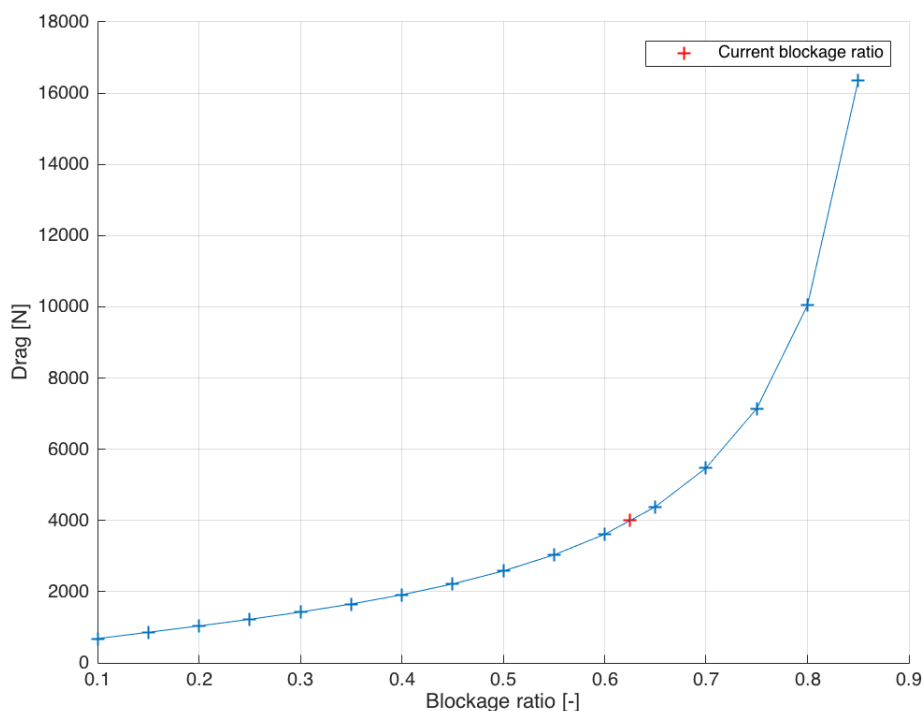
Figure A.4: Variation of drag with blockage ratio

The changes in drag due to a change in internal tube pressure and velocity are shown in Figure A.5. The drag varies linearly with increasing internal tube pressure. A rapid increase in drag can be seen when the velocity exceeds $\approx 99.5 m/s$. After this velocity, the flow becomes choked which causes the drag to drastically rise. This 'critical speed' can be found based on the choked mass flow rate and is thus dependent on the throat area. It is therefore also dependent on the blockage ratio. Before this critical speed is reached, a quadratic relation can be observed between the drag and pod velocity. After this, the relation changes to a more or less linear relation.
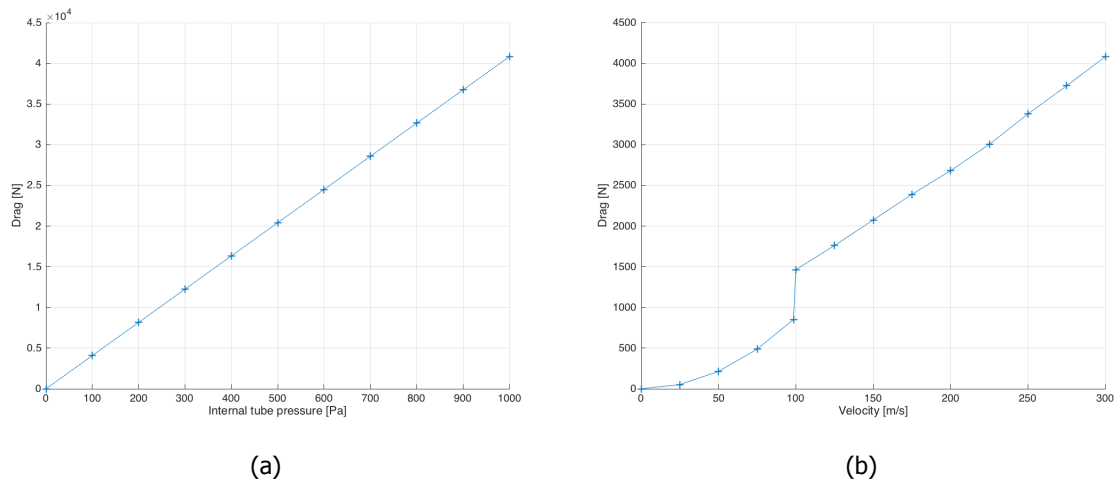
<div align="center">(a)   (b)</div>

<div align="center">Figure A.5: Variation of drag with internal pressure (a) and velocity (b)</div>

A.3. Additional CFD verification procedures

It is often emphasized that the CFD simulations are a crucial part in the validation of the aerodynamic solver. Therefore, additional verification procedures to the ones that were presented in Section 4.5 are carried out. As discussed, far-field boundary conditions are necessary for imposing external flow conditions on the computational domain. The real physical flow domain is evidently too large to incorporate in a computational domain. A pressure far-field condition was therefore used in order to allow for the reduction in size of the computational domain, and consequently the computational time. This boundary condition models a free-stream condition at infinity, where the Mach number and static conditions are imposed. However, to correctly approximate the 'true infinity conditions', the far-field boundary must be placed far enough from the object of interest. If placed too closely, the boundary condition can produce artificial effects.

In the specific case of the pod analyses, an artificial effect can for instance be the erroneous amount of reflected oblique shocks in order to satisfy the far-field condition. A simulation is therefore performed with an increased computational domain size, where the inlet and outlet are placed $50m$ in front of the pod and approximately $200m$ behind the pod respectively (compared to the original $10m$ and $51m$), thereby having a total domain length of $300m$. The Mach contours around the tail area for this simulation is shown in Figure A.6, while the pod in the entire computational domain is shown in Figure A.7.

<div align="center">Figure A.6: Tail area Mach contours in an increased computational domain size</div>

The contours show a similar flow behaviour compared to the earlier presented CFD results, where the oblique shocks are reflected and barely visible after three reflections, with again the shocks at the same location. The increased inlet distance also yield a similar high pressure region, where finally a total drag of $3.97kN$ is computed. With the same flow behaviour and approximately 0.25% difference in predicted drag, it can be concluded that the initial computational domain is sufficiently large to incorporate the far-field conditions, which saves a large amount of computational time compared to the current domain. This can also be noted from the converge histories of the residuals and total drag, shown in Figures A.8a and A.8b respectively, where approximately 2100 iterations are required to reach convergence (compared to the original 550).
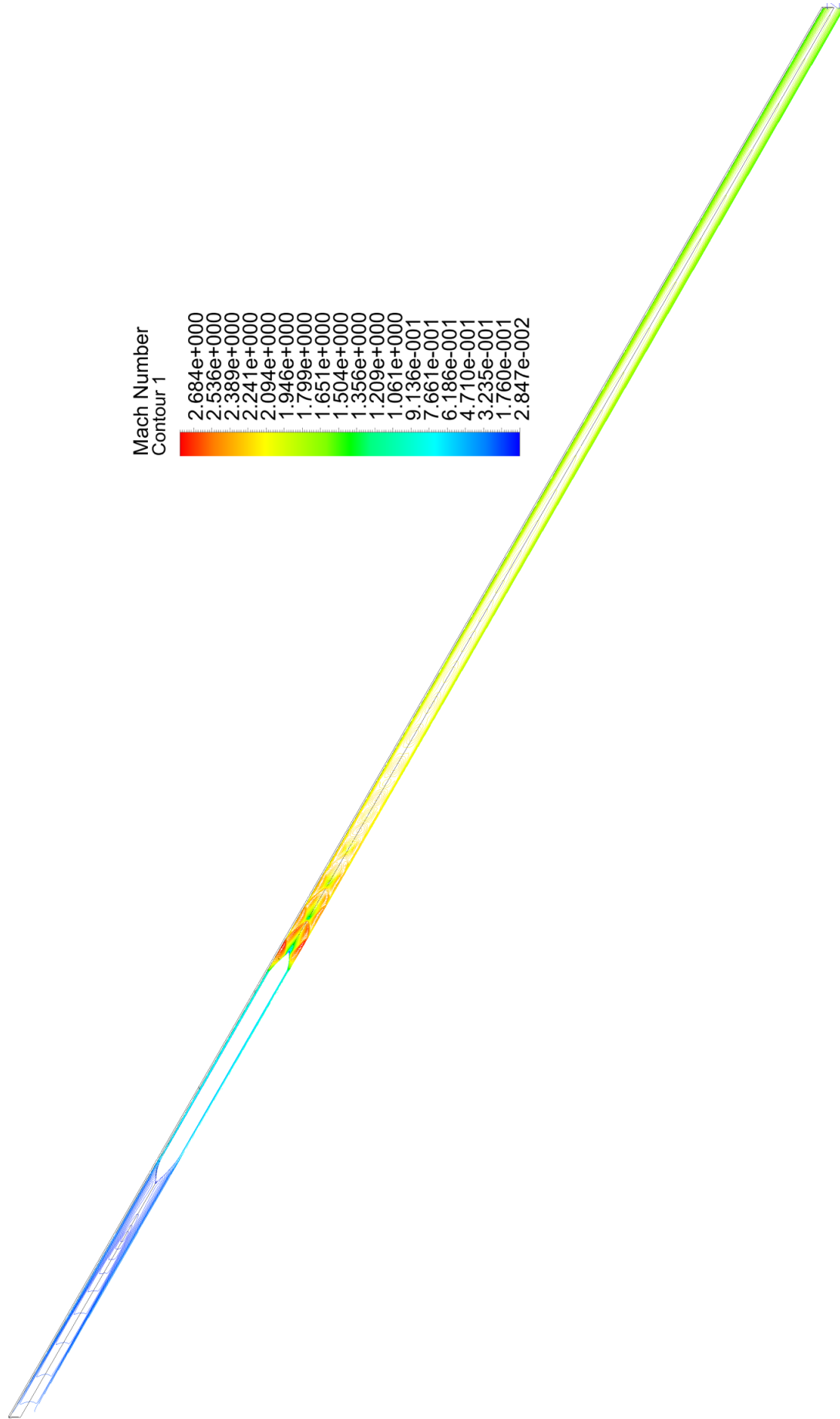
Figure A.7: Mach contours in the entire computational domain

(a)   (b)
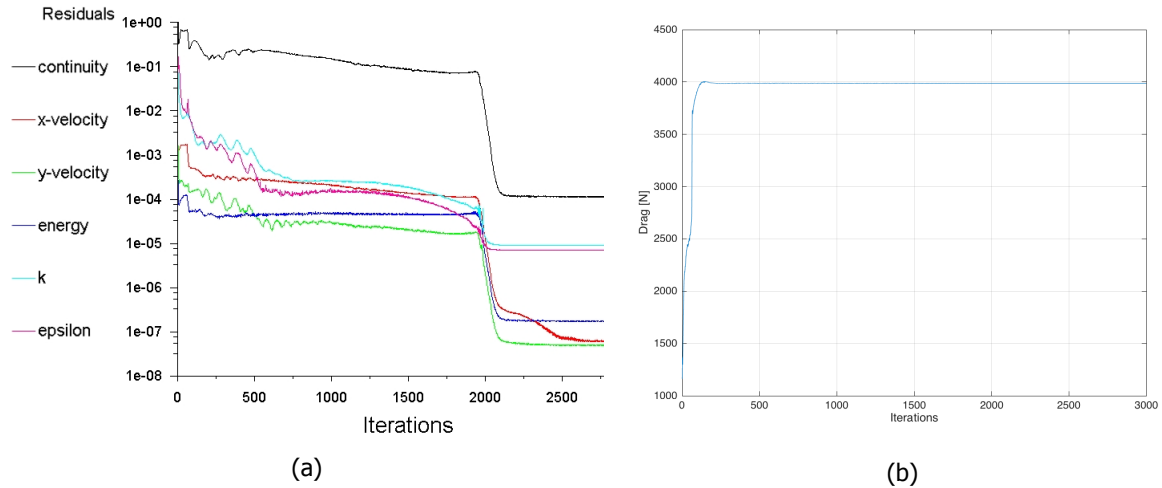
Figure A.8: Convergence history of the residuals (a) and total drag (b)

Since the tube walls are relatively close to the pod, the effect of these walls are investigated further by means of adding prism layers to the tube walls. A close up of this mesh around the pod area is shown in Figure A.9 with the corresponding Mach contour plot shown in Figure A.10.
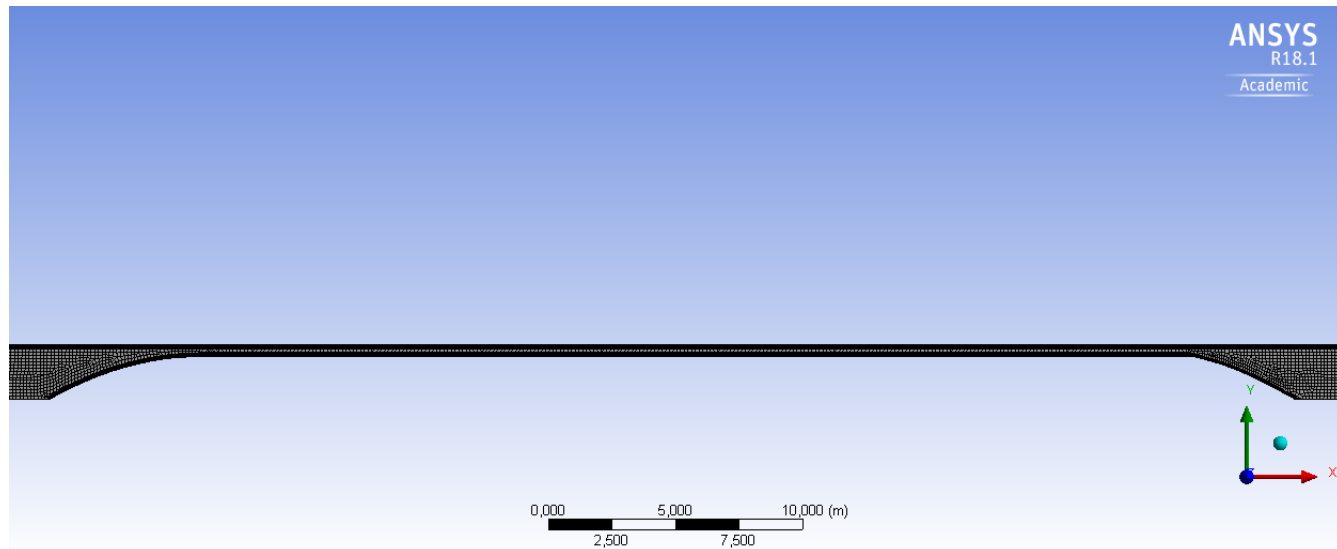

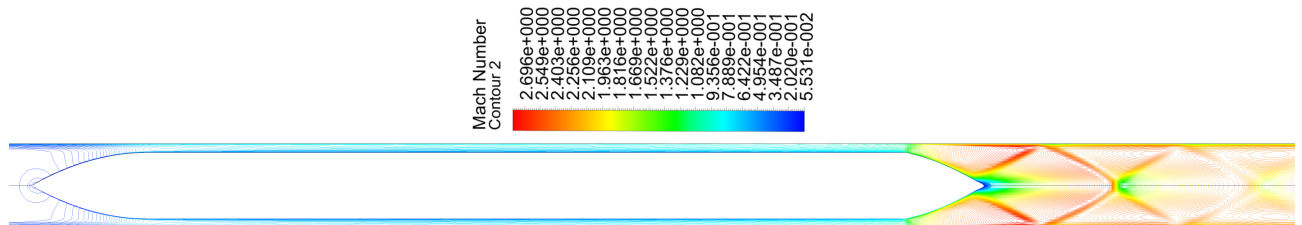Figure A.9: Mesh around the pod with prism layers added to the tube wall

Figure A.10: Mach contours of the mesh with prism layers at the tube wall

Once again, similar flow behaviours are observed with no notable differences in the bypass area specifically, and the total drag is in comparable orders ($3.96 kN$). The results of the additional verification procedures therefore give more confidence in the independence of the numerical results to

the computational grid and boundary conditions. This is also the case for the results of the optimized geometry, since those are obtained with only the first (coarse) mesh and small computational domain.

As a final verification procedure, the simulation is performed with a different turbulence model. Since the flow is assumed to be transitional, a simulation is performed with the transition SST model. This model was not used in the initial analyses due to its relative high computational requirements (solving 4 transport equations) and inaccuracy for wall bounded flows compared to the $k - \epsilon$ model. For brevity, only the Mach number and pressure distributions along the wall for the pod length are shown, and can be seen in Figures A.11a and A.11b respectively

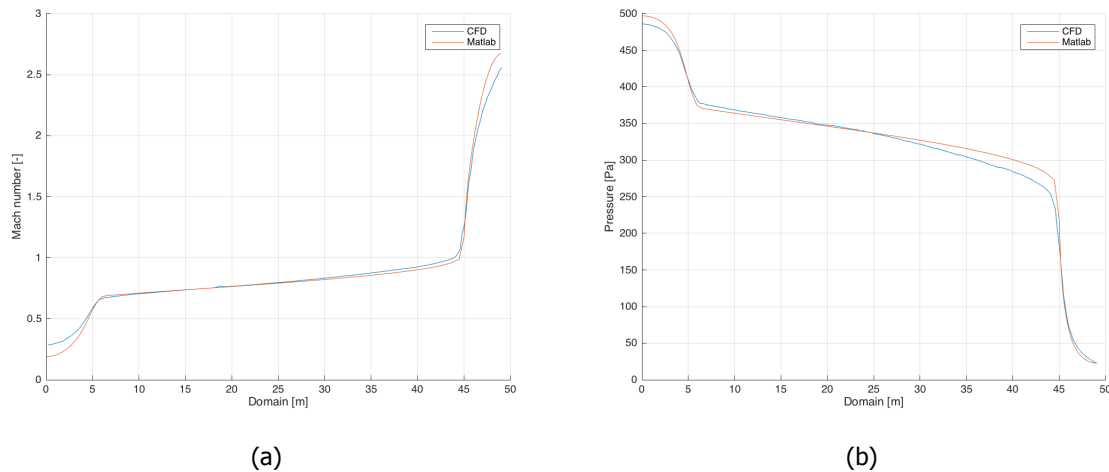(a)   (b)

Figure A.11: Distributions along the tube wall of the Mach number (a) and pressure (b)

Similarities are found for the differences between the solver and CFD results. Again, the pressure peak is overpredicted, however by a smaller amount (2.23% overprediction). When the flat section of the pod is reached, the pressure is underpredicted by the solver due to a higher pressure gradient, leading to an intersection between the distributions. Again, the inaccuracy increases with downstream location to a maximum difference of 11.3% at the start of the tail section (at $x = 45m$).

This trend is analogous to the Mach number distribution, however with smaller values of differences between the solver and CFD results. The maximum Mach number corresponds well with that encountered in the entire flow domain, but to a lesser extent to the maximum Mach number along the tube wall.

B

Optimization details

B.1. Convergence history of optimization parameters

In addition to the final values of the design variables as was given in Table 5.3, the MATLAB command window with additional iteration information is shown below. In accordance with the discussion in Section 5.9, the optimization took 37 iterations constituting 1724 function evaluations (F-count), where the normalized objective function f(x) has been reduced to its final value of 8.885421e-01. The feasibility of the solution given in the fourth column can be regarded as the adherence to the constraints, which ideally should be as close as possible to 0.

Iter	F-count	f(x)	Feasibility	Steplength	step	optimality
0	45	1.000000e+00	1.000e-04			4.915e+00
1	90	9.903462e-01	7.228e-04	1.000e+00	8.522e-02	1.998e-01
2	138	9.853521e-01	1.046e-03	4.900e-01	2.075e-01	1.418e+00
3	192	9.849528e-01	1.031e-03	4.035e-02	1.507e-02	1.539e+00
4	239	9.733364e-01	4.523e-03	7.000e-01	4.543e-01	2.167e+00
5	284	9.157984e-01	2.629e-03	1.000e+00	3.000e-01	9.342e-01
6	329	9.063392e-01	1.314e-03	1.000e+00	1.550e-01	5.903e-01
7	374	9.061892e-01	1.866e-07	1.000e+00	5.148e-02	5.047e-01
8	419	9.042419e-01	1.574e-04	1.000e+00	3.873e-02	3.583e-01
9	464	9.027015e-01	9.515e-05	1.000e+00	5.434e-02	4.360e-01
10	509	8.954363e-01	7.320e-04	1.000e+00	1.930e-01	4.973e-01
11	554	8.944062e-01	1.339e-04	1.000e+00	1.137e-01	3.842e-01
12	599	8.920750e-01	1.607e-04	1.000e+00	1.037e-01	3.838e-01
13	644	8.916557e-01	5.844e-05	1.000e+00	4.122e-02	5.083e+00
14	689	8.910973e-01	4.349e-05	1.000e+00	2.736e-02	2.749e-01
15	734	8.911540e-01	1.306e-16	1.000e+00	9.472e-03	6.867e-02
16	779	8.908968e-01	1.306e-16	1.000e+00	4.601e-02	3.508e-02
17	824	8.906338e-01	1.306e-16	1.000e+00	5.106e-02	3.441e-02
18	869	8.903899e-01	1.306e-16	1.000e+00	4.827e-02	6.442e-02
19	914	8.901044e-01	1.306e-16	1.000e+00	5.720e-02	3.361e-02
20	959	8.900586e-01	1.306e-16	1.000e+00	1.141e-02	1.387e-02
21	1004	8.899001e-01	1.306e-16	1.000e+00	3.943e-02	1.402e-02
22	1049	8.898803e-01	1.306e-16	1.000e+00	6.232e-03	1.400e-02
23	1094	8.897812e-01	1.306e-16	1.000e+00	3.141e-02	1.392e-02
24	1139	8.893078e-01	1.306e-16	1.000e+00	1.554e-01	1.357e-02
25	1184	8.888528e-01	1.306e-16	1.000e+00	1.585e-01	1.330e-02
26	1229	8.888166e-01	1.306e-16	1.000e+00	1.443e-02	1.328e-02
27	1274	8.886832e-01	1.306e-16	1.000e+00	5.393e-02	1.321e-02
28	1319	8.886291e-01	1.306e-16	1.000e+00	2.222e-02	1.319e-02
29	1364	8.886287e-01	1.306e-16	1.000e+00	5.616e-04	2.893e-03
30	1409	8.886272e-01	1.306e-16	1.000e+00	2.799e-03	2.722e-03

Iter	F–count	f(x)	Feasibility	Steplength	Norm of step	First–order optimality
31	1454	8.886199e−01	1.306e−16	1.000e+00	1.384e−02	1.894e−03
32	1499	8.885903e−01	1.306e−16	1.000e+00	6.567e−02	1.274e−03
33	1544	8.885640e−01	1.306e−16	1.000e+00	8.867e−02	1.789e−03
34	1589	8.885626e−01	1.306e−16	1.000e+00	1.611e−03	1.746e−03
35	1634	8.885563e−01	1.306e−16	1.000e+00	7.798e−03	1.537e−03
36	1679	8.885425e−01	1.306e−16	1.000e+00	3.285e−02	1.364e−03
37	1724	8.885421e−01	1.306e−16	1.000e+00	1.186e−02	5.074e−05

A visual representation concerning the convergence histories of the objective function and the constraints is given in Figures B.1 and B.2 respectively. As was discussed in Section 6.2, the reduction in objective function value is relatively small starting from approximately 1200 function evaluations, or equivalently the 27th iteration, which sometimes occurs for gradient based algorithms.

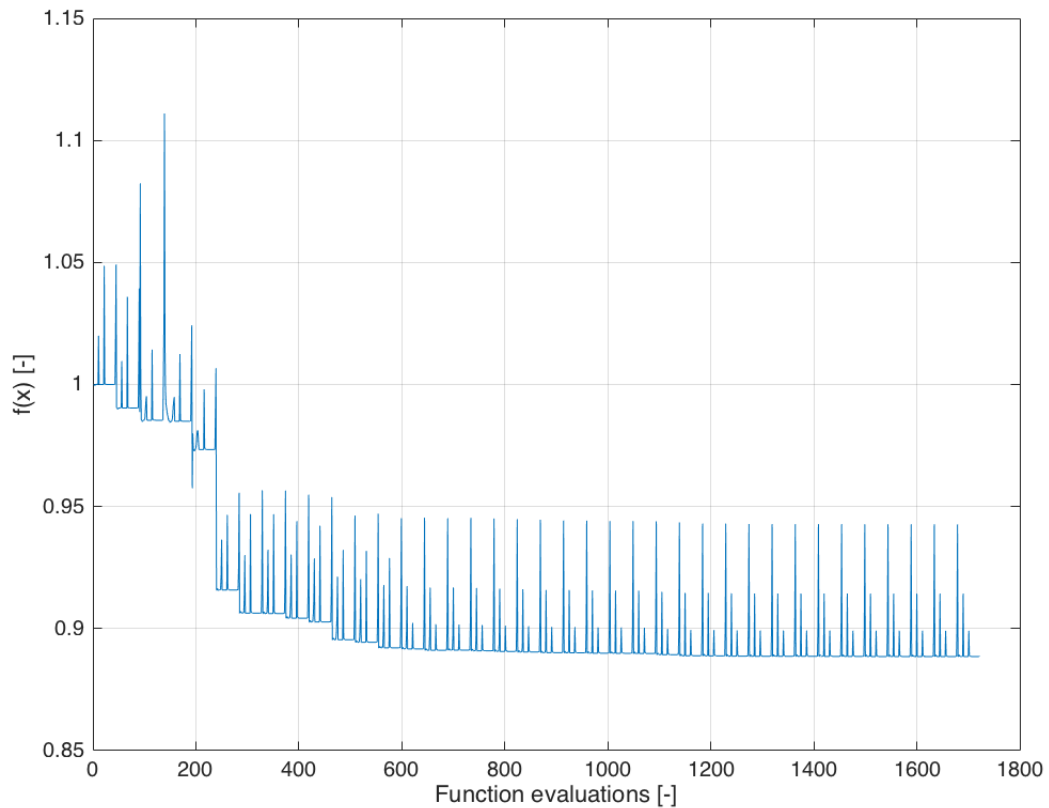Figure B.1: Convergence history of normalized objective function

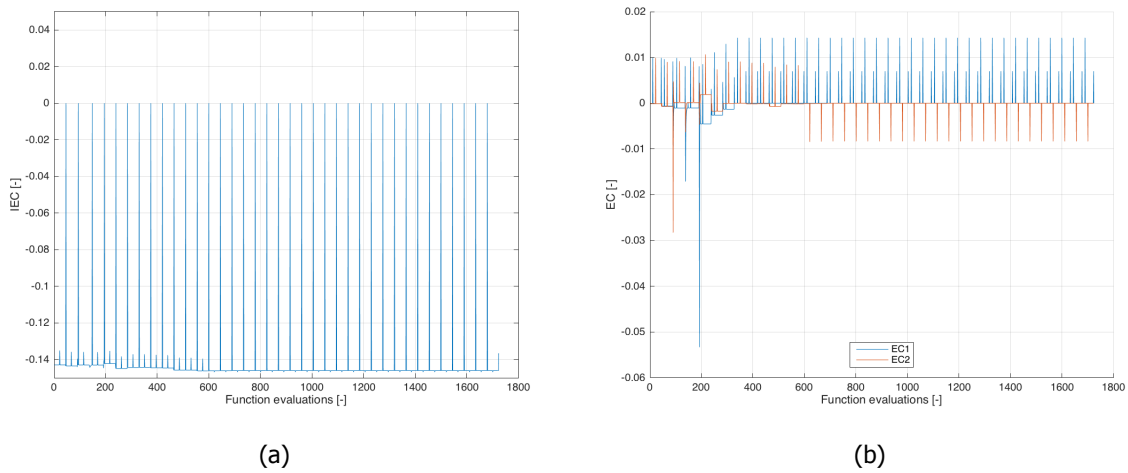(a)   (b)

Figure B.2: Convergence histories of the normalized equality (a) and inequality constraints (b)

B.2. Residual monitor of optimized geometry simulation

The convergence history of the residuals and the drag for the optimized geometry are shown in Figures B.3 and B.4 respectively. Once again, similar trends in the convergence history are observed. The amount of iterations required for convergence are comparable to that of the baseline geometry for the coarse mesh.
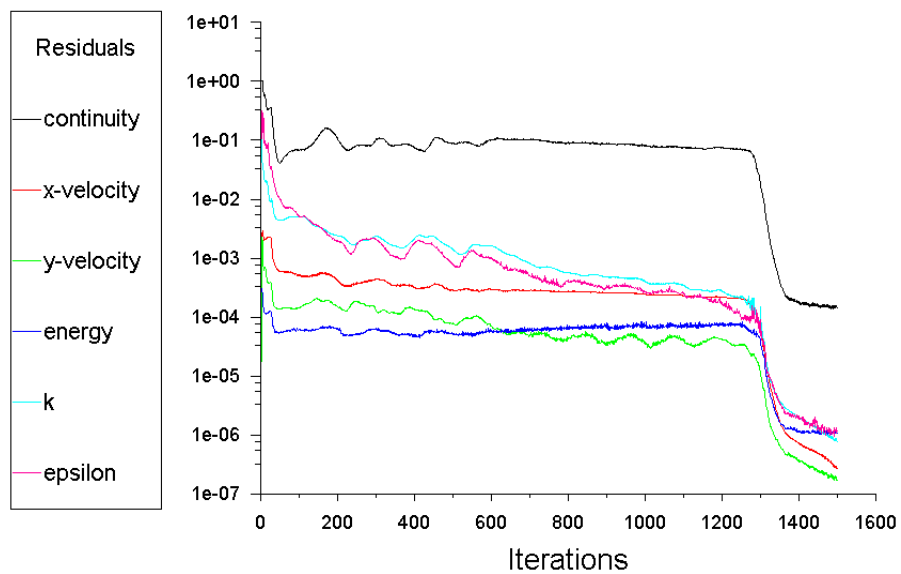

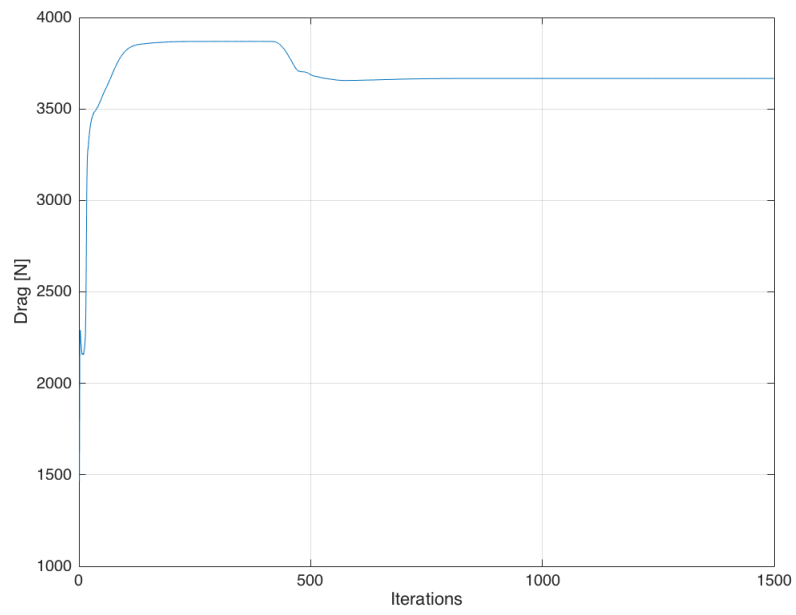Figure B.3: Convergence history of the residuals for the optimized geometry

Figure B.4: Convergence history of the total drag for the optimized geometry